

2018

Seismic Response of Moment Resisting Frames Coupled with Rocking Walls

Mehrdad Aghagholizadeh
University of Central Florida



Part of the [Civil Engineering Commons](#)

Find similar works at: <https://stars.library.ucf.edu/etd>

University of Central Florida Libraries <http://library.ucf.edu>

This Doctoral Dissertation (Open Access) is brought to you for free and open access by STARS. It has been accepted for inclusion in Electronic Theses and Dissertations by an authorized administrator of STARS. For more information, please contact STARS@ucf.edu.

STARS Citation

Aghagholizadeh, Mehrdad, "Seismic Response of Moment Resisting Frames Coupled with Rocking Walls" (2018). *Electronic Theses and Dissertations*. 6156.
<https://stars.library.ucf.edu/etd/6156>



SEISMIC RESPONSE OF MOMENT RESISTING FRAMES COUPLED WITH ROCKING WALLS

by

MEHRDAD AGHAGHOLIZADEH

M.S. Tarbiat Moallem University, Tehran, 2011

B.S. Azad University, Tehran, 2009

A dissertation submitted in partial fulfillment of the requirements
for the degree of Doctor of Philosophy
in the Department of Civil, Environmental and Construction Engineering
in the College of Engineering and Computer Science
at the University of Central Florida
Orlando, Florida

Fall Term
2018

Major Professor: Nicos Makris

© 2018 Mehrdad Aghagholizadeh

ABSTRACT

This study investigates the inelastic response of yielding structures coupled with rocking walls. This topic is of major significance in the design of tall moment-resisting buildings, since during recent major earthquakes several tall, moment-resisting frames that had been designed in accordance to the existing seismic code provisions, exhibited a weak-story failure. Utilization of this structural system can help reducing maximum story drifts, prevents weak story failure and minimize residual deformation of the structure. This study first examines different configurations of both stepping rocking walls and pinned rocking walls that have been reported in the literature. Next, effect of additional vertical tendons or vertical damping devices in maximum response of the system is investigated. This research first derives the nonlinear equations of motion of a yielding oscillator coupled with a rocking wall and the dependability of the one-degree of freedom idealization is validated against the nonlinear time-history response analysis of a 9-story moment-resisting frame coupled with a rocking wall. This research finally concludes that, stepping wall suppresses peak and permanent displacements, with the heavier wall being most effective. In contrast, the pinned rocking wall increases in general the peak inelastic displacements and the permanent displacements. While, the coupling of weak building frames with rocking walls is an efficient strategy that controls inelastic deformations by enforcing a uniform interstory-drift distribution, therefore, avoiding mid-story failures, the study shows that even for medium-rise buildings the effect of vertical tendons on the inelastic structural response is marginal, except for increasing the vertical reactions at the pivoting points of the rocking wall. Additionally, The SDOF idealization presented in this study compares satisfactory with finite-element analysis of a 9-story steel SAC building coupled with a stepping rocking wall; therefore, the SDOF idealization can be used with confidence for preliminary analysis and design.

To my parents Azam and Parviz.

"It wasn't the New World that mattered...Columbus died almost without seeing it; and not really knowing what he had discovered. It's life that matters, nothing but life—the process of discovering, the everlasting and perpetual process, not the discovery itself, at all."

The Idiot, Fyodor Dostoyevsky

ACKNOWLEDGMENTS

First, I want to express my gratitude to my advisor Dr. Nicos Makris for his guidance, support and friendship throughout my PhD research. His guidance helped me in all the time of my research. His mentorship and patience will always be a valuable example for my future career. Without his guidance and support this research would have not been possible.

I want to thank my committee members Dr. Necati Catbas, Dr. Kevin Mackie and Dr. Jeffrey Kauffman. I want to thank Dr. Necati Catbas for his support in my first year of PhD and his friendship and guidance throughout my work. I want to thank Dr. Kevin Mackie for his help in numerical analysis specifically in OpenSees parts of my study. I also want to thank Dr. Jeffrey Kauffman for the things he taught me in his course and being always available for students.

I want to thank my friends and colleagues, Dr. Ricardo Zaurin, Dr. Ozan Celik, Dr. Soroush Mokhtari, Dr. Tung Khuc, Dr. Georgios Kampas, Amirsalar Esfahani and Reza Moghimi for their friendship and support.

I want to thank my hometown friends Nima Samadzadegan, Erfan Khadji and Kaveh Chizari who have always supported me.

Last but not least, I want to thank my family Parviz, Azam, Mahsa and Mehrnoush and my girl-friend Erica for their love and support throughout this journey, your unconditional support and love gave me strength to overcome all difficulties.

TABLE OF CONTENTS

LIST OF FIGURES	x
LIST OF TABLESxxvi
CHAPTER 1: INTRODUCTION	1
Overview	1
Dynamics of a Rocking Column	5
Rocking Wall and Frame in Literature	8
Objectives and Scope	16
CHAPTER 2: YIELDING STRUCTURE WITH A STEPPING AND PINNED ROCKING WALL	18
Introduction	18
Dynamics of a Yielding Oscillator Coupled with a Stepping Rocking Wall	21
Dynamics of a Yielding Oscillator Coupled with a Pinned Rocking Wall	26
Parameters of the Problem	30
Validation of the SDOF-Idealization	35
Earthquake spectra of a yielding oscillator coupled with a rocking wall	38

Special Case: Elastic Oscillator Coupled with a Rocking Wall	41
Response Spectra of an Elastic Oscillator Coupled with a Rocking-Wall	43
Pulse Spectra of an Elastic Oscillator Coupled with a Rocking-Wall	47
Importance of the Length of the Coupling Arm	51
Stepping rocking wall	51
Pinned rocking wall	52
Conclusion	56
 CHAPTER 3: VERTICALLY RESTRAINED ROCKING WALL	 58
Dynamics of a Yielding Oscillator Coupled with a Vertically Restrained Stepping Rock- ing Wall	 58
Minimum Acceleration Needed to Initiate Uplift of The Coupled, Vertically Restrained Rocking Wall	 62
Parameters of The Problem	63
Normal Forces at the Pivoting Corners	64
Validation of the SDOF-Idealization	71
Earthquake Spectra of a Yielding Oscillator Coupled with a Rocking Wall	76
Conclusion	80

CHAPTER 4: YIELDING STRUCTURES COUPLED WITH DAMPED ROCKING WALLS

82

Introduction	82
Dynamics of a Yielding Oscillator Coupled with a Stepping Rocking Wall with Supplemental Damping	84
Kinematics of the Structural System	85
Constitutive Laws of Non-Linear Viscous and Hysteretic Dissipation Devices	87
Equation of Motion of the Entire System	88
Parameters of the Problem	90
Earthquake Spectra of a Yielding Oscillator Coupled with a Stepping Rocking Wall with Supplemental Damping	97
Difference between Viscous and Hysteretic Dampers Behavior	103
The Effect of Supplemental Hysteretic and Viscous Damping on the Rocking Response of Free-Standing Columns	106
Equation of Motion of a Rocking Column with Vertical Energy Dissipators	108
Review of The Transverse Rocking Response of The South Rangitikei Rail Bridge	110
Statement of the problem	110
Time history response analysis of the South Rangitikei Rail Bridge	113
Scholia	116

Response of the South Rangitikei Rail Bridge to more Violent Earthquake	
Records	117
An "Unexpected" Combination of Gravity, Inertia and Hysteretic Forces	119
Rocking Response with Viscous Dampers	121
Response To Mathematical Pulses	124
Rocking Response Diagrams	125
Retrofit of Rocking Columns with Vertical Energy Dissipation Devices with Finite	
Length	130
Conclusion	133
CHAPTER 5: CONCLUSION	134
LIST OF REFERENCES	136

LIST OF FIGURES

Figure 1.1: Weak Story Failure of Olive View Hospital after 1971 San Fernando, CA Earthquake.	1
Figure 1.2: Weak Story Failure of Marshal Hotel after 2018 Hualien, Taiwan Earthquake.	2
Figure 1.3: Schematic of a Rocking Block.	6
Figure 1.4: Moment-rotation diagram of a rocking block.	7
Figure 1.5: Conventional Fixed shear wall (left) compared to stepping rocking wall (center) and Pinned rocking wall (right).	12
Figure 2.1: (a): Yielding single-degree-of-freedom oscillator coupled with a stepping rocking wall. While schematically the wall is shown to be connected in series with the mass, the dynamics of the wall works in parallel with the nonlinear spring and dashpot because of the rigid connection between the mass and the wall. (b): The bilinear idealization with its control parameters. (c): Force-displacement diagram of the stepping rocking wall.	19
Figure 2.2: (a): Yielding single-degree-of-freedom oscillator coupled with a pinned rocking wall. While schematically the wall is shown to be connected in series with the mass, the dynamics of the wall works in parallel with the nonlinear spring and dashpot because of the rigid connection between the mass and the wall. (b): The bilinear idealization with its control parameters. (c): Force-displacement diagram of the pinned rocking wall.	27

Figure 2.3: (a) Time-history analysis of a nonlinear SDOF oscillator coupled with a stepping rocking wall with normalized strength $Q/m_s = 0.15g$, mass ratio $\sigma = m_s/m_w = 10$, wall size $\omega_1/p = 10$; and preyielding period of $T_1 = 0.8s$ when subjected to the Pacoima Dam/164 ground motion recorded during the 1971 San Fernando, California earthquake. (b) Time-history analysis of a nonlinear SDOF oscillator with a pinned rocking wall with same parameters and excitation as in (a). 32

Figure 2.4: (a) Time-history analysis of a nonlinear SDOF oscillator coupled with a stepping rocking wall with normalized strength $Q/m_s = 0.15g$, mass ratio $\sigma = m_s/m_w = 10$, wall size $\omega_1/p = 10$; and preyielding period of $T_1 = 0.8s$ when subjected to the Takarazuka/000 ground motion recorded during the 1995 Kobe, Japan earthquake. (b) Time-history analysis of a nonlinear SDOF oscillator with a pinned rocking wall with same parameters and excitation as in (a). 33

Figure 2.5: (a) Time-history analysis of a nonlinear SDOF oscillator coupled with a stepping rocking wall with normalized strength $Q/m_s = 0.08g$, mass ratio $\sigma = m_s/m_w = 10$, wall size $\omega_1/p = 10$; and preyielding period of $T_1 = 1.5s$ when subjected to the Erzincan NS ground motion recorded during the 1992 Erzincan, Turkey earthquake. (b) Time-history analysis of a nonlinear SDOF oscillator with a pinned rocking wall with same parameters and excitation as in (a). 34

Figure 2.6: (a): Four-story, two-bay yielding frame, with pre-yielding period $T_1 = 0.5sec$ coupled with a stepping rocking wall with $p = 0.952 \text{ rad/sec}$, $\omega_1/p = 13.2$ and $\sigma = m_s/m_w = 5$, (b): pushover curve for frame compared to hysteretic loop of SDOF idealization, response comparison when subjected to the 1971 Pacoima Dam/164 ground motion (c) and the 1995 Takarazuka/000 ground motion (d). Heavy solid lines: OpenSees solution; thin lines: MATLAB solution of the SDOF response. 36

Figure 2.7: (a): Four-story, two-bay yielding frame, with pre-yielding period $T_1 = 0.5sec$ coupled with a pinned rocking wall with $p = 0.952 \text{ rad/sec}$, $\omega_1/p = 13.2$ and $\sigma = m_s/m_w = 5$, (b): pushover curve for frame compared to hysteretic loop of SDOF idealization, response comparison when subjected to the 1971 Pacoima Dam/164 ground motion (c) and the 1995 Takarazuka/000 ground motion (d). Heavy solid lines: OpenSees solution; thin lines: MATLAB solution of the SDOF response. 37

Figure 2.8: Peak displacement (a, c, e, g) and residual displacement (b, d, f, h) spectra of a yielding SDOF oscillator coupled with a stepping wall (a, b, e, f) and pinned wall (c, d, g, h) for two values of the strength, $Q/m_s = 0.15g$ (a, b, c, d) and $Q/m_s = 0.08g$ (e, f, g, h) with, mass ratio, $\sigma = m_s/m_w = 5$ and 20 and wall size, $\omega_1/p = 10$, when subjected to the Pacoima Dam/164 ground motion recorded during the 1971 San Fernando, California earthquake. 39

Figure 2.9: Peak displacement (a, c, e, g) and residual displacement (b, d, f, h) spectra of a yielding SDOF oscillator coupled with a stepping wall (a, b, e, f) and pinned wall (c, d, g, h) for two values of the strength, $Q/m_s = 0.15g$ (a, b, c, d) and $Q/m_s = 0.08g$ (e, f, g, h) with, mass ratio, $\sigma = m_s/m_w = 5$ and 20 and wall size, $\omega_1/p = 10$, when subjected to the Takarazuka/000 ground motion recorded during the 1995 Kobe, Japan earthquake. 40

Figure 2.10: Displacement spectra of an elastic SDOF oscillator coupled with a stepping wall (left) and a pinned wall (right) for three values of the mass ratio $\sigma = m_s/m_w = 5, 10$ and 20 and two values of the wall size, $\omega_o/p = 10$ and 15 when subjected to the CO2/065 ground motion recorded during the 1966 Parkfield, California earthquake (bottom). 43

Figure 2.11 Displacement spectra of an elastic SDOF oscillator coupled with a stepping wall (left) and a pinned wall (right) for three values of the mass ratio $\sigma = m_s/m_w = 5, 10$ and 20 and two values of the wall size, $\omega_o/p = 10$ and 15 when subjected to the Pacoima Dam/164 ground motion recorded during the 1971 San Fernando, California earthquake (bottom). 44

Figure 2.12 Displacement spectra of an elastic SDOF oscillator coupled with a stepping wall (left) and a pinned wall (right) for three values of the mass ratio $\sigma = m_s/m_w = 5, 10$ and 20 and two values of the wall size, $\omega_o/p = 10$ and 15 when subjected to the Takarazuka/000 ground motion recorded during the 1995 Kobe, Japan earthquake (bottom). 46

Figure 2.13 Normalized displacement spectra (u/R) of a SDOF oscillator coupled with a stepping wall (left) and a pinned wall (right) for three values of the mass ratio $\sigma = m_s/m_w = 5, 10$ and 20 and two values of the wall size, $\omega_o/p = 10$ and 15 when subjected to a symmetric Ricker wavelet with $a_p = 0.5g$ 49

Figure 2.14 Normalized displacement spectra (u/R) of a SDOF oscillator coupled with a stepping wall (left) and a pinned wall (right) for three values of the mass ratio $\sigma = m_s/m_w = 5, 10$ and 20 and two values of the wall size, $\omega_o/p = 10$ and 15 when subjected to a symmetric Ricker wavelet with $a_p = 1.0g$ 50

Figure 2.15 Displacement spectra of an elastic SDOF oscillator coupled with a stepping wall (left) and a pinned wall (right) with a short coupling arm for two values of the mass ratio $\sigma = m_s/m_w = 5$ (top) and 20 (bottom) and the wall size, $\omega_o/p = 10$ and three values of the length of the coupling arm, $L = \infty, b$ and $b/10$ when subjected to Pacoima Dam/164 ground motion recorded during the 1971 San Fernando, California earthquake. 54

Figure 2.16 Displacement spectra of an elastic SDOF oscillator coupled with a stepping wall (left) and a pinned wall (right) with a short coupling arm for two values of the mass ratio $\sigma = m_s/m_w = 5$ (top) and 20 (bottom) and the wall size, $\omega_o/p = 10$ and three values of the length of the coupling arm, $L = \infty, b$ and $b/10$ when subjected to Takarazuka/000 ground motion recorded during the 1995 Kobe, Japan earthquake. 55

Figure 3.1: Yielding single-degree-of-freedom oscillator coupled with a vertically restrained stepping rocking wall. 59

Figure 3.2: Free-body diagram of a rocking wall with an elastic tendon passing through its center-line. 65

Figure 3.3: Time-history analysis of a nonlinear SDOF oscillator coupled with a vertically restrained stepping rocking wall with preyielding period, $T_1 = 0.8$ sec, normalized strength $Q/m_s = 0.08g$, wall size ratio, $\omega_1/p = 10$ and structure-to-wall mass ratio, $\sigma = 10$ when subjected to the 1971 Pacoima Dam/164 ground motion (left) and the 1992 Erzincan NS, Turkey ground motion (right). Even stiff tendons ($EA/m_w g = 200$) have a marginal effect on the response, except of drastically increasing the vertical reaction (more than 50%) at the pivot points. Tendons are not prestressed, $P_o/m_w g = 0$ 68

Figure 3.4: Time-history analysis of a nonlinear SDOF oscillator coupled with a vertically restrained stepping rocking wall with preyielding period, $T_1 = 1.5$ sec, normalized strength $Q/m_s = 0.12g$, wall size ratio, $\omega_1/p = 10$ and structure-to-wall mass ratio, $\sigma = 10$ when subjected to the 1971 Pacoima Dam/164 ground motion (left) and the 1992 Erzincan NS, Turkey ground motion (right). Even stiff tendons ($EA/m_w g = 200$) have a marginal effect on the response, except of drastically increasing the vertical reaction (more than 50%) at the pivot points. Tendons are not prestressed, $P_o/m_w g = 0$ 69

Figure 3.5: Time-history analysis of a nonlinear SDOF oscillator coupled with a vertically restrained stepping rocking wall with preyielding period, $T_1 = 1.5$ sec, normalized strength $Q/m_s = 0.12g$, wall size ratio, $\omega_1/p = 10$ and structure-to-wall mass ratio, $\sigma = 10$ when subjected to the 1994 Newhall/360 ground motion (left) and the 1995 Takarazuke/000, Japan ground motion (right). Even stiff tendons ($EA/m_w g = 200$) have a marginal effect on the response, except of drastically increasing the vertical reaction (more than 50%) at the pivot points. Tendons are not prestressed, $P_o/m_w g = 0$ 70

Figure 3.6: Top: Nine-story moment-resisting steel frame designed for the SAC Phase II Project coupled with a stepping rocking wall. Bottom: Geometric and physical characteristics pertinent to the 9-story SAC building. 72

Figure 3.7: (a): Comparison of the computed push-over curve (base-shear vs roof displacement) of the 9-story moment-resisting steel building with the results reported by [80]. Base-shear versus displacement at mid-height computed with OpenSees of the 9-story steel building without rocking wall together with the corresponding force-displacement loops computed with MATLAB of the SDOF inelastic model shown in Figure 1 when excited with the 1994 Newhall/360, Northridge (b), the 1992 Erzincan NS, Turkey (c), the 1995 Takarazuka/000, Kobe (d) and the 1971 Pacoima Dam/164, Imperial Valley (e) ground motions. 73

Figure 3.8: Comparison of the displacement time histories at mid-height of the 9-story steel building shown in Figure 6, computed with OpenSees with the displacement time-histories of the SDOF idealization shown in Figure 1, when excited with the 1971 Pacoima Dam/164, San Fernando, California (left) and the 1992 Erzincan NS, Turkey (right) ground motions. 74

Figure 3.9: Comparison of the displacement time histories at mid-height of the 9-story steel building shown in Figure 6, computed with OpenSees with the displacement time-histories of the SDOF idealization shown in Figure 1, when excited with the 1994 Newhall/360, Northridge, California (left) and the 1995 Takarazuka/000, Kobe, Japan (right) ground motions. 75

Figure 3.10 Displacement spectra of a yielding SDOF oscillator coupled with a vertically restrained stepping rocking wall with slenderness $\tan \alpha = 1/6$, for two valued of strength, $Q/m_s = 0.15g$ (left column) and $Q/m_s = 0.08g$ (right column) with mass ratios, $\sigma = 5, 10$ and ∞ (no wall); several values of tendon stiffness ($EA/m_w g = 0, 40, 72$ and 200) with ($P_o = m_w g$) and without ($P_o = 0$) pre-tensioning when subjected to the Newhall/360 ground motion recorded during the 1994, Northridge California earthquake. 77

Figure 3.11 Displacement spectra of a yielding SDOF oscillator coupled with a vertically restrained stepping rocking wall with slenderness $\tan \alpha = 1/6$, for two valued of strength, $Q/m_s = 0.15g$ (left column) and $Q/m_s = 0.08g$ (right column) with mass ratios, $\sigma = 5, 10$ and ∞ (no wall); several values of tendon stiffness ($EA/m_w g = 0, 40, 72$ and 200) with ($P_o = m_w g$) and without ($P_o = 0$) pre-tensioning when subjected to the Pacoima Dam/164 ground motion recorded during the 1971 San Fernando, California earthquake. 78

Figure 3.12 Displacement spectra of a yielding SDOF oscillator coupled with a vertically restrained stepping rocking wall with slenderness $\tan \alpha = 1/6$, for two values of strength, $Q/m_s = 0.15g$ (left column) and $Q/m_s = 0.08g$ (right column) with mass ratios, $\sigma = 5, 10$ and ∞ (no wall); several values of tendon stiffness ($EA/m_w g = 0, 40, 72$ and 200) with ($P_o = m_w g$) and without ($P_o = 0$) pre-tensioning when subjected to the Erzincan NS ground motion recorded during the 1992 Erzincan, Turkey earthquake. 79

Figure 4.1: (a) Moment-resisting frame coupled with a stepping rocking wall with vertical supplemental dampers as was introduced by James M Kelly, et al. 1972, (b) A single-degree-of-freedom idealization of a yielding oscillator coupled with a stepping rocking wall with supplemental dampers. 83

Figure 4.2: Geometric quantities pertinent to the dynamic analysis of a rocking wall with additional energy dissipators. 85

Figure 4.3: Reduction of the lever arm r_1 of the damping force across the pivoting point (a) and lever arm of the damping force next to the pivoting point (b) as a function the column rotation θ 89

Figure 4.4: Example of torsionally yielding steel-beam damper installed at the base of the stepping pier of the South Rangitikei Rail Bridge in New Zealand which delivers a yield force of $2 \times 45kN$ which is equivalent to $\frac{k_d u_y}{m_w g} = 0.05$ 91

Figure 4.5: Time history analysis of a nonlinear SDOF oscillator coupled with a step-
 ping rocking wall with normalized strength $Q/m_s = 0.15g$, mass ratio, $\sigma =$
 $m_s/m_w = 5$, wall size, $\omega_1/p = 10$, and pre-yielding period of $T_1 = 0.8sec$,
 when subjected to the Newhall/360 ground motion recorded during the 1994
 Northridge, California earthquake. Thin lines: No wall, Heavy solid lines:
 (thinner) with wall and no dampers (heavier) wall with hysteretic ($k_d u_y/m_w g =$
 5%) (left) and linear viscous ($C/m_w p = 2.8$) (right) zero-length dampers.
 Bottom: Force-displacement loops of the hysteretic (left) and linear (right)
 dampers installed at each leg of the rocking wall. 93

Figure 4.6: Time history analysis of a nonlinear SDOF oscillator coupled with a step-
 ping rocking wall with normalized strength $Q/m_s = 0.15g$, mass ratio, $\sigma =$
 $m_s/m_w = 5$, wall size, $\omega_1/p = 10$, and pre-yielding period of $T_1 = 0.8sec$,
 when subjected to the Newhall/360 ground motion recorded during the 1994
 Northridge, California earthquake. Thin lines: No wall, Heavy solid lines:
 (thinner) with wall and no dampers (heavier) wall with hysteretic ($k_d u_y/m_w g =$
 5%) (left) and linear viscous ($C/m_w p = 2.8$) (right) dampers located at $d =$
 $0.1b$ and $L = 0.2h$. Bottom: Force-displacement loops of the hysteretic (left)
 and linear (right) dampers installed at each leg of the rocking wall. 95

Figure 4.7: Time history analysis of a nonlinear SDOF oscillator coupled with a stepping rocking wall with normalized strength $Q/m_s = 0.08g$, mass ratio, $\sigma = m_s/m_w = 5$, wall size, $\omega_1/p = 10$, and pre-yielding period of $T_1 = 1.2sec$, when subjected to the REHS ground motion recorded during the 2011 Christchurch, New Zealand earthquake. Thin lines: No wall, Heavy solid lines: (thinner) with wall and no dampers (heavier) wall with hysteretic ($k_d u_y/m_w g = 5\%$) (left) and linear viscous ($C/m_w p = 2.8$) (right) zero-length dampers. Bottom: Force-displacement loops of the hysteretic (left) and linear (right) dampers installed at each leg of the rocking wall. 96

Figure 4.8: Peak response of SDOF yielding oscillator coupled with a stepping wall with slenderness $\tan \alpha = 1/6$ with zero-length supplemental viscous dampers ($q=1$) appended at the pivoting points ($d=0$) when excited by the three strong ground motions presented earlier in this study. Figures on the left are corresponding to stronger oscillator with strength of $Q/m_s = 0.15g$ and on the right with an oscillator with strength of $Q/m_s = 0.08g$ 98

Figure 4.9: Peak response of SDOF yielding oscillator coupled with a stepping wall with slenderness $\tan \alpha = 1/6$ with zero-length supplemental hysteretic dampers appended at the pivoting points ($d=0$) when excited by the three strong ground motions presented earlier in this study. Figures on the left are corresponding to stronger oscillator with strength of $Q/m_s = 0.15g$ and on the right with an oscillator with strength of $Q/m_s = 0.08g$ 99

Figure 4.10 Peak response of SDOF yielding oscillator coupled with a stepping wall with slenderness $\tan \alpha = 1/6$ with supplemental viscous dampers ($q=1$) with length of ($l = 0.2h$) installed along the sides of the rocking wall at the distance ($d = 0.1b$) when excited by the three strong ground motions presented earlier in this study. Figures on the left are corresponding to stronger oscillator with strength of $Q/m_s = 0.15g$ and on the right with an oscillator with strength of $Q/m_s = 0.08g$ 101

Figure 4.11 Peak response of SDOF yielding oscillator coupled with a stepping wall with slenderness $\tan \alpha = 1/6$ with supplemental hysteretic dampers with length of ($l = 0.2h$) installed along the sides of the rocking wall at the distance ($d = 0.1b$) when excited by the three strong ground motions presented earlier in this study. Figures on the left are corresponding to stronger oscillator with strength of $Q/m_s = 0.15g$ and on the right with an oscillator with strength of $Q/m_s = 0.08g$ 102

Figure 4.12 Time history analysis of a solitary stepping rocking wall size $\tan \alpha = 1/6$ with supplemental hysteretic dampers with normalized strength of $k_d u_y / m_w g = 0.05$ attached at the pivoting points when subjected to the sine pulse with $t_p = 0.5sec$ and $a_p = 0.5g$ 104

Figure 4.13 Time history analysis of a solitary stepping rocking wall size $\tan \alpha = 1/6$ with supplemental linear viscous dampers with $C = 6667 \text{ kN}\cdot\text{sec}/\text{m}$ attached at the pivoting points when subjected to the sine pulse with $t_p = 0.5sec$ and $a_p = 0.5g$ 105

Figure 4.14(a) View of the South Rangitikei Rail Bridge in New Zealand and (b) close-up view of the rocking interface. The piers are allowed to uplift by 12.5 cm; while the rocking motion is controlled by torsionally yielding steel-beam damper shown below. (c) Detail of the torsionally yielding steel-beam damper installation at the base of the stepping piers atop the pile cap that delivers a yield force of $2 \times 45\text{kN}$. (d) Schematic of the torsionally yielding steel-beam damper. 109

Figure 4.15 Schematic of the stepping center pier of the South Rangitikei Rail Bridge (a) together with the geometric parameters needed for planar dynamic response analysis (b). 111

Figure 4.16 Rotation and angular velocity time histories of the 72.7m tall center pier of the South Rangitikei Rail Bridge when subjected to the North-South component of the El Centro ground motion recorded during the 1940 Imperial Valley, California earthquake (left) and the CO2/064 ground motion recorded during the 1966 Parkfield, California earthquake (right). Thin lines: No dampers. Heavy solid lines: Hysteretic dampers with $k_d u_y / (mg) = 5\%$. Bottom: Force-displacement loops of the 900kN hysteretic dampers installed at each leg of the pier. Positive rotation is clockwise.). 114

Figure 4.17 Rotation and angular velocity time histories of the 72.7m tall center pier of the South Rangitikei Rail Bridge when subjected to the Pacoima Dam/164 ground motion recorded during the 1971 San Fernando, California earthquake (left) and the North-South component of the ground motion recorded during the 1992, Erzincan, Turkey earthquake (right). Thin lines: No dampers. Heavy solid lines: Hysteretic dampers with $k_d u_y / (mg) = 5\%$. Bottom: Force-displacement loops of the 900kN hysteretic dampers installed at each leg of the pier. Positive rotation is clockwise. 118

Figure 4.18 Rotation and angular velocity time histories of the 72.7m tall center pier of the South Rangitikei Rail Bridge when subjected to the Newhall/360 ground motion recorded during the 1994 Northridge, California earthquake. Thin lines: No dampers. Heavy solid lines: Hysteretic dampers with $k_d u_y / (mg) = 5\%$ (left) and linear viscous dampers with $C / (mp) = 5.7$ (right). Bottom: Force-displacement loops of the 900kN hysteretic (left) and linear viscous (right) dampers installed at each leg of the pier. Positive rotation is clockwise. 120

Figure 4.19 Rotation and angular velocity time histories of the 72.7m tall center pier of the South Rangitikei Rail Bridge when subjected to the REHS ground motion recorded during the 2011 Christchurch, New Zealand earthquake. Thin lines: No dampers. Heavy solid lines: Hysteretic dampers with $k_d u_y / (mg) = 5\%$ (left) and linear viscous dampers with $C / (mp) = 4.3$ (right). Bottom: Force-displacement loops of the 900kN hysteretic (left) and linear viscous (right) dampers installed at each leg of the pier. Positive rotation is clockwise. . . . 123

Figure 4.20 Rocking spectra of free-standing columns with slenderness, $\tan \alpha = 1/6$ with various levels of supplemental damping appended at their pivoting points when subjected to a symmetric Ricker wavelet with acceleration amplitude, $a_p = 0.35g$ (plots (a) and (b)) and $a_p = 0.5g$ (plots (c) and (d)). 126

Figure 4.21 Rocking spectra of free-standing columns with slenderness, $\tan \alpha = 1/6$ with various levels of supplemental damping appended at their pivoting points when subjected to an antisymmetric Ricker wavelet with acceleration amplitude, $a_p = 0.35g$ (plots (a) and (b)) and $a_p = 0.5g$ (plots (c) and (d)). 127

Figure 4.22 Peak rotation as a function of the size of free-standing columns with slenderness $\tan \alpha = 1/6 = 0.167$ with zero-length supplemental hysteretic dampers appended at the pivoting points ($d = 0$) when excited by the six strong ground motions presented in this study. 128

Figure 4.23 Peak rotation as a function of the size free-standing columns with slenderness $\tan \alpha = 1/6 = 0.167$ with zero-length supplemental viscous dampers ($q = 1$) appended at the pivoting points ($d = 0$) when excited by the six strong ground motions presented in this study. 129

Figure 4.24 Peak rotation as a function of the size of free-standing columns with slenderness $\tan \alpha = 1/6 = 0.167$ with supplemental hysteretic dampers with length ($l = 0.2h$) installed along the sides of the rocking columns at a distance ($d = 0.1b$) when excited by the six strong ground motions presented in this study. 131

Figure 4.25	Peak rotation as a function of the size of free-standing columns with slender-	
	ness $\tan \alpha = 1/6 = 0.167$ with supplemental viscous dampers ($q = 1$) with	
	length ($l = 0.2h$) installed along the sides of the rocking columns at a dis-	
	tance ($d = 0.1b$) when excited by the six strong ground motions presented in	
	this study.	132

LIST OF TABLES

Table 1.1: Comparison of monolithic vs. hybrid walls (prestressed rocking wall with energy dissipators)	10
---	----

CHAPTER 1: INTRODUCTION

Overview

In the wake of significant damage and partially collapse of the Olive View Hospital after 1971 San Fernando, California earthquake (Figure 1.1), Bertero et al. [1] directed attention of engineers to coherent acceleration pulses (0.8-1.5 sec duration at that time) which result in large monotonic velocity increments and impose severe deformation demands on structures. Almost two decades later, after 1994 Northridge, California earthquake followed by 1995 Kobe, Japan earthquake, such coherent acceleration pulses received revived attention. Makris [2], Alavi and Krawinkler [3] and Makris and Cheng [4] studied the destructive potential of pulse-like ground motions recorded near the causative fault of earthquakes.



Figure 1.1: Weak Story Failure of Olive View Hospital after 1971 San Fernando, CA Earthquake.

In order to eliminate the generation of weak story failure Meek [5] suggested coupling a rocking wall to a moment resisting frame. Also, during the last two decades, precast shear walls have been promoted as seismic resisting systems for structures in seismic areas (PCI Ad Hoc Committee on

Precast Walls [6]). As early as the PRESSS Program [7, 8], the jointed shear wall system was allowed to lift-off and rock [9, 10]. About the same time Kurama et al. [11, 12] examined the lateral load behavior of unbonded segmented post-tensioned precast concrete walls while, Mander and Cheng [13] introduced the damage avoidance design (DAD) in which the free-standing piers of a bridge frame are only vertically restrained through their center line and are allowed to rock atop the pile-cap and below the pier-cap beam without inducing any damage.



Figure 1.2: Weak Story Failure of Marshal Hotel after 2018 Hualien, Taiwan Earthquake.

Following the PRESSS program, Holden et al. [14] presented experimental studies on the cyclic loading of a precast partially prestressed system that incorporated post-tensioned unbonded tendons and steel reinforced concrete. In this experimental study supplemental hysteretic energy dissipation devices were also provided. The Holden et al. [14] study concluded that the precast, partially prestressed rocking wall achieved drift levels well in excess of 3% with no visible damage; while, it offers a comprehensive literature review on the work on rocking walls up to the time of its publication. Ajrab et al. [15] presented a performance-based design methodology for the frame-building-rocking-wall system with various prestressed tendon configurations and energy dissipation devices. In their proposed methodology Ajrab et al. [15] adopt an "equivalent-static" lateral force procedure, and the study concludes that the proposed performance-based, capacity-demand method predicts larger displacements than those obtained from time-history analysis.

Experimental and analytical studies on the response of a frame-building-rocking-wall system were also presented by Lu [16] who included 3-D effects in the analysis; while, Toranzo et al. [17] tested a 2/5 scale reinforced concrete frame coupled with a confined-masonry rocking wall. The Toranzo et al. [17] study focused on bringing forward the advantages of low-cost rocking wall-reinforced concrete frames including their ability of recentering due to the gravity force acting on the stepping rocking wall.

Following the early concepts advanced by Alavi and Krawinkler 2004 [18], Wada et al. [19] and Qu et al. [20] proposed a pinned rocking wall for the seismic protection of an 11-story reinforced concrete building. The main motivation for the proposed study was the avoidance of a weak story failure of the RC frame. The novelty in the Wada et al. [19] study (further expanded in the Qu et al. [20]) is that the rocking wall does not alternate pivot points (it is not a stepping wall) given that it is supported on a specially designed pin bearing to avoid potentially unfavorable impact at the pivoting corners. With this design the system does not enjoy any recentering action; while, the weight of the wall works against stability. Clearly, the post-tensioning of the rocking wall only increases the cracked strength of the wall, rather than providing any self-centering action. In the Wada et al. [19] and Qu et al. [20] studies much emphasis is placed on the energy dissipation by the supplemental steel dampers; while, no comments are offered to what extent the mobilization of the rotational inertia of the 11-story height shear walls are modifying the dynamic response of the coupled reinforced concrete structure. Following the Wada et al. [19] and Qu et al. [20], studies several publications appeared to promote the seismic protection of a moment resisting frame structure when coupled with a rocking wall (Hu, et al. [21], Nicknam and Filiatrault [22], Grigorian and Grigorian [23, 24] among others). In addition to these studies, a recent paper by Kurama et al. [25] reviewed the state of the art of precast concrete structure advances and it concludes that the widespread use of precast concrete in seismic regions is feasible today and the new innovative techniques that introduces through these studies led to improved seismic performance of buildings

and bridges.

Most of these aforementioned studies introduce the unique advantages of rocking action by referencing the seminal paper by Housner [26], who noticed that tall, slender, free-standing columns, while they can easily uplift even when subjected to a moderate ground acceleration (uplifting initiate when $\ddot{u}_g > g \frac{base}{height}$); they exhibit remarkable seismic stability due to a size-frequency scale effect. In his 1963 paper Housner shows that there is a safety margin between uplifting and overturning and that as the size of the free-standing column increases or the frequency of the excitation pulse increases, this safety margin increases appreciably to the extent that large free-standing columns enjoy ample seismic stability. Recently, Makris [27, 28] explained that as the size of the free-standing rocking column increases, the enhanced seismic stability primarily originates from the difficulty to mobilize the rotational inertia of the column (wall) which increases with the square of the column (wall) size. Further studies by Makris and Vassiliou [29] and Vassiliou and Makris [30] showed that as the size of the column (wall) increases, the resistance to mobilize the rotational inertia increases to such an extent, that the effect of vertical tendons becomes increasingly marginal.

The motivation for coupling of a moment-resisting frame with a strong rocking wall is to primarily enforce a uniform distribution of interstory drifts; therefore, the first mode of the frame becomes dominant as was first indicated in the seminal paper by Alavi and Krawinler [18]. Further analytical evidence to the first-mode dominated response is offered in the Qu et al. [20] paper. These results together with additional evidence by other investigators were critically evaluated in a recent paper by Grigorian and Grigorian [23] who concluded that a moment resisting frame coupled with a rocking wall can be categorized as a single-degree-of-freedom (SDOF) system. Accordingly, in this study we adopted the SDOF idealization shown in Figure 2.1 and 2.2.

Dynamics of a Rocking Column

Seismic stability of a tall free standing solitary column was studied in Housner [26] seminal paper. In that paper size-frequency scale effect of the rocking column is introduced and showed why the larger of two geometrically similar blocks survives an excitation that will topple the smaller block, and of two acceleration pulses with the same amplitude, the one with the longer duration is more capable of overturning [31]. Following Housner's 1963 study other researchers showed that the uplifting and rocking of a solitary free-standing column has a beneficial effect to the seismic resistance of such members [32–36].

In this section a brief overview of equation of motion for a rocking block is discussed. The schematic of the rocking block is shown in Figure 1.3.

Considering the Figure 1.3, if the friction is big enough, the block can oscillate without sliding about pivoting points of O and O' when it is set to rocking. Center of gravity and geometry is in distance of R from pivoting points.

Under positive ground acceleration \ddot{u}_g , the block will rotate with a negative rotation (In order to rocking motion to be initiated, $\ddot{u}_g > g \tan \alpha$). And if it does not overturn, it will eventually resume to positive rotation. Equation of motion when there is only horizontal acceleration expressed as:

$$I\ddot{\theta} + mgR \sin(-\alpha - \theta) = -m\ddot{u}_g R \cos(-\alpha - \theta), \quad \theta < 0 \quad (1.1)$$

and

$$I\ddot{\theta} + mgR \sin(\alpha - \theta) = -m\ddot{u}_g R \cos(\alpha - \theta), \quad \theta > 0 \quad (1.2)$$

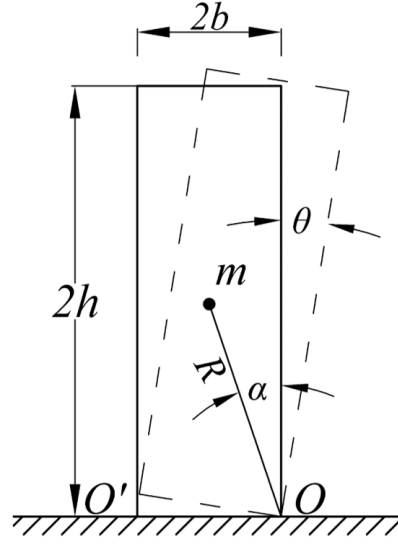


Figure 1.3: Schematic of a Rocking Block.

In which, for rectangular blocks, $I = 4/3mR^2$, $\alpha = \tan^{-1}(b/h)$ and $R = \sqrt{b^2 + h^2}$. Above equations can be expressed in the following compact format.

$$\ddot{\theta} = -p^2 \left[\sin(\alpha \operatorname{sgn}(\theta(t)) - \theta(t)) + \frac{\ddot{u}_g}{g} \cos(\alpha \operatorname{sgn}(\theta(t)) - \theta(t)) \right] \quad (1.3)$$

Frequency of oscillation for a rigid rocking block under free vibration is not constant, and it is dependent on the amplitude of vibration. However, $p = \sqrt{3g/4R}$ is a measure of dynamics characteristics of the block

Figure 1.4 shows the moment-rotation relationship during the rocking motion of a free-standing block. The system has infinite stiffness until the magnitude of the applied moment reaches the value $mgR \sin \alpha$, and once the block is rocking, its restoring force decrease monotonically, reaching zero when $\theta = \alpha$.

This negative stiffness which is inherent in rocking systems, is most attractive in earthquake en-

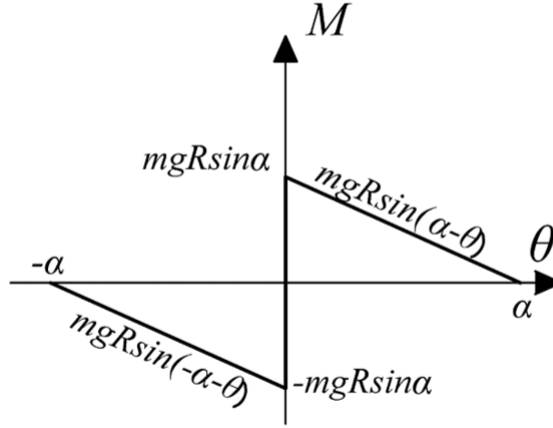


Figure 1.4: Moment-rotation diagram of a rocking block.

gineering in terms of keeping base shears and moments low [37], provided that the rocking block remains stable, thus the need for a formula that will offer a safe design value for its slenderness.

Since the moment-rotation curve follows the same curve that shown in Figure 1.4, and there is no enclosing area, the only source of energy dissipation is the energy loss during the impact, when the pivoting points changed. The ratio of kinetic energy before and after impact is

$$r = \frac{\dot{\theta}_2^2}{\dot{\theta}_1^2} \quad (1.4)$$

It means that angular velocity after the impact is \sqrt{r} times of the velocity before the impact. Considering conservation of angular momentum before and after impact, it gives

$$r = \left(1 - \frac{3}{2}\sin^2\alpha\right)^2 \quad (1.5)$$

Rocking Wall and Frame in Literature

One of the early works that studied the possibility of a core shear wall that is able to rock, is the work by Meek [5]. Inspired by the seminal work on rocking blocks by Housner [26] this study used a simplified analysis of the core rocking wall and a frame when the wall and footing rock on the soil. In this study it was showed that tipping (rocking) wall greatly reduces the base shear and the moment and the base of the wall when it compared conventional to fixed-base shear walls.

Later in early 1990s, a coordinated research program between United States and Japan was initiated [7]. The Precast Seismic Structural System (PRESSS) program included many individual projects and it was followed by a design and testing of a five-story precast building [8–10]. These studies established the basis for further researches in the US.

Kurama et al. [11, 12, 38] investigated behavior of unbonded post-tensioned precast concrete walls. In these studies, a design procedure based on idealized trilinear base-shear-roof-drift relationship is proposed. In these study, a trilinear relation is used to define base-shear-roof-drift relation and effect of rotational inertia is not considered. The trilinear relation consists of 4 stages; decompression state (when wall starts the uplift), softening state (linear limit either governed by gap opening of the walls or nonlinear behavior of concrete in compression), yielding state (at this state strain in post-tensioning steel first reaches the linear simit strain) and failure state (in which wall fails) are defined. Kurama et al. [12] verifies the analytical model using test results of National Institute of Standards and Technology (NIST) [39]. The verification of the analytical model compared with test results shows that the analytical model is reasonably agreed with the test in loading; however, the model is not accurate in unloading phase. This paper concluded that the post-tensioned precast walls are feasible alternative to cast in place walls. These walls can undergo large displacement with minor damages. Whats more, precast walls have almost no residual displacement. Additionally, in Kurama et al. [11] using equal displacement assumption in the analytical model of this

study drift results of the model is not predicting the experiment results correctly.

Holden et al. [14] compared behavior of monolithic reinforced concrete walls with prestressed concrete walls using reversed cyclic quasi-static lateral loading. In this study two geometrically identical (half-scale) concrete wall were tested under quasi-static analysis. One wall was conventional reinforced fixed-end shear wall and the second specimen was a partially prestressed precast wall which was free to uplift and rock on the pivoting points. The precast wall was also equipped with hysteretic energy dissipating devices. For the rocking wall in this study assumed a bilinear elastic behavior which is inspired by the damage avoidance design (DAD) paradigm [13] and it ignores effects of walls mass inertia. In this study it was assumed that after uplifting, systems stiffness is attained from strain-hardening stiffness in energy dissipaters and stiffness of the tendons. Results from this study shows that partially prestressed rocking wall with energy dissipating devices achieved drift level on excess of 3% with no visible damage. This study mostly focused on the advantages of self-centering walls over monolithic shear walls in terms of damage to walls after lateral loadings and residual displacement comparison, Table 1-1 from Holden et al. [14] shows a good comparison between monolithic and prestressed walls.

Ajrab et al. [15] analyzed a rocking wall-reinforced concrete frame system with additional tendon system and dampers. Total damping of the system is assumed to be summation of structural damping, equivalent viscous damping caused by wall and foundation impact, hysteretic damping caused by inelastic action in the frame and additional damping due to supplemental damping devices. In order to calculate lateral capacity demand of the rocking wall-frame system this study adopted a capacity design approach. In the pre-rocking stage, the system behavior governed by structural flexibility, when uplifting of the wall initiated, based on the equilibrium of internal and external works, the base shear capacity of the system is calculated without considering effect of rotational inertia of the rocking wall. Then overall performance of the structure under MCE (Maximum Considered Earthquake) and MAE (Maximum Assumed Earthquake) is compared with the maxi-

Table 1.1: Comparison of monolithic vs. hybrid walls (prestressed rocking wall with energy dissipators)

System property	Monolithic	Hybrid
Energy dissipation capacity	Excellent	Good
Special reinforcing detailing	In potential plastic hinge zones. Congested cages to confine the concrete, prevent longitudinal reinforcing from buckling, and to prevent shear failure.	Only required at wall ends and foundation beam where rocking takes place.
Dimensional limitations	To prevent plastic hinge instability	Minimum—based on elastic theory as wall panels remain essentially crack-free
Minimum reinforcement requirements	Can significantly increase the moment capacity at the critical region. This could result in larger foundations as a result of capacity design	Temperature and shrinkage can be substituted with fiber reinforced concrete
Expected postearthquake repair work	In plastic hinge zones repair work can vary from epoxy injection of 1 mm wide cracks or less, to concrete replacement. Longitudinal bars could buckle and fracture requiring demolition. Permanent deformations.	None expected. Self-centering, permanent deflections are not expected.
Initial cost	Competitive—widely used systems	Competitive? Requires cost analysis.
Life-cycle cost	Competitive relative to other conventional systems. May require postearthquake repair, or following a severe earthquake demolition and rebuilding may be necessary.	Expected to be very competitive. No postearthquake repairs needed.

imum displacement of the structure, calculated using time-history analysis. The results of designed structure under different ground motions showed that the adopted capacity-demand method predicts larger displacements in comparison to what was obtained from time-history analysis. Also, response of an analytical structure with proposed rocking wall-damper system to 1970 Pacoima Dam S18W ground motion is analyzed and compared with the fixed end wall. The results show that the proposed wall-frame system with dampers has smaller roof displacement. Additionally, inter-story drifts are also reduced and became more uniformly distributed through the height of the building.

About the same time to strengthen moment-resisting frames to near-fault ground motion effects, Alavi and Krawinkler [18] introduced pinned rocking wall system. Because of the nature of near-fault ground motion which cause a highly non-uniform distribution of story ductility demand, in this study effects of coupling MRFs to pinned rocking wall was investigated and it concluded that

strengthening with pinned wall is effective and reduces drift demands of structures with a wide range of periods and various performance levels.

In their study, Filiatrault et al. [40] reviewed self-centering structural systems and discussed advantages of such structures over conventional structural systems in terms of cost, resilience and serviceability after major earthquakes. The paper points the main advantages of these systems as: their large lateral displacement capacity, the lack of structural damage associated with large displacements and their ability to return to the original position upon unloading.

Lu, Y [16] studied behavior of rocking wall-frame system considering its 3D effect. Purpose of the study was modeling wall's neutral axis migration and showing its significance and assessment of 3D effect of the wall in order to control it. This study showed that the uncontrolled wall rocking can cause beam-wall connection failures. In this study planar six story high wall-frame system is also tested under different ground motions. Experiment's main objective was to assess response of the wall-frame system which was designed using Eurocode 8. In this paper test result showed that approximately 80% of the first-story lateral drift was attributed to the wall rigid body rotation about its pivoting points during inelastic response. In this study also, an analytical model of the tested building was investigated. In analytical model walls were modeled as columns and there is no consideration of how wall's inertia was implemented.

Restrepo and Rahman [41] investigated performance of prestressed self-centering walls with and without additional energy dissipators. Prototype wall tested under quasi-static reversed cyclic loading. In contrast with previous works of Kuramma et al. [11, 12, 38] and Holden et al. [14], instead of trilinear representation of lateral load-displacement relationship, this study utilizes a bi-linear representation. The experiments showed no residual displacement in rocking walls even when the system had no energy dissipators installed and in prestressed wall with dissipators, flag-shaped hysteresis behavior was observed.

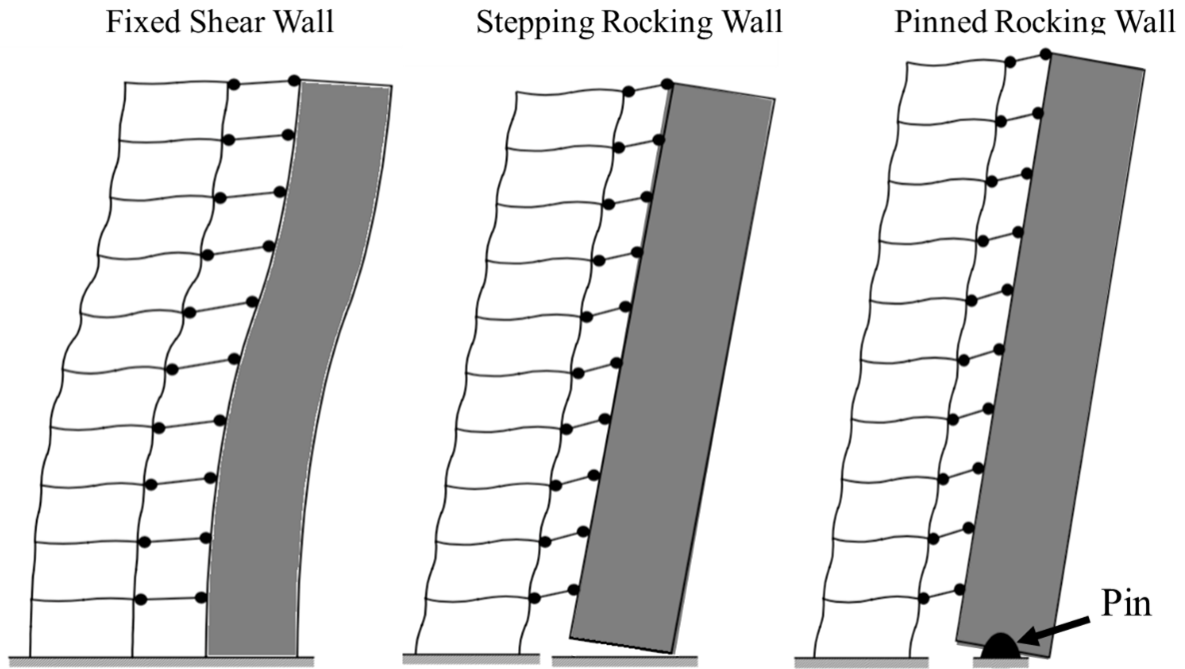


Figure 1.5: Conventional Fixed shear wall (left) compared to stepping rocking wall (center) and Pinned rocking wall (right).

Erkmen and Schultz [42] investigated self-centering behavior of postensioned precast shear walls. Experimental results in this study showed that even though the postensioning force may die-out in cyclic loading but the rocking wall is still capable of recentering.

Tozano et al. [17] tested a confined-masonry rocking wall-reinforced concrete frame system with supplemental hysteretic damping. In order to design the wall-frame system a performance-based design methodology is used. This study investigates the benefits of masonry rocking wall-reinforced concrete frame, incorporated with low-cost hysteretic damping in order to reduce maximum roof drifts and dissipate more energy. Prototype structure was a 40% scaled model of a segment of a three-story building. Structure tested under 60 different ground motions which most of them were intended to reproduce the seismic demand of the system in different design levels.

The structure showed a good performance under different levels of ground motions and met the design criteria. This study focuses mostly on the performance of the tested prototype structure, the advantage of rocking-wall frame system using ability of self-centering in the rocking wall, and with addition of low-cost hysteretic dampers how these systems can dissipate more energy. Since this study is more focused on the performance of the structure under different design levels, there is no detailed discussion on the dynamic behavior of the rocking wall and effect of walls rotational inertia. These tests showed that thanks to good performance of rocking masonry wall, this structure performed well under different seismic excitation, and reached a maximum roof drift ratio of 2.5% without visible damage. Finally, the structural system showed no residual deformation because of employing the advantage of self-centering in rocking systems.

Inspired by the idea of coupling a moment-resisting frame with a pinned-rocking wall from the work of Alavi and Krawinkler [18], Wada et al. [19] and Qu et al. [20] retrofitted an existing reinforced concrete moment-resisting frame with a pinned-rocking wall and steel damping system. The structure was a 11-story-high reinforced concrete frame building which is located in the campus of Tokyo Institute of Technology in Japan. The proposed rocking wall system is a pin-supported concrete wall which is connected to the main frame of the structure. Goal of this retrofitting is enhancing integrity and avoiding weak story failure. Although pin-support connection of the wall prevents the wall foundation impact (when the wall changes its pivot point in rocking) but wall weight cannot help in the self-centering of the system in order to prevent residual displacements. Also, it had showed that strengthening of the frame with hinged walls is effective way of reducing maximum story drift and producing more uniform distribution of story drifts. Performance of the structure assessed through nonlinear dynamic analysis before and after retrofitting. Additionally, energy dissipating devices used between rocking wall and frame. With this approach vertical deformation of the wall can be used in order to dissipate more energy Theoretical analysis of the system in this paper has done in a capacity design manner and while they considered a lateral load

at the roof level the failure mechanism is assumed. Because of the nature of this analysis, inertia of the wall is neglected which will not represent the real dynamic behavior of the system. Analytical model of the structure is analyzed under different ground motions for the cases of before and after retrofit using ABAQUS software. The hysteretic behavior of the steel dampers is idealized as elastic-perfectly plastic the nominal yielding strength. The analysis shows the structure undergoes smaller drifts, and deflections are evenly distributed through the structure which shows the damage would be distributed throughout the structure not concentrating at a local part of the structure.

Hu and Zhang [21] studied retrofitting of concrete frames using hybrid rocking walls (rocking walls with prestressing tendons and dampers). They made a parametric study of the seismic behavior of self-centering walls used for retrofitting of the reinforced concrete frames. This study examined the effect of variety of factors like cross sectional area of prestressing tendons, location of the tendons in the wall and yielding stress of the hysteretic dampers. In the numerical modeling of the system the wall modeled as beam-column element and its mass lumped at the end of nodes (without mentioning any mass inertia consideration). The rocking wall is an infill masonry wall in a reinforce concrete frame with prestressing tendons. Additionally, a prototype structure is selected for numerical analysis. Push over and time history analysis of this numerical model had done using OpenSees. The results of this paper compared frame without wall with a frame retrofitted with a rocking wall and showed that after retrofitting the frame dropped the drift from 2-5% to 0.5-0.9% for different ground motions. Additionally, this study investigated the parametric study of the tendons in the rocking wall system and found that the area of the tendons and yield strength of the base dampers play a great role in hysteretic behavior of the hybrid wall system.

Belleri et al. [43] analyzed a half scaled 3-story high precast concrete building with two unbonded post-tensioned precast walls located at the north and south of the structure, subjected to shake-table testing. In order to provide more energy dissipation ability, energy dissipating devices were used. Through these tests they evaluate the design procedure. The test reported in this paper is

the dynamic response of rocking wall to ground motions. Additionally, they investigated higher mode effects on the response of the system and strain distribution at rocking wall's pivoting points. Expected and measured responses of the wall are also presented.

Nicknam et al. [22] analyzed and compared experimental results with a numerical model of a structural system which named propped rocking wall (PRW). Proposed structure is a 1:3 scaled structure and goal of the study is to validate direct displacement-based design with experimental outcomes. PRW structure system consists of a concrete frame with a wall which has unbonded post tensioned bars and two diagonally propped hysteretic dampers connected to the wall. In the proposed design method based on a closed-form solution derived for the base shear-roof displacement relationship of the PRW system at its maximum response, even though the wall rotates around its pivoting point but in the calculation no mass inertia of the wall included. An experimental study is performed. A wall with three floors slabs connected to it, and propped hysteretic dampers is designed with this method. This structure then analyzed under different ground motions. The tests showed good seismic behavior of PRW system, but experimentally measured fundamental period of the system was significantly larger than pre-test numerical analysis. Comparison of the experimental and numerical results shows that the results are close but the numerical model's response damps out quicker than the experiment and the maximum roof displacement of the experimental model is higher than the numerical model.

Grigorian and Grigorian [23, 24] proposed a new approach based on the principles of designed analysis for the rocking-wall-moment-frame (RWMF) systems. In this study several generic examples and case studies have been provided to demonstrate application and validation of the proposed procedure. The rocking wall system of this study consists of a pin-supported wall coupled with a frame and the wall-frame system is connected with rigid pin-ended arms. In the analysis, although the wall considered to be rigid, but when the wall tilted no mass rotational inertia was considered.

Nazari et al. [44] investigated different precast rocking walls with various prestressing and tendon area configurations. In terms of performance under different seismic loadings rocking walls performed satisfactorily and sustained negligible damages. All test walls recentered with minimum residuals. In this study, prestressed precast wall is also modeled in OpenSees with a single degree idealization of the rocking wall. This analysis was in good agreement with the experimental results.

In their recent work Sun and Kurama [45] proposed a practical displacement-based seismic design for pin-supported rocking wall-frame systems. In their analytic study they investigated behavior of a frame with pin-supported wall. In this study supplemental damping devices has been used to dissipate more energy and reduce maximum deformation and they concluded that the proposed system works satisfactory under designed seismic loads. In their work they showed that the pin-supported wall when is not equipped with dampers is not recenter properly (figures 11) and they confirmed the similar findings as introduced in work of Aghagholizadeh and Makris which weight of the pinned rocking wall works against stability [46, 47]. At the same time Gioiella et al. [48] introduced "dissipative tower" solution that they retrofitted a school in Italy with two pin-supported rocking steel frames equipped with supplemental damping. In both works of Sun and Kuramma [45] and Gioiella et al. [48] they validate first-mode domination and they also use single-degree-of-freedom approach to design the system as it presented in [47, 49].

Objectives and Scope

This study is on the seismic response of yielding structures coupled with rocking walls. This topic is of major significance in the design of tall moment-resisting buildings, since during recent major earthquakes several tall, moment-resisting frames that had been designed in an accordance to the existing seismic code provisions, exhibited a weak-story failure some cases several stories above

the ground. Utilization of this structural system can help reducing maximum story drifts, prevents weak story failure and minimize residual deformation of the structure.

Some of the objectives of this study can be summarized as follows

- Comparative study on the dynamics of stepping rocking wall and pinned rocking walls
- In current practice, seismic response of a building frame coupled with a rocking wall is entrenched within the context of capacity design—that is essentially a static procedure, where the nonlinear dynamics of the rocking wall is neglected.
- Investigate that to what extent the dynamics of a rocking wall influenced the dynamic response and permanent displacements of the coupled yielding structure
- Study behavior of the rocking wall-frame system with vertical prestressing
- Effect of supplemental damping in system's maximum drift
- Verification of SDOF representation

This study offers a systematic investigation of the complex nonlinear dynamics associated with this structural configuration and it concludes to important practical design recommendations.

This dissertation first derives the nonlinear equations of motion of a yielding oscillator coupled with rocking walls and analyzes dynamics of yielding oscillator coupled with stepping rocking or pinned rocking walls. It investigates that how different configuration of the wall can effect the maximum displacement and its recentering capability. Next, effect of vertical restrainers (with or without prestressing) in stepping rocking walls is studied. Also rocking walls equipped with supplemental dampers are examined. Lastly, the dependability of the one-degree of freedom idealization is validated against the nonlinear time-history response analysis of a well-known 9-story moment-resisting steel frame.

CHAPTER 2: YIELDING STRUCTURE WITH A STEPPING AND PINNED ROCKING WALL

Introduction

Following the spectacular damage of the Olive View Hospital during the 1971 San Fernando, California earthquake, Bertero et al. [1] directed the attention of engineers to coherent acceleration pulses (0.8–1.5 s duration at that time) which result in large monotonic velocity increments and impose severe deformation demands on structures. Such coherent acceleration pulses received revived attention some 20 years later after the 1994 Northridge, California and the 1995 Kobe, Japan earthquakes when the majority of engineers recognized the severe implications of the destructive potential of pulse-like ground motions recorded near the causative fault of earthquakes [2–4]. In particular, several tall, moment-resisting frames that have been designed in accordance to the existing seismic code provisions exhibited a weak-story failure in some cases several stories above the ground [3, 50].

In an effort to eliminate the generation of a weak story failure an old concept [5] was revived that is the coupling of a moment resisting frame with a rocking wall [15, 17, 18] and it was recently implemented for the seismic upgrade of an 11-story building in Japan [19, 20]. The concept of enhancing the seismic performance of a moment resisting frame by coupling its response with a strong rocking wall has been also supported appreciably by the progress achieved in the technology of precast, post-tensioned [7, 9, 11, 12, 14] and is receiving increasing attention by practicing engineers ([23, 24] among others). In addition to preventing a weak-story failure, stepping rocking walls suppress permanent drifts; therefore, the entire structural system may reach safely a larger deformation capacity. In contrast, fixed-base shear walls may experience near their base appre-

liable cyclic degradation under long excitation motions and are subject to large ductility demands under near-fault pulse-like motions.

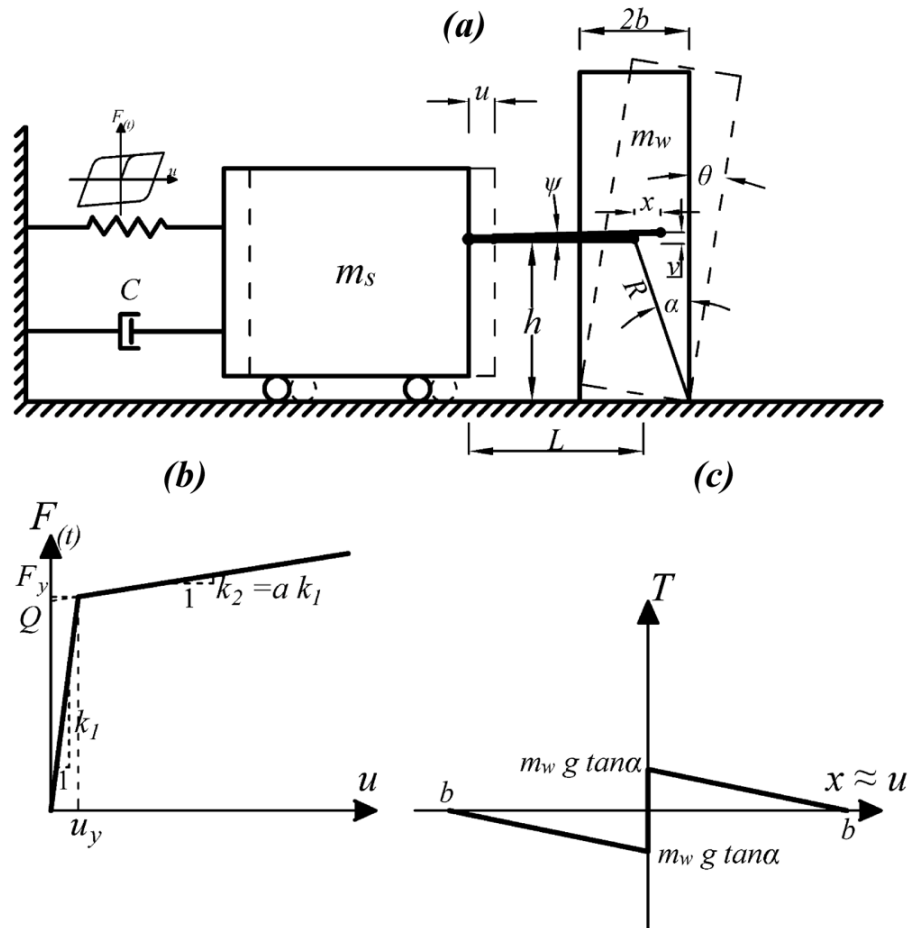


Figure 2.1: (a): Yielding single-degree-of-freedom oscillator coupled with a stepping rocking wall. While schematically the wall is shown to be connected in series with the mass, the dynamics of the wall works in parallel with the nonlinear spring and dashpot because of the rigid connection between the mass and the wall. (b): The bilinear idealization with its control parameters. (c): Force-displacement diagram of the stepping rocking wall.

When a moment-resisting frame that is coupled with a rocking wall yields, the dynamics of the system are affected by both the inelastic behavior of the moment-resisting frame and the dynamics of the rocking wall which may be either a stepping rocking wall which enhances the recentering

capability of the entire structure [5, 15–17, 21] or a pinned rocking wall [18–20].

Most of these aforementioned studies introduce the unique advantages of rocking action by referencing the seminal paper by Housner [26], who noticed that tall, slender, free-standing columns, while they can easily uplift even when subjected to a moderate ground acceleration (uplifting initiates when $\ddot{u}_g > g \frac{base}{height}$); they exhibit remarkable seismic stability due to a size-frequency scale effect. In his 1963 paper, Housner shows that there is a safety margin between uplifting and overturning and that as the size of the free-standing column increases or the frequency of the excitation pulse increases, this safety margin increases appreciably to the extent that large free-standing columns enjoy ample seismic stability. Recently, [27, 28] explained that as the size of the free-standing rocking column increases, the enhanced seismic stability primarily originates from the difficulty to mobilize the rotational inertia of the column (wall) which increases with the square of the column (wall) size. Further studies by Vassiliou and Makris [30] and Makris and Vassiliou [29] showed that as the size of the column (wall) increases, the resistance to mobilize the rotational inertia increases to such an extent, that even the effect of vertical tendons becomes increasingly marginal.

With the clear exception of the pioneering work of Meek [5], the prevailing approach in the aforementioned studies which are concerned with the seismic response of a building frame coupled with a rocking wall is entrenched within the context of capacity design that is essentially a static procedure, where the effect of the rotational inertia of the rocking wall is neglected. Clearly, there are cases where the response of the moment-resisting frame dominates the overall response and the rotational inertia effects of the rocking wall are negligible. Nevertheless, in view of the expected inelastic behavior of the moment resisting frames and the acceptance by the practice of pinned rocking walls that work against the stability of the system [46, 51], the main motivation of this study is to examine to what extent the dynamics of a stepping or a pinned rocking wall influences the dynamic response and permanent displacements of the coupled inelastic oscillator shown in

Figures 2.1 and 2.2.

The motivation for coupling of a moment-resisting frame with a strong rocking wall is to primarily enforce a uniform distribution of interstory drifts and avoid a soft story collapse; therefore, the first mode of the frame becomes dominant as was first indicated in the seminal paper by Alavi and Krawinler [18]. Further analytical evidence to the first-mode dominated response is offered in the Qu et al. [20] and Aghagholizadeh and Makris [47] papers. These results together with additional evidence by other investigators were critically evaluated in the paper by Grigorian and Grigorian [23] who concluded that a moment resisting frame coupled with a rocking wall can be categorized as a single-degree-of-freedom (SDOF) system. Accordingly, in this study the authors adopted the SDOF idealization shown in Figures 2.1 and 2.2 which is most relevant for stiff rocking walls.

Dynamics of a Yielding Oscillator Coupled with a Stepping Rocking Wall

With reference to Figure 2.1., this study first examines the dynamic response of a yielding single-degree-of-freedom (SDOF) structure, with mass, m_s , pre-yielding stiffness, k_1 , post yielding stiffness k_2 , and strength, Q , that is coupled with a free-standing stepping rocking wall of size $R = \sqrt{b^2 + h^2}$, slenderness, $\tan \alpha = b/h$, mass, m_w and moment of inertia about the pivoting (stepping) points O and O' , $I = 4/3m_w R^2$. In the interest of simplicity, the authors assume that the arm with length, L , that couples the motion is articulated at the center of mass of the rocking wall at a height, h , from its foundation as shown in Figure 2.1.

During rocking motion, the center of mass of the rocking wall uplifts by v ; therefore, the initially horizontal coupling arm rotates by an angle ψ . Accordingly, the horizontal translation of the center of mass of the rotating wall, x , is related to the horizontal displacement of the SDOF oscillator, u , via the expression, $\cos \psi = 1 - (u - x)/L$; whereas, $\sin \psi = v/L$. From the identity, $\cos^2 \psi +$

$\sin^2 \psi = 1$, one concludes that the horizontal displacement, u of the SDOF oscillator is related to the horizontal displacement x of the center of mass of the rotating wall via the expression:

$$\frac{u}{L} = 1 + \frac{x}{L} - \sqrt{1 - \frac{v^2}{L^2}} \quad (2.1)$$

For the sake of simplicity, it is assumed to be long enough so that v^2/L^2 is much smaller than unity ($v^2/L^2 \ll 1$); and in this case $u = x$. Clearly, there are cases where the coupling arm is short and in this case the term v^2/L^2 is not negligible. Nevertheless, a recent study by Makris and Aghagholizadeh [46] on the response of an elastic oscillator coupled with a rocking wall showed that the effect due to a shorter coupling arm is negligible. The importance of the length of the coupling arm is also discussed later in this chapter.

The system under consideration shown in Figure 2.1 is a single-degree-of-freedom system where the lateral translation of the mass, u is related to the rotation of the stepping rocking wall θ via the expression:

$$u = \pm R[\sin \alpha - \sin(\alpha \mp \theta)] \quad (2.2)$$

$$\dot{u} = R\dot{\theta} \cos(\alpha \mp \theta) \quad (2.3)$$

$$\ddot{u} = R[\ddot{\theta} \cos(\alpha \mp \theta) \pm \dot{\theta}^2 \sin(\alpha \mp \theta)] \quad (2.4)$$

In equations (2.2) to (2.4) whenever there is a double sign (say \pm), the top sign is for $\theta > 0$ and the bottom sign is for $\theta < 0$. Dynamic equilibrium of the mass m_s gives:

$$m_s(\ddot{u} + \ddot{u}_g) = -F_s - c\dot{u} + T \quad (2.5)$$

where F_s is the force the develops in the nonlinear spring and is described by the Bouc-Wen model [52].

$$F_s(t) = ak_1u(t) + (1 - a)k_1u_yz(t) \quad (2.6)$$

where $a = k_2/k_1$ is the postto-pre yielding stiffness ratio and $-1 \leq z(t) \leq 1$ is a dimensionless internal variable described by:

$$\dot{z}(t) = \frac{1}{u_y} [\dot{u}(t) - \beta \dot{u}(t)|z(t)|^n - \gamma |\dot{u}(t)|z(t)|^{n-1}] \quad (2.7)$$

In equation (2.7), constants β , γ and n are model parameters to be discussed later in the chapter.

Furthermore, in equation (2.5), T is the axial force (positive = tensile) that develops in the coupling arm.

Case 1 $\theta > 0$:

For positive rotations ($\theta > 0$), dynamic equilibrium of the rotating wall with mass m_w , gives:

$$I\ddot{\theta} = -TR\cos(\alpha - \theta) - m_w g R \sin(\alpha - \theta) - m_w \ddot{u}_g R \cos(\alpha - \theta) \quad (2.8)$$

The axial force T appearing in equation (2.8) is replaced with the help of equations (2.5) and (2.6) and for a rectangular stepping wall ($I = \frac{4}{3}m_w R^2$), equation (2.8) assumes the form:

$$\begin{aligned} \frac{4}{3}m_w R^2 \ddot{\theta} + [m_s(\ddot{u} + \ddot{u}_g) + ak_1u(t) + (1 - a)k_1u_yz(t) + c\dot{u}]R\cos(\alpha - \theta) \\ = -m_w R[\ddot{u}_g \cos(\alpha - \theta) + g \sin(\alpha - \theta)] \end{aligned} \quad (2.9)$$

Upon dividing with $m_w R$ equation (2.9) gives:

$$\begin{aligned} \frac{4}{3}R\ddot{\theta} + \left[\sigma(\ddot{u} + \ddot{u}_g) + a\frac{k_1}{m_w}u(t) + (1-a)\frac{k_1}{m_w}u_y z(t) + \frac{c}{m_w}\dot{u} \right] \cos(\alpha - \theta) \\ = -\ddot{u}_g \cos(\alpha - \theta) - g \sin(\alpha - \theta) \end{aligned} \quad (2.10)$$

in which $\sigma = m_s/m_w$ is the mass ratio parameter.

Substitution of the expressions of the relative displacement, velocity and acceleration given by equations (2.2) to (2.4) for positive rotations and after dividing with R , equation (2.10) gives:

$$\begin{aligned} \left(\frac{4}{3} + \sigma \cos^2(\alpha - \theta) \right) \ddot{\theta} \\ + \sigma \cos(\alpha - \theta) \left[a\omega_1^2 (\sin \alpha - \sin(\alpha - \theta)) + 2\xi \omega_1 \dot{\theta} \cos(\alpha - \theta) + \dot{\theta}^2 \sin(\alpha - \theta) \right. \\ \left. + (1-a)\omega_1^2 \frac{u_y}{R} z(t) \right] = -\frac{g}{R} \left[(\sigma + 1) \frac{\ddot{u}_g}{g} \cos(\alpha - \theta) + \sin(\alpha - \theta) \right], \end{aligned} \quad (2.11)$$

where $\omega_1 = \sqrt{k_1/m_s}$ is the pre-yielding undamped frequency and $\xi = \frac{c}{2m_s\omega_1}$ is the pre-yielding viscous damping ratio of the SDOF oscillator. Equation (2.11) is the equation of motion for positive rotations of the coupled system shown in Fig. 2.1.

Case 2: $\theta < 0$

For negative rotations one can follow the same reasoning and the equation of the coupled system shown in Fig. 2.1 is:

$$\begin{aligned} \left(\frac{4}{3} + \sigma \cos^2(\alpha + \theta) \right) \ddot{\theta} \\ - \sigma \cos(\alpha + \theta) \left[a\omega_1^2 (\sin \alpha - \sin(\alpha + \theta)) - 2\xi \omega_1 \dot{\theta} \cos(\alpha + \theta) + \dot{\theta}^2 \sin(\alpha + \theta) \right. \\ \left. - (1-a)\omega_1^2 \frac{u_y}{R} z(t) \right] = \frac{g}{R} \left[-(\sigma + 1) \frac{\ddot{u}_g}{g} \cos(\alpha + \theta) + \sin(\alpha + \theta) \right] \end{aligned} \quad (2.12)$$

When parameter $a = 1$, the expressions offered by equations (2.11) and (2.12) describe an elastic SDOF oscillator coupled with a stepping rocking wall and they collapse to the equations of motion presented by Makris and Aghagholizadeh [46]. In equations (2.11) and (2.12) the terms multiplied with the parameter $\sigma = m_s/m_w$ are associated with the dynamics of the yielding SDOF oscillator; whereas, the remaining terms are associated with the dynamics of the rocking wall. When the SDOF oscillator is absent ($\sigma = \omega_1 = \xi = 0$), equations (2.11) and (2.12) reduce to the equations of motion of the free-standing rocking wall [36, 53–55] since the frequency parameter p for rectangular walls is $p = \sqrt{3g/4R}$.

During the oscillatory motion of the coupled system shown in Figure 2.1, aside from the energy that is dissipated from the inelastic behavior of the SDOF oscillator and the idealized viscous damping, additional energy is also lost during impact when the angle of rotation reverses. At this instant it is assumed that the rotation of the rocking wall continues smoothly from points O to O' ; nevertheless, the angular velocity, $\dot{\theta}_2$, after the impact is smaller than the angular velocity, $\dot{\theta}_1$, before the impact. Given that the energy loss during impact is a function of the wall-foundation interface, the coefficient of restitution, $e = \dot{\theta}_2/\dot{\theta}_1 < 1$, is introduced as a parameter of the problem. In this study the coefficient of restitution assumes the value of $e = 0.9$. The integration of the equations of motion (2.11) and (2.12) together with equation (2.7) is performed via a state-space formulation. The state vector of the system is

$$\left\{ y(t) \right\} = \begin{Bmatrix} y_1(t) \\ y_2(t) \\ y_3(t) \end{Bmatrix} = \begin{Bmatrix} \theta(t) \\ \dot{\theta}(t) \\ z(t) \end{Bmatrix} \quad (2.13)$$

and the time derivatives of the state vector, $\{\dot{y}(t)\}$ can be expressed solely in terms of the state variables, $y_1(t)$, $y_2(t)$ and $y_3(t)$. For instance, for positive rotations ($\theta > 0$) the time derivative

vector, $\{\dot{y}(t)\}$ is given by:

$$\left\{ \dot{y} \right\} = \begin{pmatrix} y_2 \\ \frac{\sigma \cos(\alpha - y_1)}{4/3 + \sigma \cos^2(\alpha - y_1)} \left[a\omega_1^2 (\sin \alpha - \sin(\alpha - y_1)) + 2\xi \omega_1 y_2 \cos(\alpha - y_1) + y_2^2 \sin(\alpha - y_1) \right. \\ \left. + (1-a)\omega_1^2 \frac{u_y}{R} y_3 \right] - \frac{g}{R[4/3 + \sigma \cos^2(\alpha - y_1)]} \left[(\sigma + 1) \frac{\ddot{u}_g}{g} \cos(\alpha - y_1) + \sin(\alpha - y_1) \right] \\ \frac{1}{u_y} \left[R y_2 \cos(\alpha - y_1) - \beta R y_2 \cos(\alpha - y_1) |y_3|^n - \gamma R y_2 \cos(\alpha - y_1) |y_3| y_3^{n-1} \right] \end{pmatrix} \quad (2.14)$$

The numerical integration of the time-derivative state vector, $\{\dot{y}(t)\}$, is performed with standard ordinary differential equations (ODE) solvers available in MATLAB [56]. Upon the rotation, θ , and rotational velocity, $\dot{\theta}$, are computed; the relative displacement, u and velocity \dot{u} of the mass m_s are offered by equations (2.2) and (2.3). Rocking of the stepping wall initiates when the ground acceleration exceeds the threshold [46]:

$$\ddot{u}_g^{\mu p} = \frac{1}{\sigma + 1} g \tan(\alpha) \quad (2.15)$$

Dynamics of a Yielding Oscillator Coupled with a Pinned Rocking Wall

Wada et al. [19] and Que et al. [20] proposed a pinned rocking wall for the seismic protection of an 11-story building. The novelty in the Wada et al. [19], and Qu et al. [20] studies is that the rocking wall does not alternate pivot points (it is not a stepping wall) given that it is pinned at mid-width as shown in Figure 2.2.

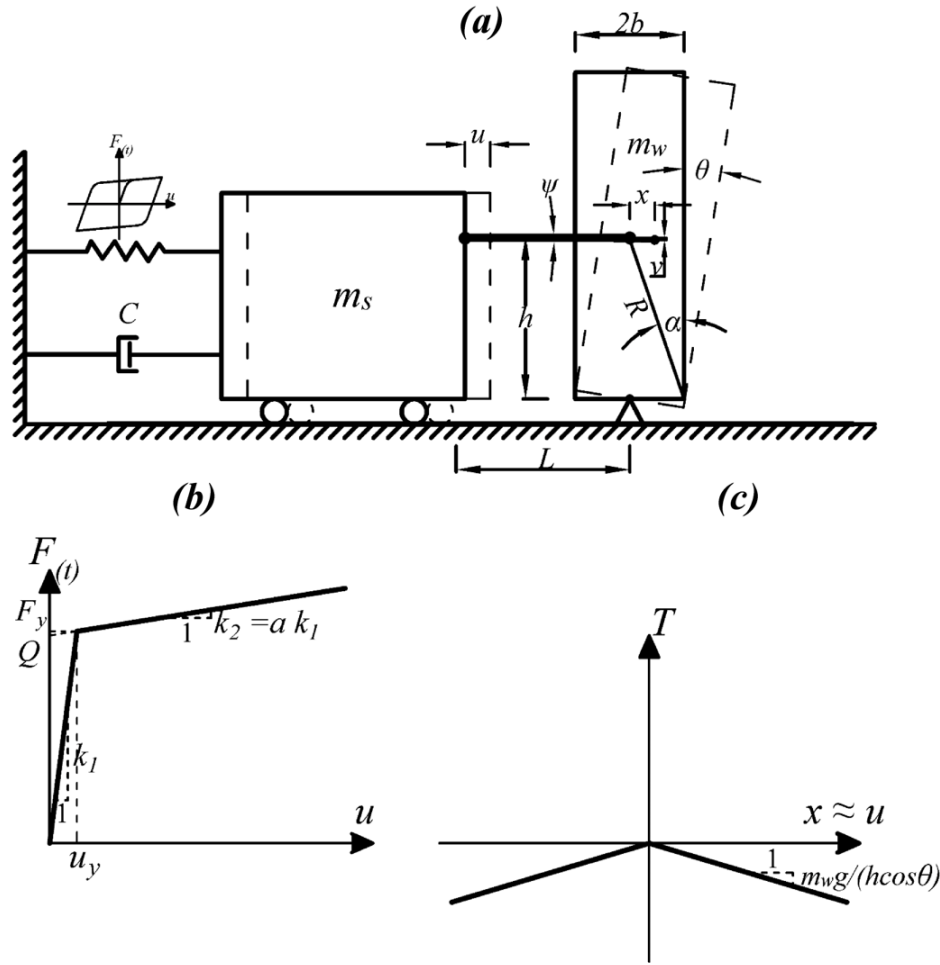


Figure 2.2: (a): Yielding single-degree-of-freedom oscillator coupled with a pinned rocking wall. While schematically the wall is shown to be connected in series with the mass, the dynamics of the wall works in parallel with the nonlinear spring and dashpot because of the rigid connection between the mass and the wall. (b): The bilinear idealization with its control parameters. (c): Force-displacement diagram of the pinned rocking wall.

A detail of the specially design pin bearing is presented in the Wada et al. [19], Qu et al. [20] studies. Given that this configuration has been adopted by other investigators (Grigorian and Grigorian [23, 24]), in this section the dynamics of a yielding SDOF structure with mass, m_s , pre-yielding stiffness, k_1 , post-yielding stiffness, k_2 , strength, Q , yielding displacement, u_y and damping c , that is coupled with pinned wall of size $R = \sqrt{b^2 + h^2}$, slenderness, $\tan \alpha = b/h$, mass, m_w and moment

of inertia about the pin O , $I = m_w R^2 (1/3 + \cos^2 \alpha)$ is examined. As in the previous case (stepping rocking wall) the authors assume that the coupling arm is articulated at the center of mass of the rocking wall at the height of $h = R \cos \alpha$ from the pin bearing as shown in Fig. 2.2; whereas, the coupling arm is assumed long enough so that $v^2 L^2 \ll 1$; and in this case, $x = u$.

The system shown in Figure 2.2 is a SDOF system where the lateral translation of the mass, u is related to the rotation of the pinned rocking wall, θ via the expression:

$$u = h \sin \theta \quad (2.16)$$

The time derivatives of equation (2.16) are:

$$\dot{u} = h \dot{\theta} \cos \theta \quad (2.17)$$

$$\ddot{u} = h \ddot{\theta} \cos \theta - h \dot{\theta}^2 \sin \theta \quad (2.18)$$

Dynamic equilibrium of the mass m_s is given by equation (2.5), where, T , is again the axial force in the coupling arm. In this case, the rocking wall does not alternate pivot points so the same equation of motion for the pinned rocking wall holds for both positive and negative rotations:

$$I \ddot{\theta} = -T h \cos \theta + m_w g h \sin \theta - m_w \ddot{u}_g h \cos \theta \quad (2.19)$$

Note that in equation (2.19) the moment from the weight of the wall ($+m_w g h \sin \theta$) works against stability; whereas the equivalent term in equation (2.8) for the stepping wall ($-m_w g R \sin(\alpha - \theta)$) works towards stability = recentering.

The axial force T appearing in equation (2.19) is replaced with the help of equation (2.5) and for

a rectangular wall pinned at the mid-span of its base ($I = m_w R^2(1/3 + \cos^2 \alpha)$), equation (2.19) assumes the form:

$$\begin{aligned} m_w R^2 \left(\frac{1}{3} + \cos^2 \alpha \right) \ddot{\theta} + \left[m_s (\ddot{u} + \ddot{u}_g) + a k_1 u + (1-a) k_1 u_y z(t) + c \dot{u} \right] h \cos \theta \\ = -m_w \ddot{u}_g h \cos \theta + m_w g h \sin \theta \end{aligned} \quad (2.20)$$

Using that $h = R \cos \alpha$, and upon dividing with $m_w R$, equation (2.20) gives:

$$\begin{aligned} R \left(\frac{1}{3} + \cos^2 \alpha \right) \ddot{\theta} + \left[\sigma (\ddot{u} + \ddot{u}_g) + a \sigma \frac{k_1}{m_s} u + (1-a) \sigma \frac{k_1}{m_s} u_y z(t) + \sigma \frac{c}{m_s} \dot{u} \right] \cos \alpha \cos \theta \\ = -\ddot{u}_g \cos \alpha \cos \theta + g \cos \alpha \sin \theta \end{aligned} \quad (2.21)$$

in which $\sigma = m_s/m_w$ as in the case of the stepping wall.

Substitution of the expression of the relative displacement, velocity and acceleration given by equations (2.16) to (2.18) and after dividing with R , equation (2.21) gives:

$$\begin{aligned} \left[\frac{1}{3} + (1 + \sigma \cos^2 \theta) \cos^2 \alpha \right] \ddot{\theta} \\ + \sigma \cos^2 \alpha \cos \theta \left[(a \omega_1^2 - \dot{\theta}^2) \sin \theta + (1-a) \omega_1^2 \frac{u_y}{R \cos \alpha} z(t) + 2\xi \omega_1 \dot{\theta} \cos \theta \right] \\ = -\frac{g}{R} \cos \alpha \left[(\sigma + 1) \frac{\ddot{u}_g}{g} \cos \theta - \sin \theta \right], \end{aligned} \quad (2.22)$$

where $\omega_1 = \sqrt{k_1/m_s}$ is the pre-yielding undamped frequency and $\xi = \frac{c}{2m_s \omega_1}$ is the viscous damping ratio of the SDOF oscillator (as in the previous case). Equation (2.22) is the equation of motion for both positive and negative rotations of the coupled system shown in Figure 2.2. Again, the state variables of the system are given by equation (2.13) and the solution is performed with standard ODE solver as described in the case of the stepping wall.

Parameters of the Problem

The Bouc-Wen model described by equations (2.6) and (2.7) is a phenomenological model of hysteresis originally proposed by Bouc [57] and subsequently generalized by Wen [52, 58] and Baber and Wen [59]. It is a versatile model that can capture various details of the nonlinear force-displacement loop. Subsequent studies on the modeling of yielding systems by Constantinou and Adnane [60] concluded that when certain constraints are imposed on the parameters β and γ ($\beta + \gamma = 1$), the model reduces to a viscoplastic element with well-defined physical characteristics. The Bouc-Wen model essentially builds on the bilinear idealization shown in the bottom-left of Figures 2.1 and 2.2. For the five-parameter system shown with the bilinear idealization. (k_1 = pre-yielding stiffness, k_2 = post-yielding stiffness, u_y = yield displacement, Q = strength and F_y = yielding force), only three parameters are needed to fully describe the bilinear behavior (see for instance [61]). In this work, the authors select the pre-yielding stiffness $k_1 = m_s \omega_1^2$, the post-yielding stiffness $k_2 = a k_1$ and the strength of the structure Q . With reference to Figures 2.1 or 2.2 (bottom-left), $F_y = k_1 u_y = Q + k_2 u_y$. Accordingly, $u_y = Q/(k_1 - k_2)$ and $F_y = k_1 Q/(k_1 - k_2)$. The parameters β , γ and n appearing in equation (2.7) are established from past studies on the parameter identification of yielding concrete structures and assume the values: $\beta = 0.95$, $\gamma = 0.05$ and $n = 2$ ([62, 63] among others). With the parameters $\beta = 0.95$, $\gamma = 0.05$ and $n = 2$ being established, the peak inelastic displacement, u_{max} of the SDOF system shown in Figures 2.1 and 2.2 is a function of the following parameters:

$$u_{max} = f\left(\omega_1, \frac{Q}{m_s}, a, \xi, p, \tan \alpha, \sigma, g, \text{parameters of excitation}\right) \quad (2.23)$$

In this study, it is assumed that upon yielding, the structure maintains a mild, positive, post-yielding stiffness $= k_2 = 0.05 k_1$, therefore $a = 0.05$ [62, 63]. Furthermore, it is assumed that the pre-yielding damping ratio, $\xi = c/(2m_s \omega_1) = 0.03$ and the authors focus on rocking walls with slenderness,

$\tan \alpha = 1/6$. Before proceeding with earthquake response spectra, Figure 2.3 plots force displacement loops, together with displacement, $u(t)$ and rotation, $\theta(t)$, time histories with a structure having, $T_1 = 0.8s$, $Q/m_s = 0.15g$ which is coupled with a rocking wall with $\omega_1/p = 10$, ($p = 0.778 \text{ rad/sec}$) and $\sigma = m_s/m_w = 10$ when excited by the Pacoima Dam/164 ground motion recorded during the 1971 San Fernando, California earthquake. The heavy line is when the structure is coupled with the wall, whereas the thin line is when there is no wall ($\sigma = \infty$).

Assuming the bilinear idealization shown at the bottom-left of Figs. 1 and 2, for a given value of pre-yielding period, T_1 , normalized strength, $Q/m_s g$ and pre-to-post yielding stiffness ratio, $a = 0.05$, the yield displacement is uniquely defined.

$$u_y = \frac{Q}{k_1(1-a)} = \frac{Q}{m_s} \frac{T_1^2}{4\pi^2(1-a)} \quad (2.24)$$

Figure 2.3 (left) indicates that the participation of the stepping rocking wall (even with appreciable size and weight, $p = 0.778 \text{ rad/sec}$, $\sigma = 10$) has a marginal effect in the suppressing peak inelastic displacement and the only clear benefit is in reducing permanent displacements.

Figure 2.3 (right) plots the corresponding response qualities described in Figure 2.3 (left) for the case where the yielding structure is coupled with a pinned rocking wall. While, Figure 2.3 (left) indicates that the stepping rocking wall slightly suppresses the peak response; Figure 2.3 (right) indicates that the pinned rocking wall slightly amplifies the peak response of the structure. In this case, the pinned rocking wall is also responsible for further increasing the permanent displacements of the inelastic structure, nevertheless, this finding is not uniform along the entire period spectrum of the frame-structures. Figures 2.4 and 2.5 reveal similar trends than those discussed for the results of Figure 2.3 when the inelastic structural system is subjected to the Takarazuka/000 ground motion recorded during the 1995 Kobe, Japan earthquake (Figure 2.4) and to the Erzincan NS ground motion recorded during the 1992 Erzincan, Turkey earthquake (Figure 2.5).

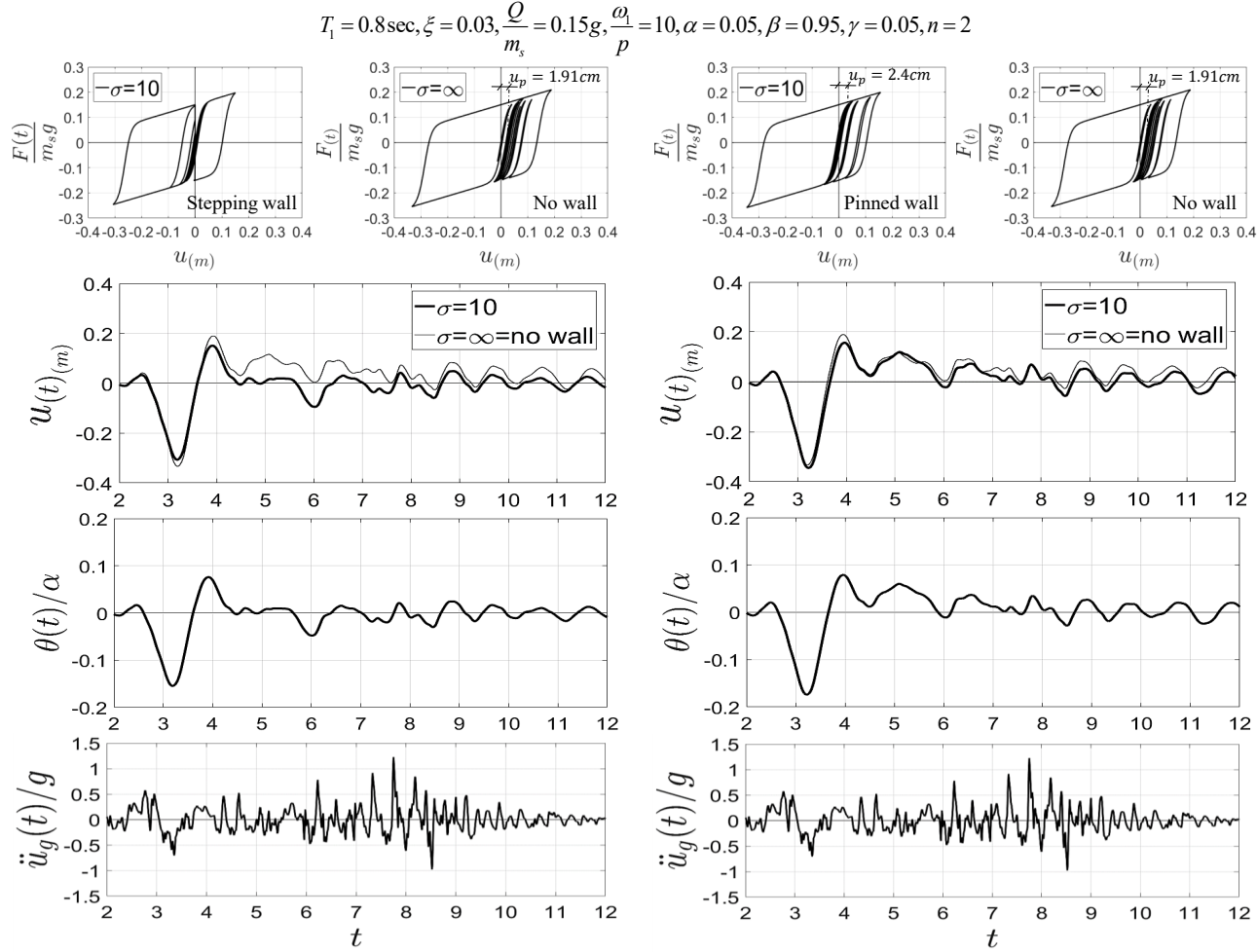


Figure 2.3: (a) Time-history analysis of a nonlinear SDOF oscillator coupled with a stepping rocking wall with normalized strength $Q/m_s = 0.15g$, mass ratio $\sigma = m_s/m_w = 10$, wall size $\omega_1/p = 10$; and preyielding period of $T_1 = 0.8s$ when subjected to the Pacoima Dam/164 ground motion recorded during the 1971 San Fernando, California earthquake. (b) Time-history analysis of a nonlinear SDOF oscillator with a pinned rocking wall with same parameters and excitation as in (a).

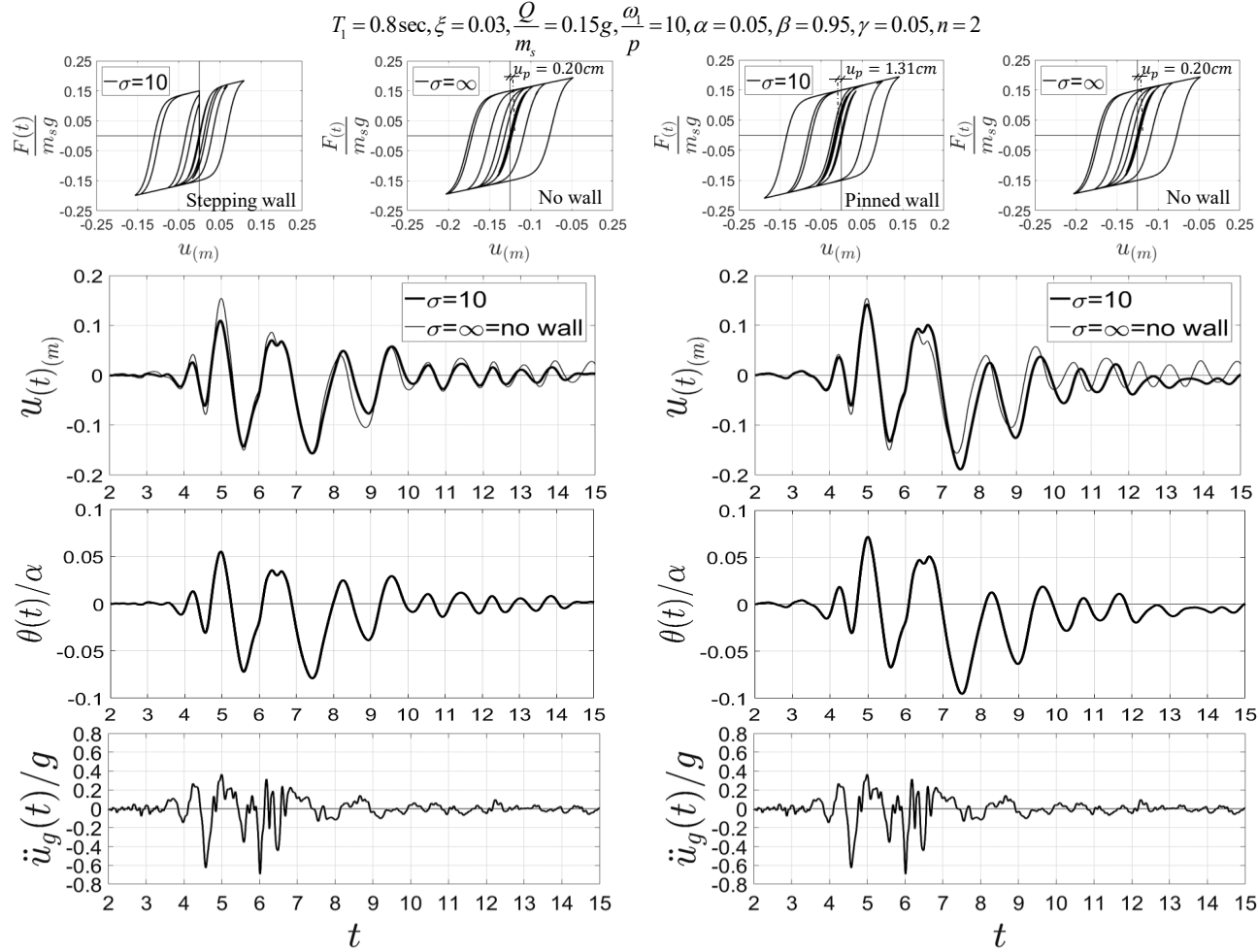


Figure 2.4: (a) Time-history analysis of a nonlinear SDOF oscillator coupled with a stepping rocking wall with normalized strength $Q/m_s = 0.15g$, mass ratio $\sigma = m_s/m_w = 10$, wall size $\omega_1/p = 10$; and preyielding period of $T_1 = 0.8s$ when subjected to the Takarazuka/000 ground motion recorded during the 1995 Kobe, Japan earthquake. (b) Time-history analysis of a nonlinear SDOF oscillator with a pinned rocking wall with same parameters and excitation as in (a).

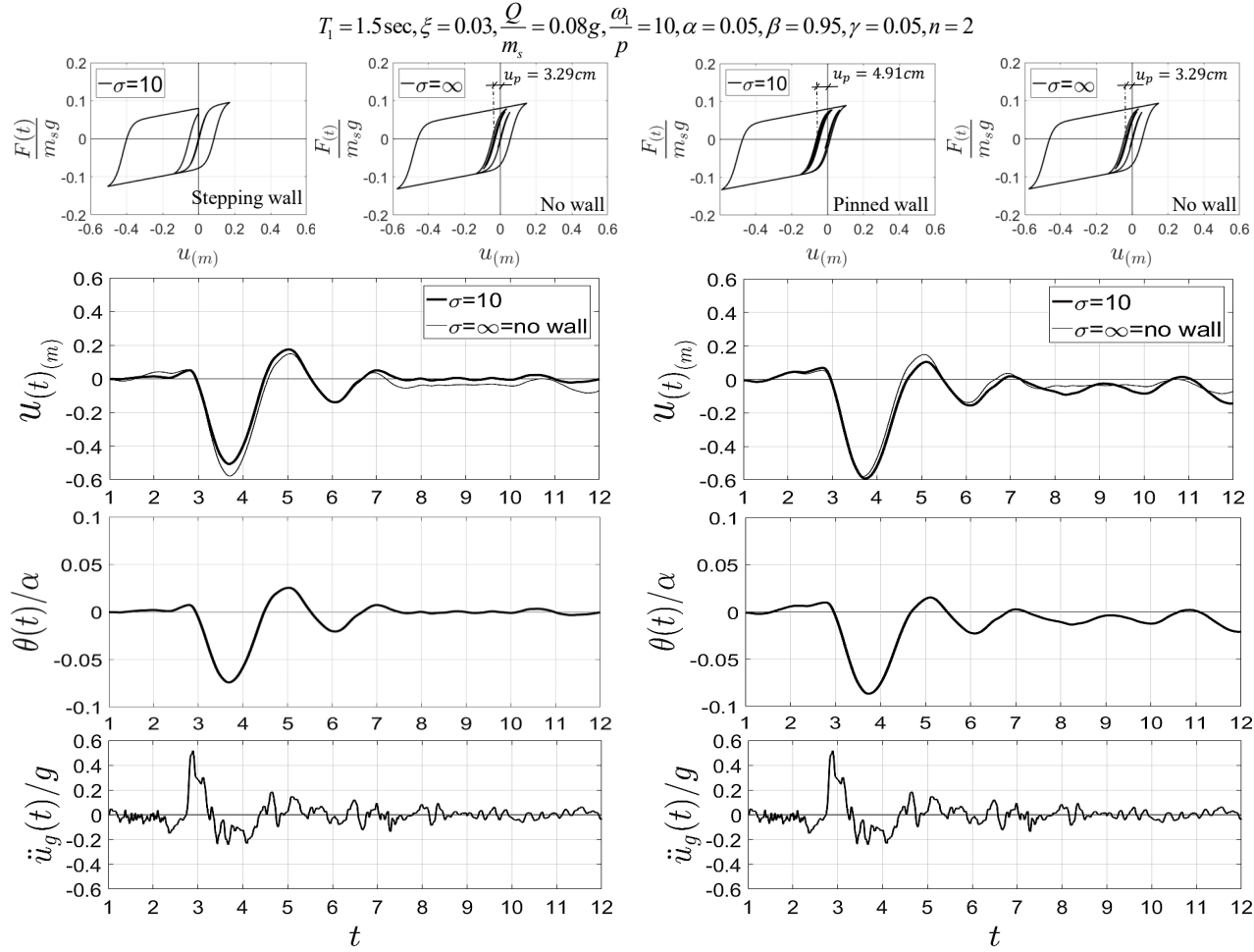


Figure 2.5: (a) Time-history analysis of a nonlinear SDOF oscillator coupled with a stepping rocking wall with normalized strength $Q/m_s = 0.08g$, mass ratio $\sigma = m_s/m_w = 10$, wall size $\omega_1/p = 10$; and preyielding period of $T_1 = 1.5s$ when subjected to the Erzincan NS ground motion recorded during the 1992 Erzincan, Turkey earthquake. (b) Time-history analysis of a nonlinear SDOF oscillator with a pinned rocking wall with same parameters and excitation as in (a).

Validation of the SDOF-Idealization

In view of small differences between the peak response of a yielding structure coupled with a rocking wall (either stepping or pinned) and the nonlinear response of the solitary yielding structure (other than the reduction of permanent displacements) even for the strong excitations shown in Figures 2.3, 2.4 and 2.5, the dependability of the single-degree-of-freedom idealization shown in Figure 2.1 and 2.2 is examined against the results obtained with the open-source code [64] when analyzing the two-bay, four-story frame shown in Figures 2.6 and 2.7 (top-left: (a)). Given that in the SDOF-models shown in Figures 2.1 and 2.2, the coupling arm is connected at the center of mass off the rocking wall, in Figures 2.6 and 2.7 (top-left: (a)), the coupling arms emanating from each story are connected along the center line of the rocking wall.

For the stepping rocking wall shown in Figure 2.6, the mechanical properties of the rocking interface are approximated with a rigid-elastic rotational spring together with a rotational viscous dashpot [65, 66] to approximate the energy loss during impact as the rocking wall alternate pivot-points. For a free-standing stepping rocking wall with size R , slenderness, α , and mass m_w , dimensional analysis yields that the expression of the equivalent rotational dashpot is [65–67]:

$$c = \lambda \alpha^2 m_w g^{0.5} R^{1.5} \quad (2.25)$$

Where $\lambda = 110$, is a parameter that is calibrated from best fit of the results. The frame is modeled with elastic elements and plastic hinges are defined with Bouc-Wen model at the beams end and base of the columns as it shown in figures 2.6(a) and 2.7(a).

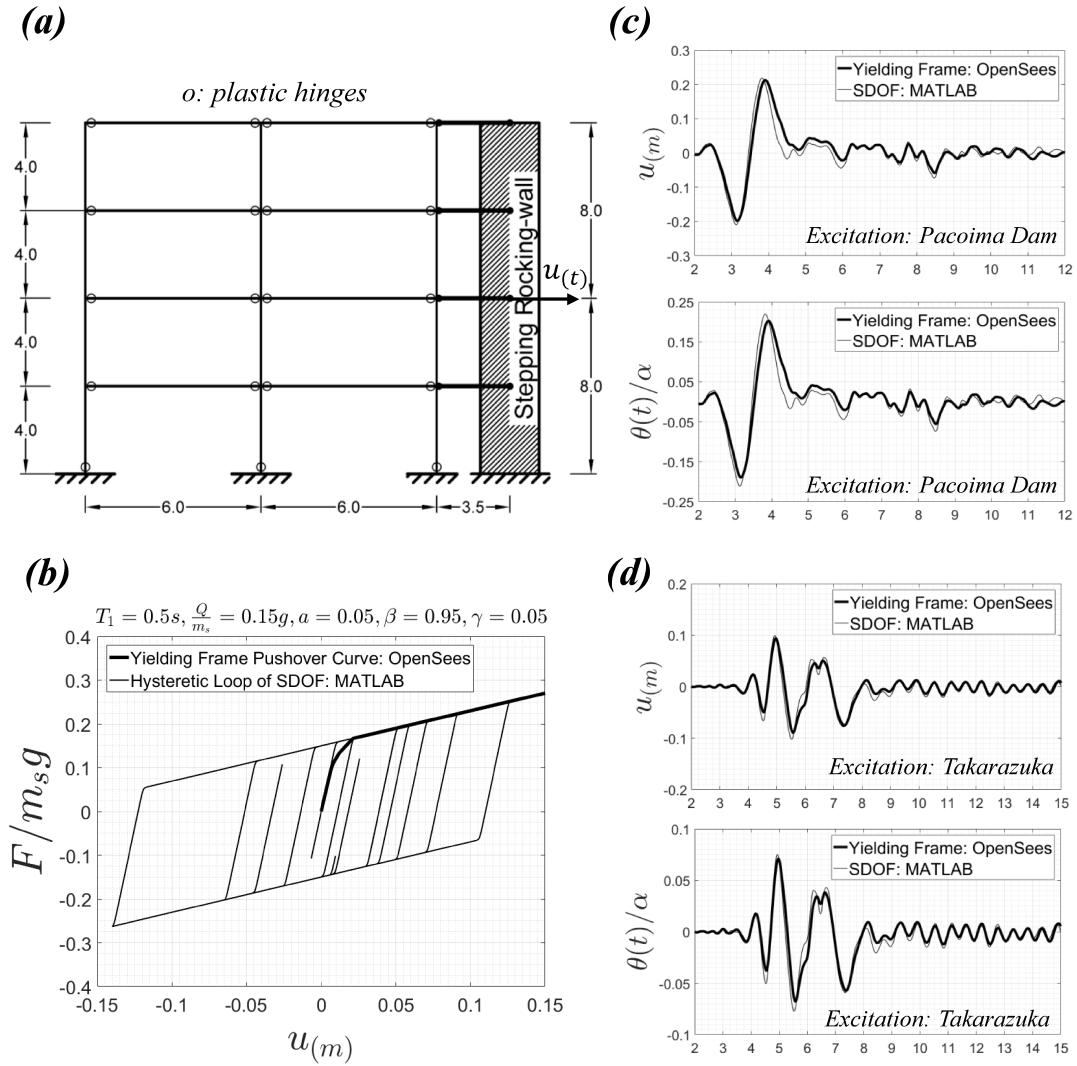


Figure 2.6: (a): Four-story, two-bay yielding frame, with pre-yielding period $T_1 = 0.5\text{sec}$ coupled with a stepping rocking wall with $p = 0.952\text{ rad/sec}$, $\omega_1/p = 13.2$ and $\sigma = m_s/m_w = 5$, (b): pushover curve for frame compared to hysteretic loop of SDOF idealization, response comparison when subjected to the 1971 Pacoima Dam/164 ground motion (c) and the 1995 Takarazuka/000 ground motion (d). Heavy solid lines: OpenSees solution; thin lines: MATLAB solution of the SDOF response.

Figure 2.6 ,(right: (c), (d)) plots response time histories of the second story displacement of a four-story yielding frame with elastic period, $T_1 = 0.5\text{ s}$ and first modal damping ratio $\xi = 0.03$, when coupled with a stepping rocking wall with $p = 0.952\text{ rad/sec}$, ($\omega_1/p = 13.2$) shown in Figure 2.6

(top-left: (a)) when subjected to the 1971 Pacoima Dam/164 ground motion shown at the bottom of Fig. 3 and the 1995 Takarazuka/000 ground motion shown at the bottom of Figure 2.4.

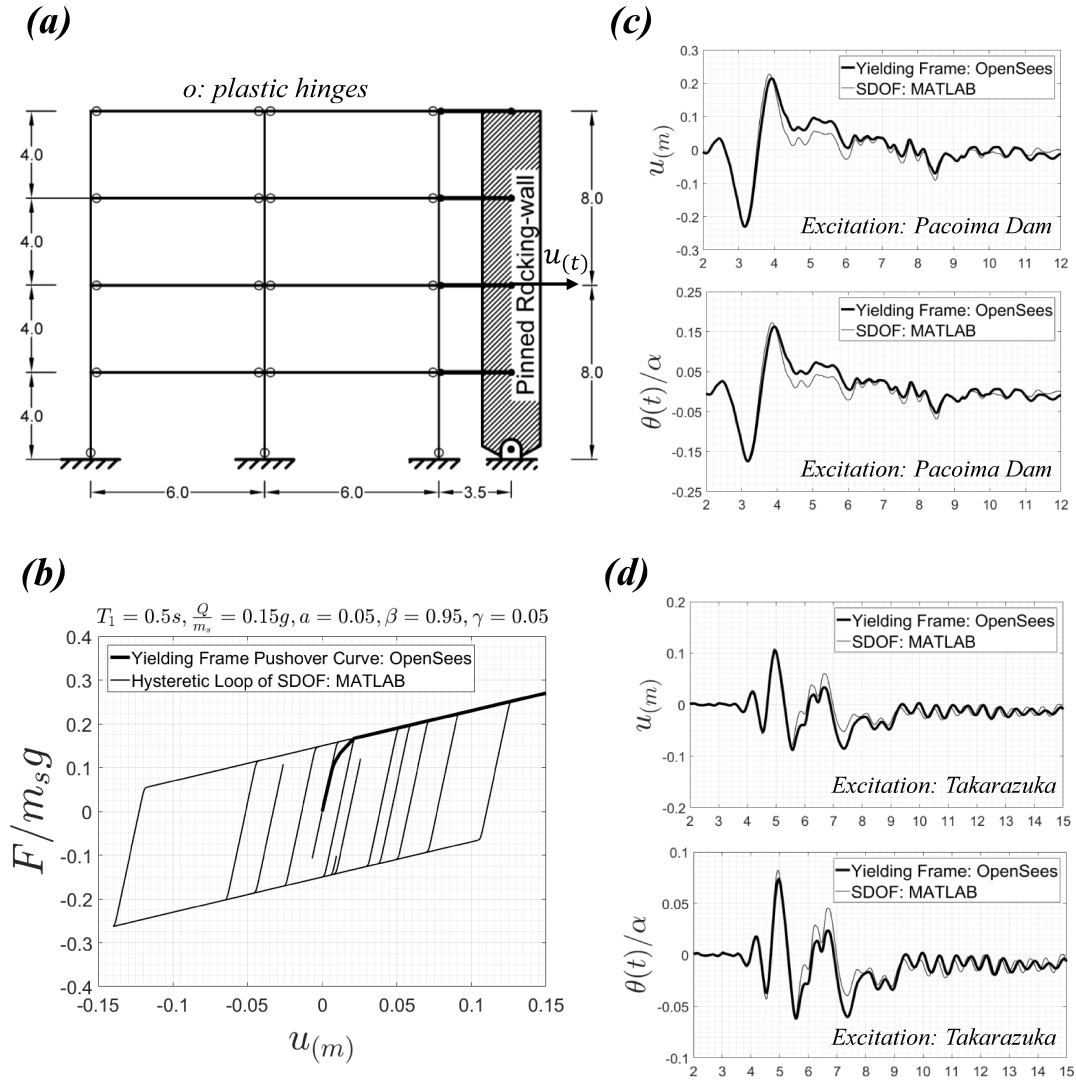


Figure 2.7: (a): Four-story, two-bay yielding frame, with pre-yielding period $T_1 = 0.5sec$ coupled with a pinned rocking wall with $p = 0.952 rad/sec$, $\omega_1/p = 13.2$ and $\sigma = m_s/m_w = 5$, (b): pushover curve for frame compared to hysteretic loop of SDOF idealization, response comparison when subjected to the 1971 Pacoima Dam/164 ground motion (c) and the 1995 Takarazuka/000 ground motion (d). Heavy solid lines: OpenSees solution; thin lines: MATLAB solution of the SDOF response.

The response of the nonlinear SDOF idealization shown in Figure 2.1 is in good agreement with the

numerical solution from OpenSees for the four-story yielding frame. This favorable comparison validates the SDOF idealization adopted in this study. For any given yielding frame, the parameters of the SDOF model, $k_1 = 4\pi^2 m_s / T_1^2$, Q/m_s and $a = k_1/k_2$ need to be calibrated to match the push-over curve of the yielding frame as is shown in Figure 2.6 (bottom-left: (b)).

Figure 2.7, (right: (c), (d)) plots response time histories of the second story displacement of a four-story yielding frame with elastic period, $T_1 = 0.5$ s and first modal damping ratio $\xi = 0.03$, when coupled with a pinned rocking wall with $p = 0.952$ rad/sec, ($\omega_1/p = 13.2$) shown in Figure 2.7 (top-left: (a)) when subjected to the 1971 Pacoima Dam/164 ground motion shown at the bottom of Figure 2.3 and the 1995 Takarazuka/000 ground motion shown at the bottom of Figure 2.4.

The response of the nonlinear SDOF idealization shown in Figure 2.2 is in good agreement with the numerical solution from OpenSees for the four-story yielding frame. This favorable comparison validates the SDOF idealization adopted in this study. For any given yielding frame, the parameters of the SDOF model, $k_1 = 4\pi^2 m_s / T_1^2$, Q/m_s and $a = k_1/k_2$ need to be calibrated to match the push-over curve of the yielding frame as is shown in Figure 2.7 (bottom-left: (b)).

Earthquake spectra of a yielding oscillator coupled with a rocking wall

Following the validation of the single-degree-of-freedom idealization adopted in this study; the equations of motion (2.11) and (2.12) for a structure coupled with a stepping wall, together with equation (2.22) for a structure coupled with a pinned wall are used to generate inelastic earthquake response spectra.

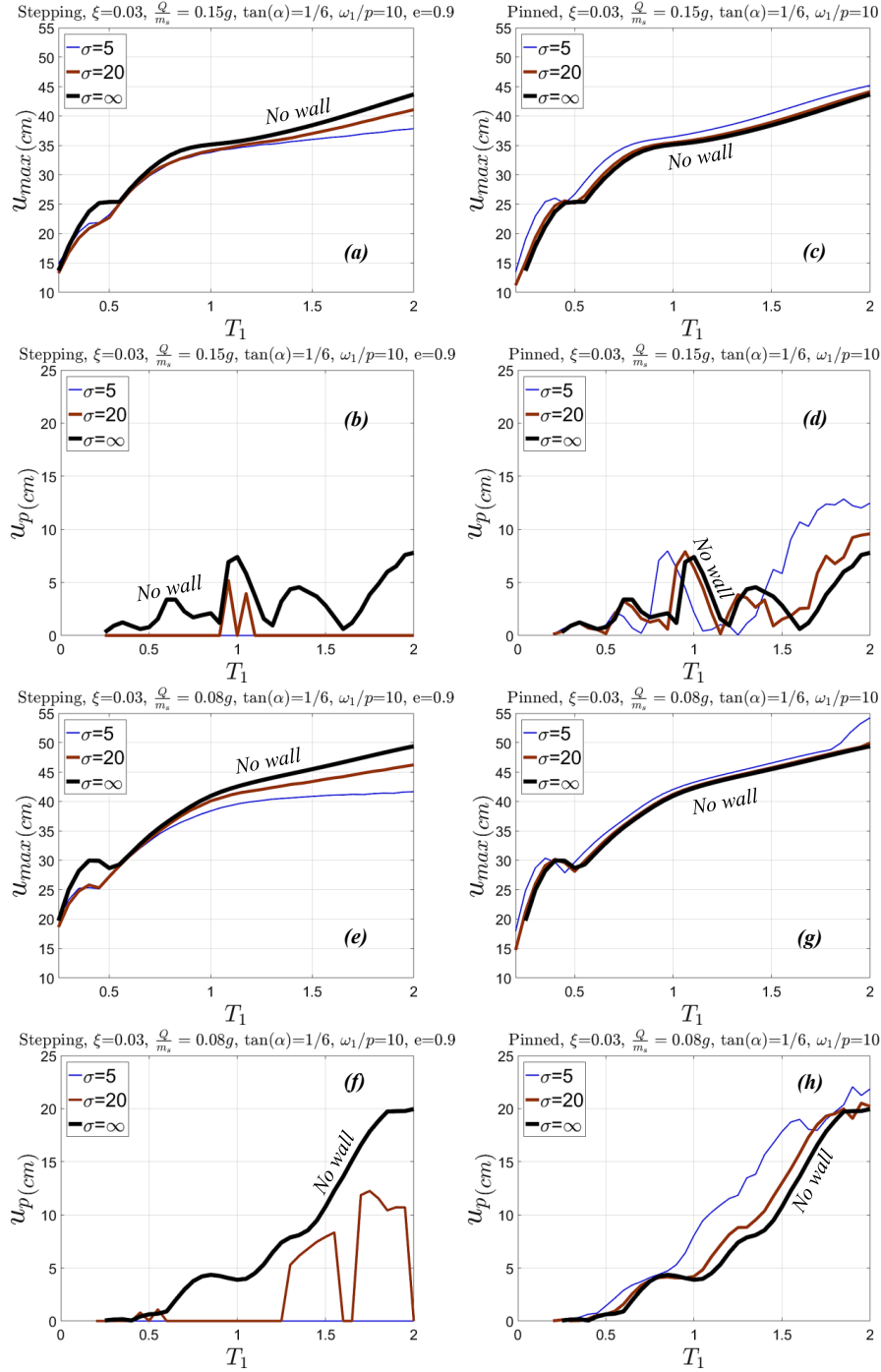


Figure 2.8: Peak displacement (a, c, e, g) and residual displacement (b, d, f, h) spectra of a yielding SDOF oscillator coupled with a stepping wall (a, b, e, f) and pinned wall (c, d, g, h) for two values of the strength, $Q/m_s = 0.15g$ (a, b, c, d) and $Q/m_s = 0.08g$ (e, f, g, h) with, mass ratio, $\sigma = m_s/m_w = 5$ and 20 and wall size, $\omega_1/p = 10$, when subjected to the Pacoima Dam/164 ground motion recorded during the 1971 San Fernando, California earthquake.

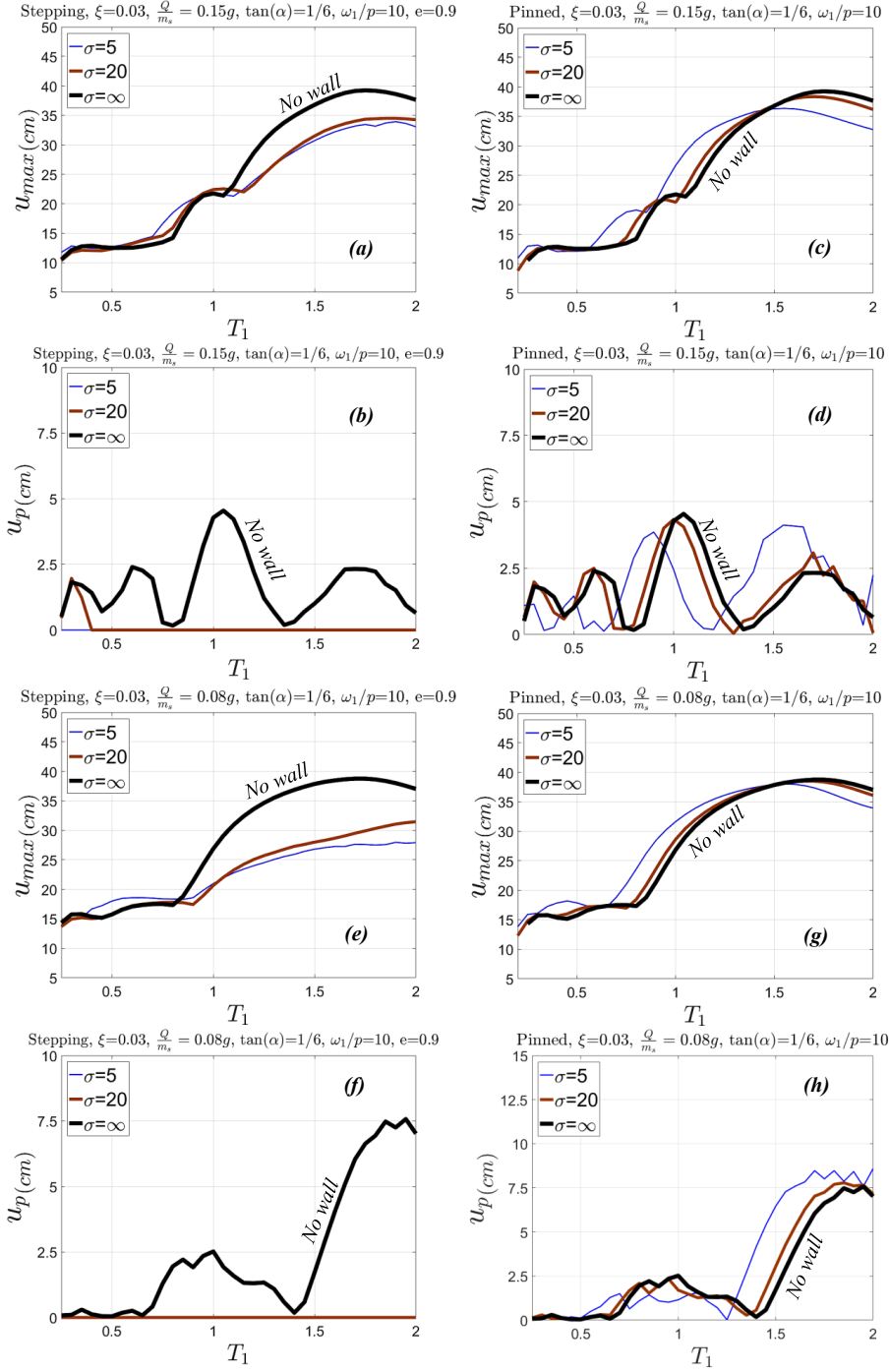


Figure 2.9: Peak displacement (a, c, e, g) and residual displacement (b, d, f, h) spectra of a yielding SDOF oscillator coupled with a stepping wall (a, b, e, f) and pinned wall (c, d, g, h) for two values of the strength, $Q/m_s = 0.15g$ (a, b, c, d) and $Q/m_s = 0.08g$ (e, f, g, h) with, mass ratio, $\sigma = m_s/m_w = 5$ and 20 and wall size, $\omega_1/p = 10$, when subjected to the Takarazuka/000 ground motion recorded during the 1995 Kobe, Japan earthquake.

Figure 2.8 plots displacement spectra for the SDOF yielding oscillator coupled with a stepping wall (left) and a pinned wall (right) when excited by the Pacoima Dam/164 ground motion recorded during the 1971 San Fernando, California earthquake. The top plots are for $Q/m_s = 0.15g$; whereas, the bottom plots are for a less strong structure with $Q/m_s = 0.08g$. The first observation is that the coupling of a yielding frame with a rocking wall has a limited effect on the peak inelastic deformation. A stepping rocking wall (left, plots in Figure 2.8) reduces the peak inelastic deformations with the heavier wall ($\sigma = 5$) being more effective; whereas, a pinned rocking wall amplifies the inelastic deformations which are accentuated with a heavier wall ($\sigma = 5$). Stepping rocking walls are effective in reducing or even eliminating permanent displacements (see plots (b) and (f)). When a heavy stepping wall is used permanent displacements are totally eliminated. In contrast, when a pinned rocking wall is used permanent displacements are in generally larger, with the heavier wall being most detrimental in particular for long-period structures (see plots (d) and (h)).

Figure 2.9 reveals the same trends than those discussed for the spectra appearing in Figure 2.8 when the yielding SDOF oscillator with the same parameters as those shown in Figure 2.8 is subjected to the *Takarazuka/000* ground motion recorded during 1995 Kobe, Japan earthquake.

Special Case: Elastic Oscillator Coupled with a Rocking Wall

When parameter $a = 1$, the expressions offered by equations (2.11) and (2.12) describe an elastic SDOF oscillator coupled with a stepping rocking wall and they collapse to the equations of motion elastic oscillator coupled with a stepping rocking wall [46]. Equation of motion in this case is

$$[4/3 + \sigma \cos^2(\alpha - \theta)]\ddot{\theta} + \sigma \cos(\alpha - \theta) [\omega_o^2 (\sin \alpha - \sin(\alpha - \theta)) + 2\xi \omega_o \dot{\theta} \cos(\alpha - \theta) + \dot{\theta}^2 \sin(\alpha - \theta)] = -\frac{g}{R} [(\sigma + 1) \frac{\ddot{u}_g}{g} \cos(\alpha - \theta) + \sin(\alpha - \theta)], \quad (\theta > 0) \quad (2.26)$$

and

$$[4/3 + \sigma \cos^2(\alpha + \theta)]\ddot{\theta} - \sigma \cos(\alpha + \theta) [\omega_o^2 (\sin \alpha - \sin(\alpha + \theta)) - 2\xi \omega_o \dot{\theta} \cos(\alpha + \theta) + \dot{\theta}^2 \sin(\alpha + \theta)] = \frac{g}{R} [-(\gamma + 1) \frac{\ddot{u}_g}{g} \cos(\alpha + \theta) + \sin(\alpha + \theta)], \quad (\theta < 0) \quad (2.27)$$

in which, $\omega_o = \sqrt{k/m_s}$ = the undamped frequency of the SDOF oscillator. The expressions offered by equations 2.26 and 2.27 have been also confirmed by the authors with a variational formulation. In equations 2.26 and 2.27 the terms multiplied with the parameter $\sigma = m_s/m_w$ are associated with the dynamics of the elastic SDOF oscillator whereas the remaining terms are associated with the dynamics of the rocking wall. When the SDOF oscillator is absent ($\sigma = \omega_o = \xi = 0$), equations 2.26 and 2.27 reduce to the equations of motion of the free-standing rocking wall [34, 36, 55] since the frequency parameter p for rectangular walls is $p = \sqrt{3g/4R}$.

Also, when pinned rocking wall is coupled with an elastic oscillator the equation of motion for the system becomes

$$[1/3 + (1 + \sigma \cos^2 \theta) \cos^2 \alpha] \ddot{\theta} - \sigma \cos^2 \alpha \cos \theta [(\omega_o^2 - \dot{\theta}^2) \sin \theta + 2\xi \omega_o \dot{\theta} \cos \theta] = -\frac{g}{R} \cos \alpha [-(\sigma + 1) \frac{\ddot{u}_g}{g} \cos \theta - \sin \theta] \quad (2.28)$$

Response Spectra of an Elastic Oscillator Coupled with a Rocking-Wall

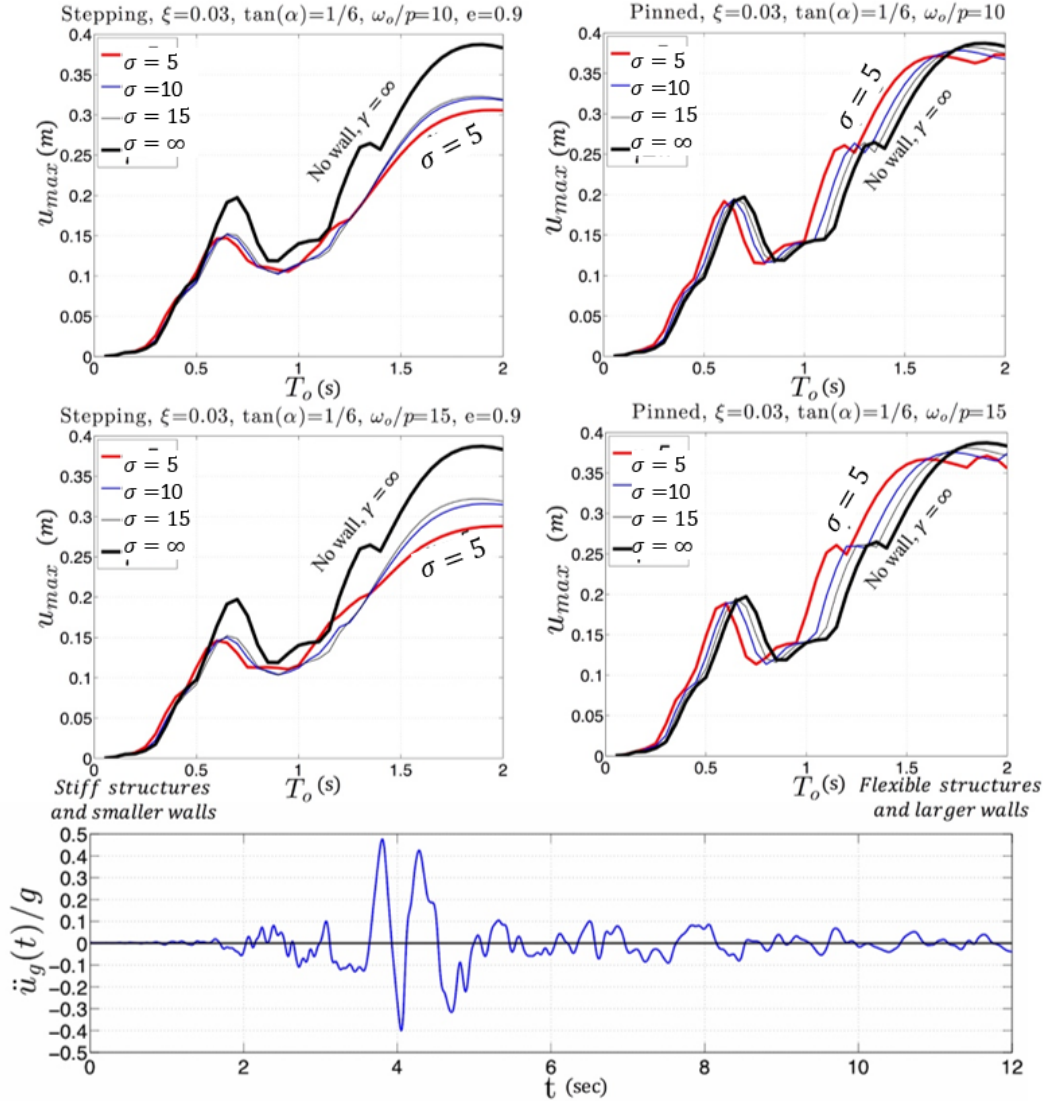


Figure 2.10: Displacement spectra of an elastic SDOF oscillator coupled with a stepping wall (left) and a pinned wall (right) for three values of the mass ratio $\sigma = m_s/m_w = 5, 10$ and 20 and two values of the wall size, $\omega_o/p = 10$ and 15 when subjected to the CO2/065 ground motion recorded during the 1966 Parkfield, California earthquake (bottom).

The equations of motions 2.26 and 2.27 for a stepping wall and 2.28 for a pinned wall are used to generate earthquake response spectra.

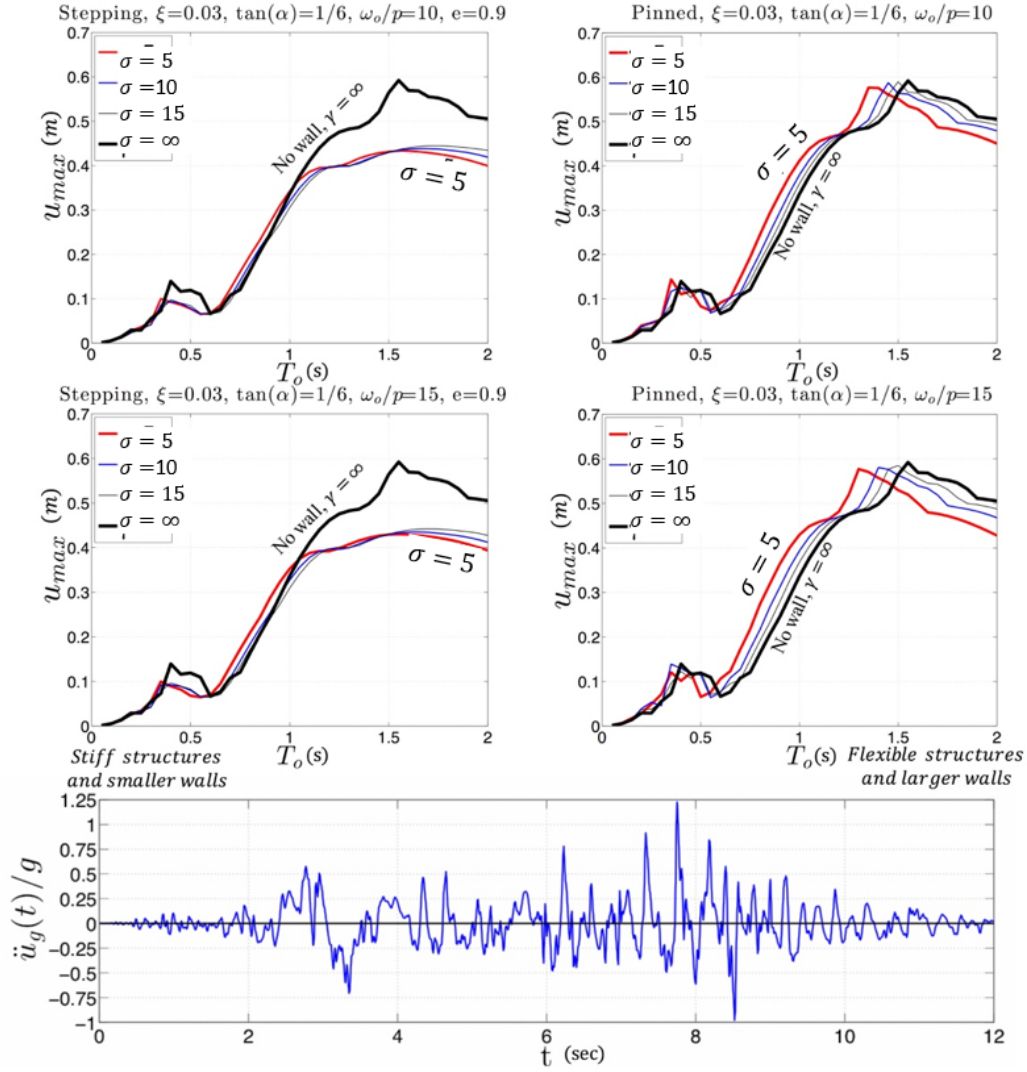


Figure 2.11: Displacement spectra of an elastic SDOF oscillator coupled with a stepping wall (left) and a pinned wall (right) for three values of the mass ratio $\sigma = m_s/m_w = 5, 10$ and 20 and two values of the wall size, $\omega_o/p = 10$ and 15 when subjected to the Pacoima Dam/164 ground motion recorded during the 1971 San Fernando, California earthquake (bottom).

Figure 2.10 plots displacement spectra for the SDOF oscillator coupled with a stepping wall (left) and a pinned wall (right) when excited by the CO2/065 ground motion recorded during the 1966 Parkfield, California earthquake shown in the bottom of Figure 2.10. The top plots are for $\omega_o/p = 10$; whereas the bottom plots are for $\omega_o/p = 15$ —that is for a larger wall at any given structural

frequency, $\omega_o = 2\pi/T_o$.

When reading the earthquake spectra shown in Figures 2.10, 2.11 and 2.12 the reader needs to recognize that as the period, T_o of the SDOF oscillator increases, for a given ratio of ω_o/p , the size of the coupled wall also increases. For instance, for the top plots which are for $\omega_o/p = 10$, the frequency parameter, p , of the wall that is coupled to a structure with $T_o = 0.5$ sec is $p = \omega_o/10 = 2/0.5 = 4$ rad/sec, which corresponds to a value of $R = 3g/4p^2 = 4.66$ m; therefore, the wall with slenderness, $\tan \alpha = 1/6$, is 9.20 m tall.

When a structure with $T_o = 1.0$ sec is of interest, the frequency parameter, p , of the wall is $p = \omega_o/10 = 2\pi/10 = 0.628$ rad/sec, which corresponds to a value of $R = 3g/4p^2 = 18.6$ m; therefore the wall with a slenderness, $\tan \alpha = 1/6$, is 36.80 m tall. When observing Figure 3, what is worth noting is that in the case where the SDOF oscillator is coupled with a stepping wall (left plots), the presence of the stepping wall suppresses the displacement response (with the heavier wall, $\sigma = 5$ being most effective), in particular for flexible structures (large values of T_o). In contrast in the case where the SDOF oscillator is coupled with a pinned wall (right plots), the presence of the pinned wall amplifies the response for the most of the spectrum with the heavier wall ($\sigma = 5$) being most detrimental. This mainly happens because in the case of the pinned wall, the moment from its weight $= +m_w g h \sin \theta$ works against stability as shown in equation 2.28.

Similar trends are shown in Figures 2.11 and 2.12 which show displacement spectra when the coupled elastic SDOF oscillator-rocking wall system is subjected to the Pacoima Dam/164 ground motion recorded during the 1971 San Fernando, California earthquake 2.11 and to the Takarazuka/000 ground motion recorded during the 1995 Kobe, Japan earthquake 2.12.

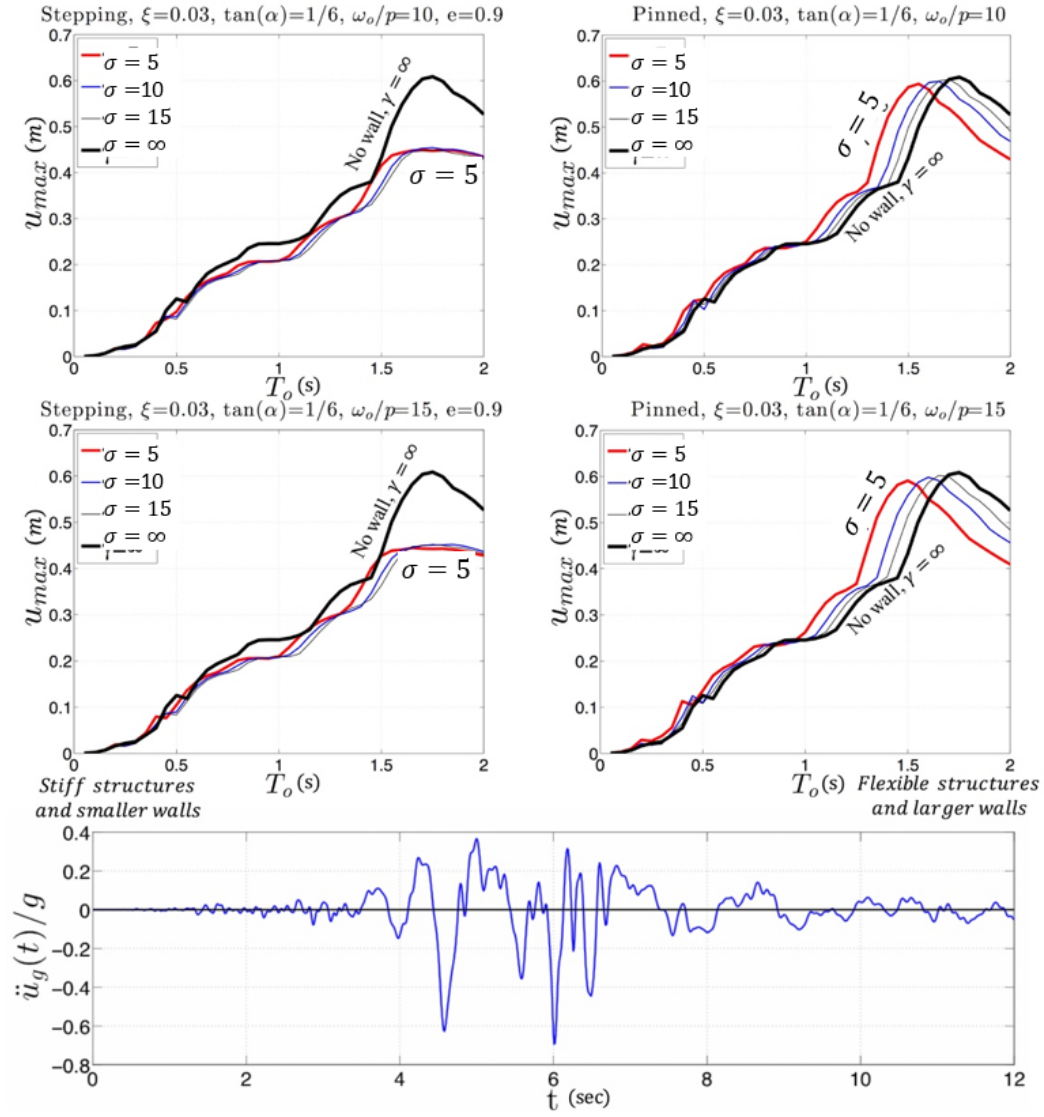


Figure 2.12: Displacement spectra of an elastic SDOF oscillator coupled with a stepping wall (left) and a pinned wall (right) for three values of the mass ratio $\sigma = m_s/m_w = 5, 10$ and 20 and two values of the wall size, $\omega_o/p = 10$ and 15 when subjected to the Takarazuka/000 ground motion recorded during the 1995 Kobe, Japan earthquake (bottom).

Pulse Spectra of an Elastic Oscillator Coupled with a Rocking-Wall

In an effort to further illustrate the dynamics of an elastic structure with a rocking wall (either stepping or pinned), this section presents response spectra to a pulse excitation [1, 4, 50, 68–70]. The choice of the specific functional expression to approximate the main pulse of a coherent ground motion has limited significance in this work. What is important to recognize is that several strong ground motions contain a distinguishable acceleration pulse that is responsible for most of the structural displacements. A mathematically rigorous and easily reproducible methodology based on wavelet analysis to extract the best mathematical pulse for a given pulse-like record has been recently proposed by Vassiliou and Makris [71].

Consider that the SDOF system shown in Figure 1 or Figure 2 is subjected to an acceleration pulse with amplitude a_p and pulse duration, $T_p = 2\pi/\omega_p$. From equations 2.26 and 2.27 or equation 2.28, it results that the response of the SDOF-system when subjected to an acceleration pulse is a function of 8 independent variables.

$$u_{max} = f(\omega_o, \xi, p, \alpha, \sigma, g, a_p, \omega_p) \quad (2.29)$$

The 8 independent variables appearing in equation 2.29 together with the dependent variable u_{max} (or θ_{max}) involve only two reference dimensions; that of length $[L]$ and the time $[T]$.

Accordingly to the Vachy-Bachington Π theorem [72], the number of dimensionless products with which the problem can be completely described is equal to [number of variables = 8 + 1 = 9] - [number of reference dimensions = 2] = 7. Herein we select as repeating variables the characteristics of the

pulse excitation, a_p and $\omega_p = 2\pi/T_p$ and the seven independent Π products are:

$$\Pi_u = \frac{u_{max}\omega_p^2}{a_p}, \Pi(\omega_o) = \omega_p/\omega_o, \Pi_\xi = \xi, \Pi(\omega_w) = \frac{\omega_p}{p}, \Pi_\alpha = \tan \alpha, \Pi_\sigma = \sigma \text{ and } \Pi_g = \frac{a_p}{g} \quad (2.30)$$

With these seven dimensionless Π products equation 2.30 reduces to:

$$\frac{u_{max}\omega_p^2}{a_p} = \phi\left(\frac{\omega_p}{\omega_o}, \xi, \frac{\omega_p}{p}, \tan \alpha, \sigma, \frac{a_p}{p}\right) \quad (2.31)$$

In this study we use as pulse excitation the second derivative of the Gaussian distribution, $e^{(-t^2/2)}$, known in the seismological literature as the symmetrical Ricker wavelet [73–75].

$$\ddot{u}_g(t) = a_p \left(1 - \frac{2\pi^2 t^2}{T_p^2}\right) e^{-\frac{1}{2} \frac{2\pi^2 t^2}{T_p^2}} \quad (2.32)$$

The value of $T_p = 2\pi/\omega_p$ is the period that maximizes the Fourier spectrum of the symmetric Ricker wavelet; therefore, $T_p = \pi\sqrt{2}$ sec, where s is the time from the peak pulse acceleration to the first zero-crossing that follows and a_p is the acceleration amplitude of the pulse.

The dimensionless maximum displacement, $\Pi_u = u_{max}\omega_p^2/a_p$ is a most useful quantity when one is interested in comparing the maximum displacements of various structural systems (say the effect of different size rocking walls). Nevertheless, for high frequency excitation pulse, the maximum displacement, u_{max} (which is usually a small quantity) is multiplied with a large number $= \omega_p^2/a_p$. Accordingly, the pulse spectra when plotted in terms of $\Pi_u = u_{max}\omega_p^2/a_p$ dilute the information that is meaningful in design, in particular when one is interested in understanding the effect of the pulse period to the structural response. For this purpose, a more meaningful normalized displacement is

introduced.

$$\frac{u_{max}}{R} = \frac{4}{3} \frac{\Pi_u \cdot \Pi_g}{\Pi_{m_\omega}^2} \quad (2.33)$$

The pulse spectra presented in this study cover to the extent possible the range of parameters of the moment-frame-rocking-wall systems reported in the literature.

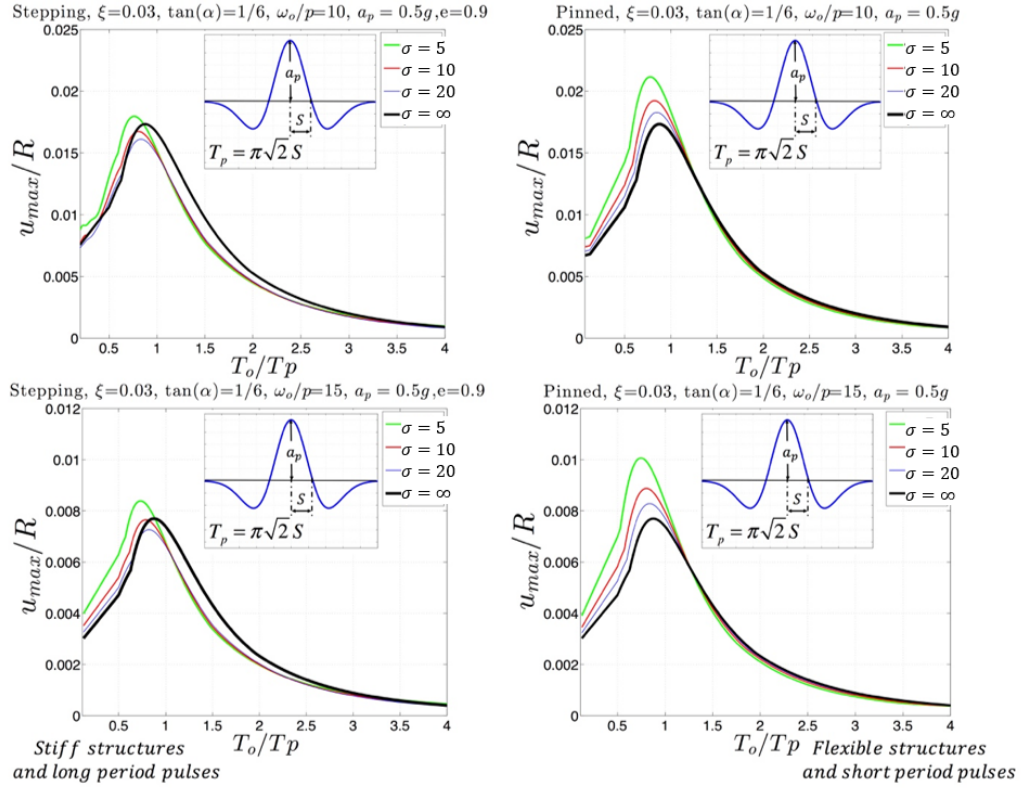


Figure 2.13: Normalized displacement spectra (u/R) of a SDOF oscillator coupled with a stepping wall (left) and a pinned wall (right) for three values of the mass ratio $\sigma = m_s/m_w = 5, 10$ and 20 and two values of the wall size, $\omega_o/p = 10$ and 15 when subjected to a symmetric Ricker wavelet with $a_p = 0.5g$.

Figures 2.13 and 2.14 show normalized displacement, u/R , spectra of a SDOF oscillator coupled with a stepping wall (left) and a pinned wall (right) for three values of the mass ratio, $\sigma = m_s/m_w =$

5, 10 and 20 and two values of the wall size, $\omega_o/p = 10$ and 15 when subjected to a symmetric Ricker wavelet with $a_p = 0.5g$ and $a_p = 1.0g$.

Figure 2.13 and 2.14 reveal that the SDOF oscillator coupled with a stepping wall (left plots) exhibits lower responses than the SDOF system oscillator coupled with a pinned wall (right plots). For long period excitations on stiff structures (say $T_o/T_p < 1.0$) the response of the SDOF oscillator coupled with a rocking wall is larger than response of the SDOF oscillator without wall. This behavior is more accentuated in the case of a pinned wall. For values of $T_o/T_p > 1$, the stepping wall suppresses the response of the SDOF oscillator, while the weight of the wall ($\omega = m_s/m_w$) appears to have marginal effect.

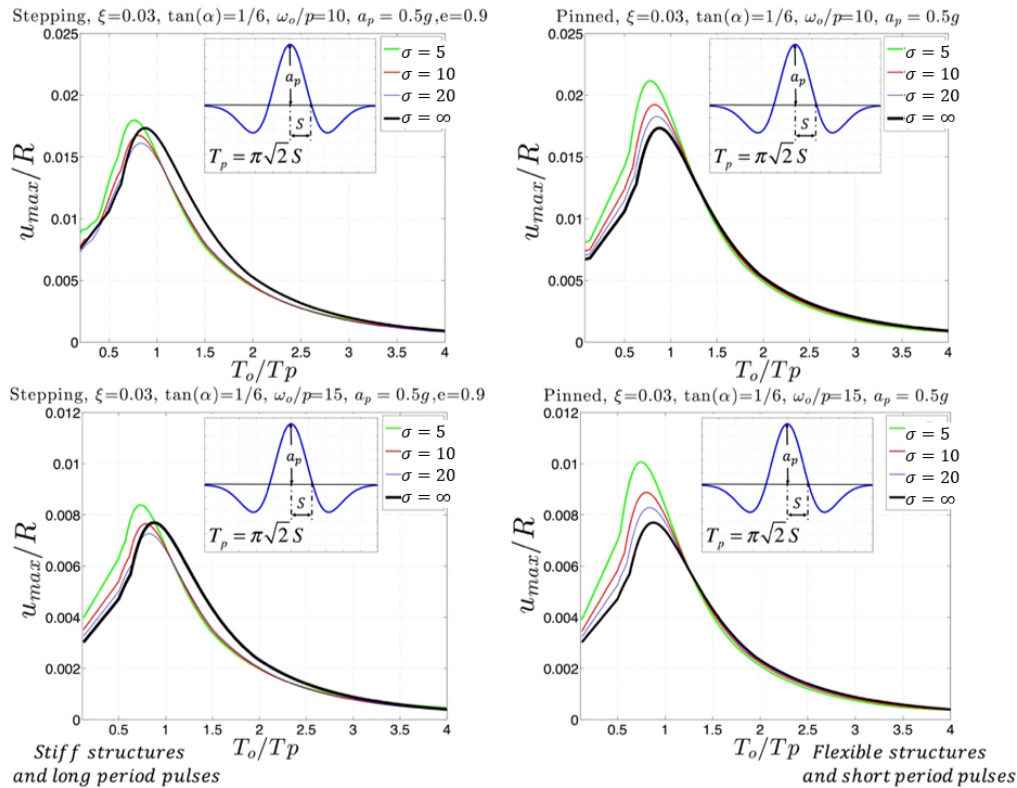


Figure 2.14: Normalized displacement spectra (u/R) of a SDOF oscillator coupled with a stepping wall (left) and a pinned wall (right) for three values of the mass ratio $\sigma = m_s/m_w = 5, 10$ and 20 and two values of the wall size, $\omega_o/p = 10$ and 15 when subjected to a symmetric Ricker wavelet with $a_p = 1.0g$.

Importance of the Length of the Coupling Arm

In the entire analysis of the study, it was assumed that the length of the coupling arm, L , appearing in Figure 2.1 and 2.2 is sufficiently large so that the quantity v^2/L^2 is much smaller than unity ($v^2/L^2 \ll 1$); and in this case $u = x$. There are cases however where the rocking wall is close enough to the laterally translating structure and in this case the length of the coupling arm, L , becomes an additional parameter of the problem.

Stepping rocking wall

For short arm lengths, equation 2.2 that offers the lateral translation of the elastic oscillator, u as a function of the positive rotation θ of the rocking wall needs to be replaced with:

$$u = L + R[\sin \alpha - \sin(\alpha - \theta)] - L\sqrt{1 - \frac{R^2}{L^2}[\cos(\alpha - \theta) - \cos \alpha]^2} \quad (2.34)$$

While, the last term with the radical in equation 2.34 complicates appreciably the expressions of its time derivatives as follows,

$$\dot{u} = R\dot{\theta} \left(\cos(\alpha - \theta) - \frac{R\sin(\alpha - \theta)[\cos \alpha - \cos(\alpha - \theta)]}{L\sqrt{1 - \frac{R^2}{L^2}[\cos(\alpha - \theta) - \cos \alpha]^2}} \right) \quad (2.35)$$

$$\begin{aligned} \ddot{u} = R\ddot{\theta} \left\{ \sin(\alpha - \theta) + \frac{R\cos(\alpha - \theta)[\cos \alpha - \cos(\alpha - \theta)] + R\sin^2(\alpha - \theta)}{L\sqrt{1 - \frac{R^2}{L^2}[\cos(\alpha - \theta) - \cos \alpha]^2}} \right. \\ \left. + \frac{R^3\sin^2(\alpha - \theta)[\cos \alpha - \cos(\alpha - \theta)]^2}{L^3\sqrt{\left(1 - \frac{R^2}{L^2}[\cos(\alpha - \theta) - \cos \alpha]^2\right)^3}} \right\} \\ + R\ddot{\theta} \left\{ \cos(\alpha - \theta) - \frac{R\sin(\alpha - \theta)[\cos \alpha - \cos(\alpha - \theta)]}{L\sqrt{1 - \frac{R^2}{L^2}[\cos(\alpha - \theta) - \cos \alpha]^2}} \right\} \end{aligned} \quad (2.36)$$

Dynamic equilibrium of the SDOF oscillator shown in Figure 2.1 with a short length link is:

$$m_s(\ddot{u} + \ddot{u}_g) = -F_s - c\dot{u} + T \cos \psi \quad (2.37)$$

while, dynamic equilibrium of the stepping rocking wall for $\theta > 0$ gives:

$$\begin{aligned} I\ddot{\theta} = & -(T \cos \psi)R \cos(\alpha - \theta) - (T \sin \psi)R \sin(\alpha - \theta) \\ & - m_w \ddot{u}_g R \cos(\alpha - \theta) - m_w g R \sin(\alpha - \theta) \end{aligned} \quad (2.38)$$

where

$$\sin \psi = \frac{R}{L} (\cos(\alpha - \theta) - \cos \alpha) \quad (2.39)$$

and $I = 4/3 m_w R^2$. Substitution of equations 2.34, 2.35 and 2.36 into equation 2.37 and after replacing the axial force T in equation 2.39 from 2.38 gives the equation of motion of the coupled SDOF system shown in Figure 2.1 for short coupling arms and $\theta > 0$.

Pinned rocking wall

For short arm lengths, equation 2.16 that offers the lateral translation of the elastic oscillator, u as a function of the rotation θ of the rocking wall needs to be replaced with:

$$u = L + h \sin \theta - L \sqrt{1 - \frac{h^2}{L^2} (1 - \cos \theta)^2} \quad (2.40)$$

Again, the last term with the radical in equation 2.40 complicates appreciably the expressions of its time derivatives. The time derivatives of the relative displacement offered by equation 2.40 are,

$$\dot{u} = h\dot{\theta} \left(\cos \theta + h \frac{(1 - \cos \theta) \sin \theta}{L \sqrt{1 - \frac{h^2}{L^2} (1 - \cos \theta)^2}} \right) \quad (2.41)$$

$$\ddot{u} = h\ddot{\theta} \left(\cos \theta + h \frac{(1 - \cos \theta) \sin \theta}{L \sqrt{1 - \frac{h^2}{L^2} (1 - \cos \theta)^2}} \right) + h\dot{\theta}^2 \left(-\sin \theta + h \frac{(1 - \cos \theta) \sin \theta}{L \sqrt{1 - \frac{h^2}{L^2} (1 - \cos \theta)^2}} + h \frac{\sin^2 \theta}{L \sqrt{1 - \frac{h^2}{L^2} (1 - \cos \theta)^2}} + \frac{h^3 (1 - \cos \theta)^2 \sin^2 \theta}{L^3 \sqrt{\left(1 - \frac{h^2}{L^2} (1 - \cos \theta)^2\right)^3}} \right) \quad (2.42)$$

Dynamic equilibrium of the SDOF oscillator shown in Figure 2.2 gives:

$$m_s(\ddot{u} + \ddot{u}_g) = -F_s + -c\dot{u} + T \cos \psi \quad (2.43)$$

while, dynamic equilibrium of the pinned rocking wall gives:

$$I\ddot{\theta} = -(T \cos \psi)h \cos \theta - (T \sin \psi)h \sin \theta + m_w g h \sin \theta - m_w \ddot{u}_g h \cos \theta \quad (2.44)$$

where

$$\sin \psi = \frac{h}{L} (1 - \cos \theta) \quad (2.45)$$

and $I = m_w R^2 (1/3 + \cos^2 \alpha)$.

Substitution of equations 2.40, 2.41 and 2.42 into equation 2.43 and after replacing the axial force T in equation 2.44 from 2.43, gives the equation of the motion for short coupling arms of the coupled SDOF system shown in Figure 2.2.

Figure 2.15 plots displacement spectra of the SDOF oscillator coupled with a stepping wall (left) and a pinned wall (right) with $\omega_o/p = 10$ and three values of the length of the coupling arm, $L = \infty, b$ and $b/10$, when excited by the Pacoima Dam/164 ground motion recorded during the 1971 San Fernando, California earthquake. The top plots are for $\sigma = m_s/m_w = 5$; whereas, the

bottom plots are for $\sigma = m_s/m_w = 20$ —that is for a lighter wall. The spectra shown on Figure 2.15 indicate that the length of the coupling arm, L , has a marginal effect on the response of the SDOF oscillator when coupled with a stepping wall (either stepping or pinned). Nevertheless, the pinned wall amplifies the response for most of the range of the spectrum. For the sake of simplicity of the analysis, it is assumed that the oscillator is elastic ($a = k_1/k_2 = 1$).

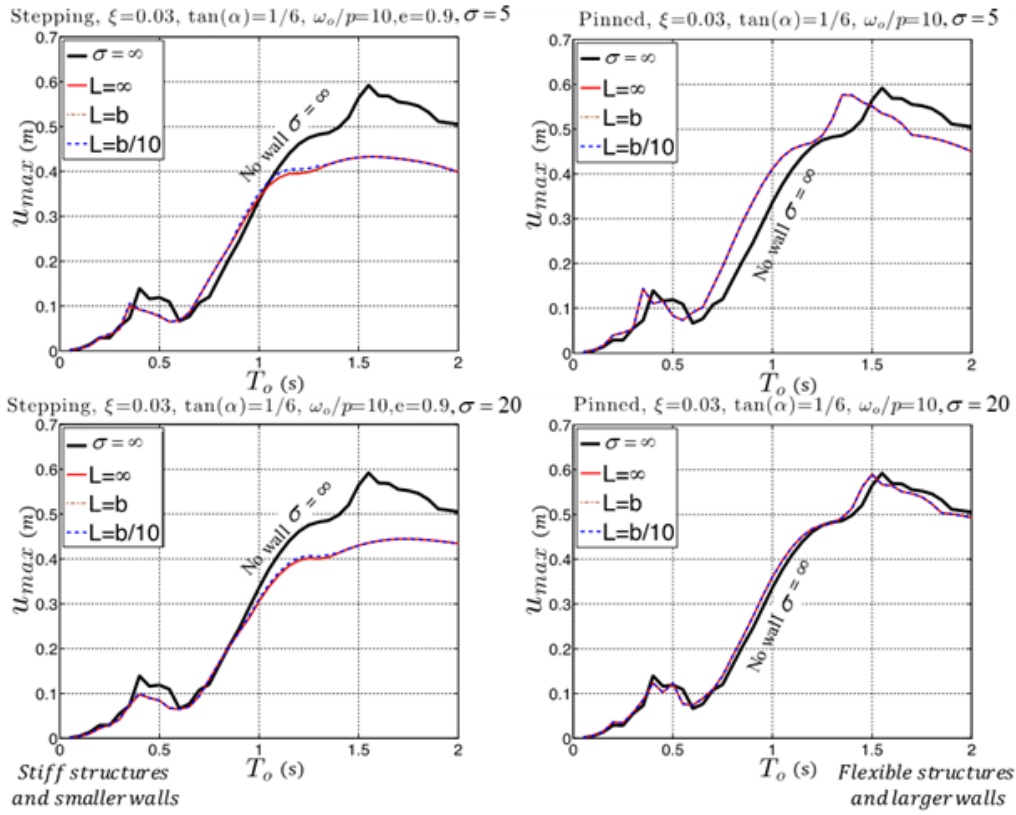


Figure 2.15: Displacement spectra of an elastic SDOF oscillator coupled with a stepping wall (left) and a pinned wall (right) with a short coupling arm for two values of the mass ratio $\sigma = m_s/m_w = 5$ (top) and 20 (bottom) and the wall size, $\omega_o/p = 10$ and three values of the length of the coupling arm, $L = \infty, b$ and $b/10$ when subjected to Pacoima Dam/164 ground motion recorded during the 1971 San Fernando, California earthquake.

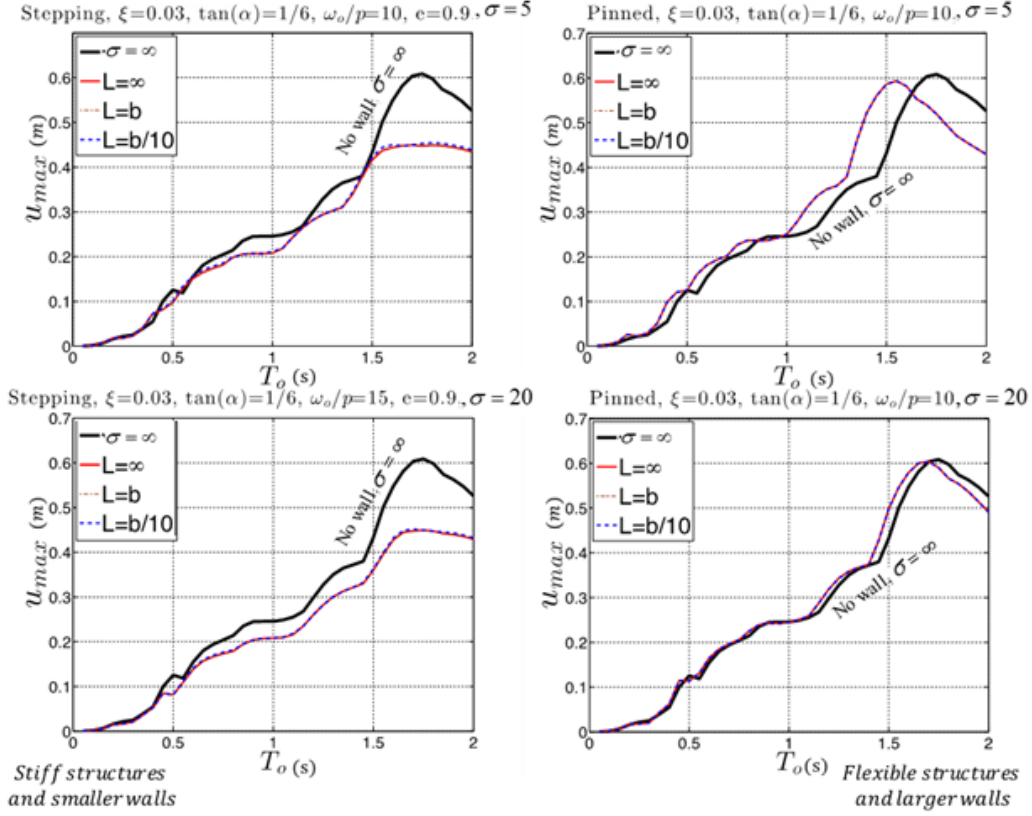


Figure 2.16: Displacement spectra of an elastic SDOF oscillator coupled with a stepping wall (left) and a pinned wall (right) with a short coupling arm for two values of the mass ratio $\sigma = m_s/m_w = 5$ (top) and 20 (bottom) and the wall size, $\omega_o/p = 10$ and three values of the length of the coupling arm, $L = \infty, b$ and $b/10$ when subjected to Takarazuka/000 ground motion recorded during the 1995 Kobe, Japan earthquake.

Same trends are observed in Figure 2.16 that plots displacement spectra of the SDOF oscillator coupled with a stepping wall (left) and a pinned wall (right) with $\omega_o/p = 10$ and three values of the length of the coupling arm, $L = \infty, b$ and $b/10$, when excited by the Takarazuka/000 ground motion recorded during the 1995 Kobe, Japan earthquake. Given that the coupling with a pinned wall invariably amplifies the displacement response, the concept of the pinned wall should be used with caution.

Conclusion

The dynamic response of a yielding SDOF oscillator coupled with a rocking wall is investigated in this part. Both configurations of a stepping and a pinned rocking wall that have been reported in the literature are examined. The full nonlinear equations of motions are derived and the study reaches through a comprehensive parametric analysis the following conclusions.

- The length of the coupling arm has a marginal effect on the response of the SDOF oscillator when coupled with a rocking wall.
- The response of the nonlinear SDOF idealization is in good agreement with the numerical solution from OpenSees for the four-story yielding frame. This favorable comparison validates the SDOF idealization adopted in this study.

When the yielding SDOF oscillator is coupled with a stepping rocking wall,

- The participation of the stepping wall suppresses the peak inelastic displacements in particular for more flexible structures with the heavier wall being most effective.
- Most importantly, the participation of the stepping rocking wall reduces drastically the permanent displacements which vanish completely as the weight of the wall increases.

When the yielding SDOF oscillator is coupled with a pinned rocking wall, opposite trends are observed:

- The participation of the pinned rocking wall increases in general the peak inelastic displacements with the heavier wall being most unfavorable.

- Pinned rocking wall increases the permanent displacements through a wide range of the response spectrum. This unfavorable response is mainly because the moment from the weight of a pinned rocking wall works against the stability of the system. Accordingly, the coupling a yielding frame with a pinned rocking wall may result to unfavorable response and should be used with caution.

CHAPTER 3: VERTICALLY RESTRAINED ROCKING WALL

Dynamics of a Yielding Oscillator Coupled with a Vertically Restrained Stepping Rocking Wall

This chapter of the study examines the dynamic response of a yielding single-degree-of-freedom (SDOF) structure, with mass m_s , pre-yielding stiffness k_1 , post yielding stiffness k_2 and strength Q , that is coupled with a free-standing stepping rocking wall of size $R = \sqrt{b^2 + h^2}$, slenderness $\tan \alpha = b/h$, mass m_w and moment of inertia about the pivoting (stepping) points O and O' , $I = 4/3 m_w R^2$, that is vertically restrained with an elastic tendon with axial stiffness EA which can be prestressed with a prestressing force P_o . In the interest of simplicity, it is assumed that the arm with length, L , that couples the motion is articulated at the center of mass of the rocking wall at a height, h , from its foundation as shown in Figure 3.1.

During rocking motion of the vertically restrained wall, the tendon is elongated by [30]

$$e = \sqrt{2} R \sin \alpha \sqrt{1 - \cos \theta} \quad (3.1)$$

In addition to the elongation, e , given by equation 3.1, the analysis accounts for an initial elongation

$$e_o = \frac{P_o}{EA/2h} \quad (3.2)$$

due to a possible initial postensioning force, P_o .

Accordingly, during rocking motion, the restoring moment on the rocking wall from the tendon alone is [30]

$$M_r = -R \sin \alpha \sin \theta \left(\frac{1}{2} EA \tan \alpha + \frac{P_o}{\sqrt{2} \sqrt{1 - \cos \theta}} \right) \quad (3.3)$$

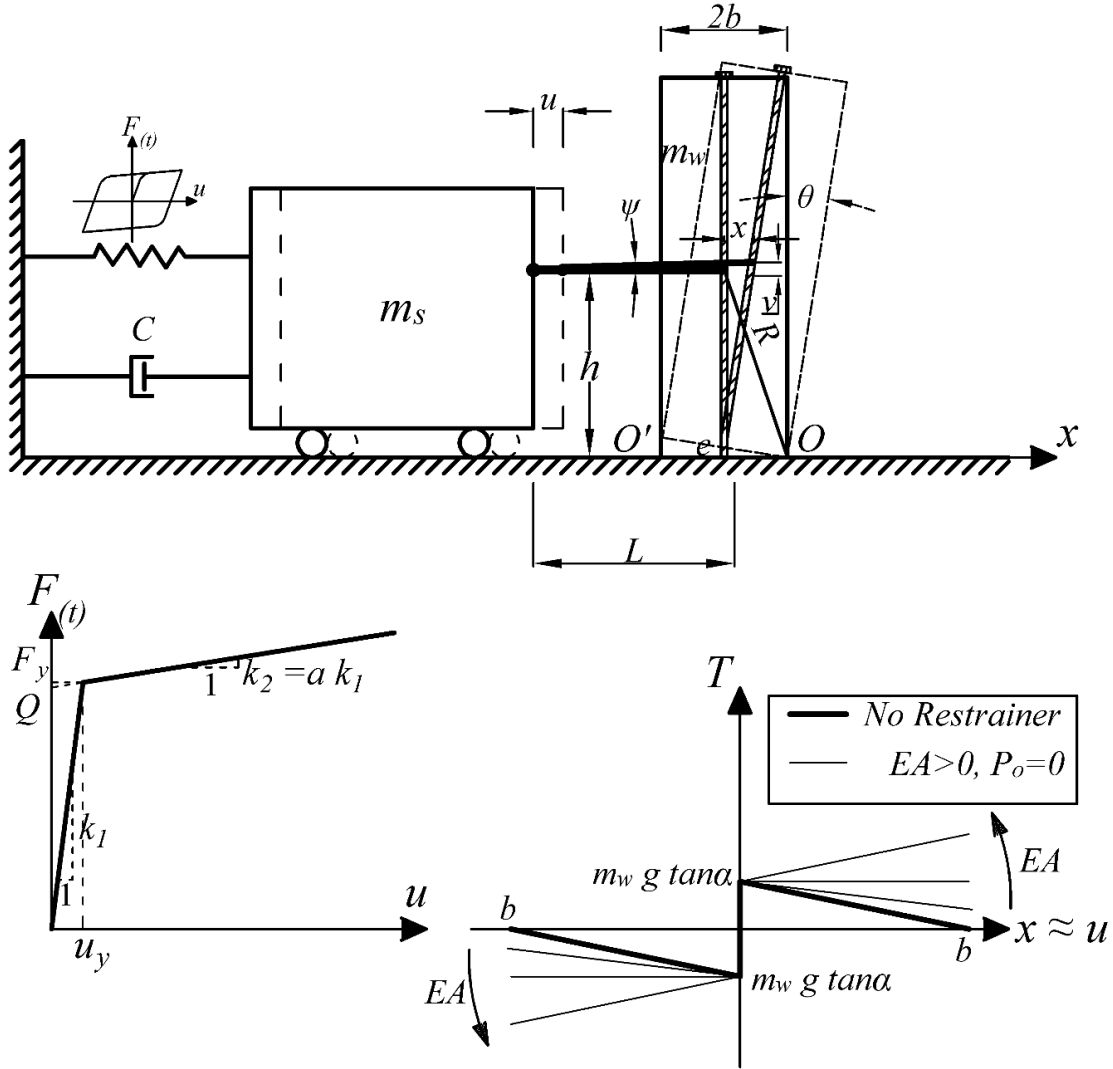


Figure 3.1: Yielding single-degree-of-freedom oscillator coupled with a vertically restrained stepping rocking wall.

With reference to Figure 3.1 (bottom), as the elasticity of the tendon increases it offsets the negative stiffness originating from rocking. The value of the axial stiffness of the tendon that is needed to introduce positive stiffness is [30]

$$\frac{EA}{m_w g} > 2 \frac{1}{\tan^2 \alpha} \quad (3.4)$$

For instance, for a slenderness value, $\tan \alpha = 1/6$, a rigid-plastic behavior is reached when $EA/(m_w g) =$

72.

Case 1: $\theta > 0$

For positive rotations ($\theta > 0$), dynamic equilibrium of the vertically restrained stepping rocking wall with mass m_w shown in Figure 3.1, gives:

$$I\ddot{\theta} = -TR\cos(\alpha - \theta) - m_w g R \sin(\alpha - \theta) - m_w \ddot{u}_g R \cos(\alpha - \theta) - R \sin \alpha \sin \theta \left(\frac{1}{2} EA \tan \alpha + \frac{P_o}{\sqrt{2}\sqrt{1 - \cos \theta}} \right) \quad (3.5)$$

where P_o is the initial post-tensioning force and EA is the axial stiffness of the elastic tendon. The axial force T appearing in equation (3.5) is replaced with the help of equations (2.5) and (2.6), whereas for a rectangular stepping wall, $I = 4/3 m_w R^2$. Accordingly, equation (3.5) assumes the form:

$$\begin{aligned} & \frac{4}{3} m_w R^2 \ddot{\theta} + [m_s(\ddot{u} + \ddot{u}_g) + a k_1 u(t) + (1 - a) k_1 u_y z(t) + c \dot{u}] R \cos(\alpha - \theta) \\ & = -m_w R [\ddot{u}_g \cos(\alpha - \theta) + g \sin(\alpha - \theta)] - R \sin \alpha \sin \theta \left(\frac{1}{2} EA \tan \alpha + \frac{P_o}{\sqrt{2}\sqrt{1 - \cos \theta}} \right) \end{aligned} \quad (3.6)$$

Upon dividing with $m_w R$ equation (3.6) gives:

$$\begin{aligned} & \frac{4}{3} R \ddot{\theta} + [\sigma(\ddot{u} + \ddot{u}_g) + a \frac{k_1}{m_w} u(t) + (1 - a) \frac{k_1}{m_w} u_y z(t) + \frac{c}{m_w} \dot{u}] \cos(\alpha - \theta) \\ & = -\ddot{u}_g \cos(\alpha - \theta) - g \sin(\alpha - \theta) - \sin \alpha \sin \theta \left(\frac{1}{2} \frac{EA}{m_w} \tan \alpha + \frac{P_o}{m_w \sqrt{2}\sqrt{1 - \cos \theta}} \right) \end{aligned} \quad (3.7)$$

in which $\sigma = m_s/m_w$ is the mass ratio parameter.

Substitution of the expressions of the relative displacement, velocity and acceleration given by equations (2.2) to (2.4) for positive rotations, and after dividing with R equation (3.7) is expressed

only in terms of the variable, $\theta(t)$.

$$\begin{aligned}
& \left(\frac{4}{3} + \sigma \cos^2(\alpha - \theta)\right) \ddot{\theta} + \sigma \cos(\alpha - \theta) [a \omega_1^2 (\sin \alpha - \sin(\alpha - \theta)) + 2\xi \omega_1 \dot{\theta} \cos(\alpha - \theta) \\
& + \dot{\theta}^2 \sin(\alpha - \theta) + (1 - a) \omega_1^2 \frac{u_y}{R} z(t)] \\
& = -\frac{g}{R} [(\sigma + 1) \frac{\ddot{u}_g}{g} \cos(\alpha - \theta) + \sin(\alpha - \theta) + \sin \alpha \sin \theta \left(\frac{1}{2} \frac{EA}{m_w g} \tan \alpha + \frac{P_o}{m_w g} \frac{1}{\sqrt{2} \sqrt{1 - \cos \theta}}\right)]
\end{aligned} \tag{3.8}$$

where $\omega_1 = \sqrt{k_1/m_s}$ is the pre-yielding undamped frequency and $\xi = c/(2m_s \omega_1)$ is the pre-yielding viscous damping ratio of the SDOF oscillator. Equation (3.8) is the equation of motion for positive rotations of the coupled system shown in Figure 3.1.

Case 2: $\theta < 0$

For negative rotations one can follow the same reasoning and the equation of the coupled system shown in Figure 3.1 is:

$$\begin{aligned}
& \left(\frac{4}{3} + \sigma \cos^2(\alpha + \theta)\right) \ddot{\theta} - \sigma \cos(\alpha + \theta) [a \omega_1^2 (\sin \alpha - \sin(\alpha + \theta)) - 2\xi \omega_1 \dot{\theta} \cos(\alpha + \theta) \\
& + \dot{\theta}^2 \sin(\alpha + \theta) - (1 - a) \omega_1^2 \frac{u_y}{R} z(t)] \\
& = \frac{g}{R} [-(\sigma + 1) \frac{\ddot{u}_g}{g} \cos(\alpha + \theta) + \sin(\alpha + \theta) - \sin \alpha \sin \theta \left(\frac{1}{2} \frac{EA}{m_w g} \tan \alpha + \frac{P_o}{m_w g} \frac{1}{\sqrt{2} \sqrt{1 - \cos \theta}}\right)]
\end{aligned} \tag{3.9}$$

When parameters $EA/m_w g = P_o/m_w g = 0$, equations (3.8) and (3.9) collapse to the equations of motion presented in [47, 51] for a yielding SDOF oscillator coupled with a rocking wall with no vertical restrainer. The terms multiplied with the parameter $\sigma = m_s/m_w$ are associated with the dynamics of the yielding SDOF oscillator; whereas, the remaining terms are associated with the dynamics of the rocking wall. When the SDOF oscillator is absent ($\sigma = \omega_1 = \xi = 0$), equations (3.8) and (3.9) reduce to the equations of motion of the solitary restrained rocking wall [30] since the frequency parameter p for rectangular walls is $p = \sqrt{3g/4R}$ [27, 28, 76]. Equations 3.8 and 3.9 reveal that the effect of tendon (EA and P_o) is different than the effect of a heavier wall (lower σ). These differences are illustrated in the response spectra presented later in the chapter.

During the oscillatory motion of the coupled system shown in Figure 3.1, aside from the energy that is dissipated from the inelastic behavior of the SDOF oscillator and the idealized viscous damping, additional energy is also lost during impact when the angle of rotation reverses. At this instant it is assumed that the rotation of the rocking wall continues smoothly from points O to O' ; nevertheless, the angular velocity, $\dot{\theta}_2$, after the impact is smaller than the angular velocity, $\dot{\theta}_1$, before the impact. Given that the energy loss during impact is a function of the wall-foundation interface, the coefficient of restitution, $e = \dot{\theta}_2 / \dot{\theta}_1 < 1$, is introduced as a parameter of the problem. In this study the coefficient of restitution assumes the value of $e = 0.9$.

Minimum Acceleration Needed to Initiate Uplift of The Coupled, Vertically Restrained Rocking Wall

With reference to Figure 3.1, during an infinitesimal admissible horizontal displacement δu , application of the principle of virtual work (when damping forces are neglected) gives

$$m_s \ddot{u}_g \delta u + m_w \ddot{u}_g \delta u = m_w g \delta v + \frac{1}{2} k \delta u^2 + \frac{1}{2} \frac{EA}{L} \delta v^2 + P_o \delta v \quad (3.10)$$

where δv is the corresponding infinitesimal vertical displacement of the center of mass of the rocking wall that is associated with δu . Assuming a positive rotation, for a horizontal displacement, u , given by equation (2.2), the associated vertical displacement v is

$$v = R[\cos(\alpha - \theta) - \cos \alpha] \quad (3.11)$$

From the calculus of variations [77]

$$\begin{aligned} \delta u &= \frac{du}{d\theta} \delta \theta \\ \delta v &= \frac{dv}{d\theta} \delta \theta \end{aligned} \quad (3.12)$$

Equation 3.12, in association with equations 2.2 and 3.11 give

$$\delta u = R \cos(\alpha - \theta) \delta \theta \quad (3.13)$$

and

$$\delta v = R \sin(\alpha - \theta) \delta \theta \quad (3.14)$$

Substitution of equations (3.13) and (3.14) into the equation of virtual work 3.10, after dropping the terms $\frac{1}{2}k\delta u^2$ and $\frac{EA}{L}\delta v^2$ which involve second order variations, gives

$$m_w(\sigma + 1)\ddot{u}_g R \cos(\alpha - \theta) \delta \theta = (m_w g + P_o) R \sin(\alpha - \theta) \delta \theta \quad (3.15)$$

At the initiation of uplift, $\theta = 0$; therefore, equation (3.15) indicates that the uplift acceleration of the system is:

$$\ddot{u}_g = \frac{1}{\sigma + 1} g \tan \alpha \left(1 + \frac{P_o}{m_w g}\right) \quad (3.16)$$

Parameters of The Problem

The Bouc-Wen model described by equations (2.6) and (2.7) is a phenomenological model of hysteresis originally proposed by Bouc 1967 [57] and subsequently generalized by Wen [52, 58] and Baber and Wen [59]. It is a versatile model that can capture various details of the nonlinear force-displacement loop. Subsequent studies on the modeling of yielding systems by Constantinou and Adnane [60] concluded that when certain constraints are imposed on the parameters β and γ ($\beta + \gamma = 1$), the model reduces to a viscoplastic element with well-defined physical characteristics. The Bouc-Wen model essentially builds on the bilinear idealization shown in the bottom-left of Figure 3.1.

For the five-parameter system shown with the bilinear idealization. (k_1 = pre-yielding stiffness, k_2 = post-yielding stiffness, u_y = yield displacement, Q = strength and F_y = yielding force), only three parameters are needed to fully describe the bilinear behavior (see for instance [61]). In this work, the authors select the pre-yielding stiffness $k_1 = m_s \omega_1^2$, the post-yielding stiffness $k_2 = a k_1$ and the strength of the structure Q . With reference to Figure 3.1 (bottom-left), $F_y = k_1 u_y = Q + k_2 u_y$. Accordingly, $u_y = Q/(k_1 - k_2)$ and $F_y = k_1 Q/(k_1 - k_2)$. The parameters β , γ and n appearing in equation 3.7 are established from past studies on the parameter identification of yielding concrete structures and assume the values: $\beta = 0.95$, $\gamma = 0.05$ and $n = 2$ [62, 63]. With the parameters $\beta = 0.95$, $\gamma = 0.05$ and $n = 2$ being established, the peak inelastic displacement, u_{max} of the SDOF system shown in Figure 3.1 is a function of the following parameters:

$$u_{max} = f(\omega_1, \frac{Q}{m_s}, a, \xi, p, \tan \alpha, \sigma, g, EA, P_o, \text{parameters of excitation}) \quad (3.17)$$

In this study, it is assumed that upon yielding, the structure maintains a mild, positive, post-yielding stiffness = $k_2 = 0.05 k_1$, therefore $a = 0.05$ [62, 63]. Furthermore, it is assumed that the pre-yielding damping ratio, $\xi = C/(2m_s \omega_1) = 0.03$ and focuses on rocking walls with slenderness, $\tan \alpha = 1/6$.

Normal Forces at the Pivoting Corners

By increasing the axial stiffness, EA , of the vertical tendon one increases the lateral stiffness of the entire structural system; nevertheless, at present it is not clear to what extent a stiffer vertical tendon improves the seismic performance of the overall structure, or it merely contributes to accentuate the vertical reaction force at the pivoting points. With reference to Figure 3.2, a rotation of the wall = θ creates an elongation to the tendon = e , given by equation (3.1) In addition to gravity and inertia forces, the vertical reaction at the pivot corner, N , also balances the vertical forces from the

tendon

$$F_v = \frac{EA}{2h} e \cos \phi + P_o \cos \phi \quad (3.18)$$

Using that $e \cos \phi = b \sin \theta$ and $\cos \phi = \frac{1}{\sqrt{2}} \sqrt{1 + \cos \theta}$, equation (3.18) assumes the form

$$F_v = \frac{1}{2}EA \tan \alpha \sin \theta + \frac{P_o}{\sqrt{2}}\sqrt{1 + \cos \theta} \quad (3.19)$$

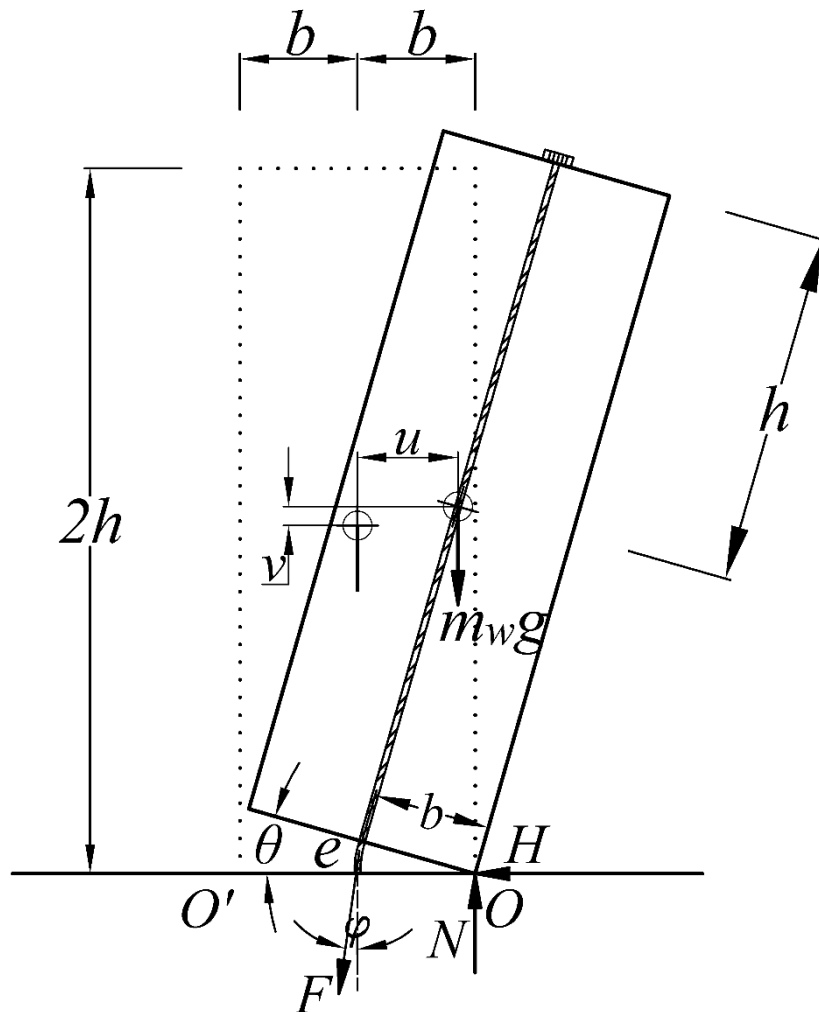


Figure 3.2: Free-body diagram of a rocking wall with an elastic tendon passing through its centerline.

During rocking motion, the vertical reaction at the pivoting corners, N , balances the weight of the wall, the inertia forces and the vertical force, F_v , from the tendon gives by equation (3.19)

$$N(t) = m_w \ddot{v} + m_w g + EA \left(\frac{1}{2} \tan \alpha \sin \theta + \frac{P_o}{EA} \frac{\sqrt{1 + \cos \theta}}{\sqrt{2}} \right) \quad (3.20)$$

where \ddot{v} is the vertical acceleration of the center of mass of the wall. For instance, for a positive rotation ($\theta > 0$), the vertical uplift of the center of mass of the wall is given by (3.11) and successive differentiation gives,

$$\dot{v} = R \dot{\theta} \sin(\alpha - \theta) \quad (3.21)$$

$$\ddot{v} = R [\ddot{\theta} \sin(\alpha - \theta) - \dot{\theta}^2 \cos(\alpha - \theta)] \quad (3.22)$$

By virtue of equation 3.22, the normalized to the weight of the wall vertical reaction of the pivoting point is given by

$$\frac{N(t)}{m_w g} = 1 + \frac{R}{g} [\ddot{\theta} \sin(\alpha - \theta) - \dot{\theta}^2 \cos(\alpha - \theta)] + \frac{1}{2} \frac{EA}{m_w g} \tan \alpha \sin \theta + \frac{1}{\sqrt{2}} \frac{P_o}{m_w g} \sqrt{1 + \cos \theta} \quad (3.23)$$

Figure 3.3 (left) plots displacement, $u(t)$, rotation, $\theta(t)$ and vertical-reaction, $N(t)$ (at the pivot points) time histories for a structure having, $T_1 = 0.8 \text{ sec}$, $Q/m_s = 0.08g$ which is coupled with a rocking wall with $\omega_1/p = 10$ ($p = 0.778 \text{ rad/sec}$), $\tan \alpha = 1/6$ and $\sigma = m_s/m_w = 10$ when excited by the Pacoima Dam/164 ground motion recorded during the 1971 San Fernando, California earthquake. The dashed line is when there is no wall, the heavy dark line is where there is a rocking wall without tendon; whereas the thinner solid lines show the response when a tendon is present without being pretensioned ($P_o = 0$). Figure 3.3 (left) shows that whereas a stiff tendon ($EA/(m_w g) = 200$) increases the vertical reaction at the pivot points by more than 50% its effect in reducing peak inelastic deformations is marginal. Figure 3.3 (right) reveals similar trends as those discussed for the

results of Figure 3.3 (left) when the inelastic structure is subjected to Erzincan NS ground motion recorded during 1992 Erzincan, Turkey earthquake.

Figure 3.4 plots displacement, $u(t)$, rotation $\theta(t)$ and vertical reaction at the pivot points, $N(t)$ time histories for a structure having $T_1 = 1.5$ sec, $Q/m_s = 0.12g$ which is coupled with a rocking wall with $\omega_1/p = 10$ ($p = 0.778\text{rad/sec}$), $\tan \alpha = 1/6$ and $\sigma = m_s/m_w = 10$ when excited by the same ground motions used in Figure 3.3. Figure 3.5 plots displacement, $u(t)$, rotation, $\theta(t)$, and vertical reaction at the pivot points, $N(t)$, time histories for a structure having the same parameters as those of the structural system of Figure 3.4; yet, now the vertical tendon is prestressed with $P_o = 0.5m_w g$ and subjected to the Newhall/360 ground motion recorded during 1994 Northridge, California earthquake (left) and the Takarazuka/000 ground motion recorded during the 1995, Kobe, Japan earthquake (right). Similar to the results presented in Figure 3.3 to 3.5 show that the effect of the vertical tendon is marginal other than increasing by more than 50% the vertical reaction of the pivot points.

While equations 3.8 and 3.9 describe merely the dynamics of the SDOF idealization shown in Figure 3.1, they are of engineering value since they show the relative contribution of the various parameters of the problem. For instance, consider a moment frame-rocking wall system with mass ratio, $\sigma = m_s/m_w = 10$, when the rocking wall with slenderness, $\tan \alpha = 1/6$, is restrained with a stiff vertical tendon (say $EA/m_w g = 200$) and subjected to a ground motion with an acceleration amplitude of $\ddot{u}_g = 0.5g$. The right-hand side of equations 3.8 and 3.9 show that the term associated with the input ground acceleration, $(\sigma + 1)\frac{\ddot{u}_g}{g} \cos(\alpha - \theta)$, is of the order of 5; whereas, the term associated with the contribution of the tendon is $\frac{1}{2} \sin \alpha \tan \alpha \frac{EA}{m_w g} \sin \theta \approx 2.74\theta$. Given that for most cases of interest θ_{max} is less than $\alpha/10 \approx (\tan \alpha)/10$ (see Figures 3.4 and 3.5), the contribution of the tendons at peak wall rotation $= \theta_{max}$, is of the order of $2.74 \tan \alpha/10 \approx 0.05$ —that is two order of magnitude smaller than the inertia term associated with the input ground acceleration. This explains the marginal contribution of the vertical tendons even when they are stiff.

$$T_1 = 0.8s, \frac{Q}{m_s g} = 0.08, \frac{\omega_1}{p} = 10, \tan \alpha = \frac{1}{6}, \sigma = 10, \xi = 0.03, \frac{P_o}{m_w g} = 0$$

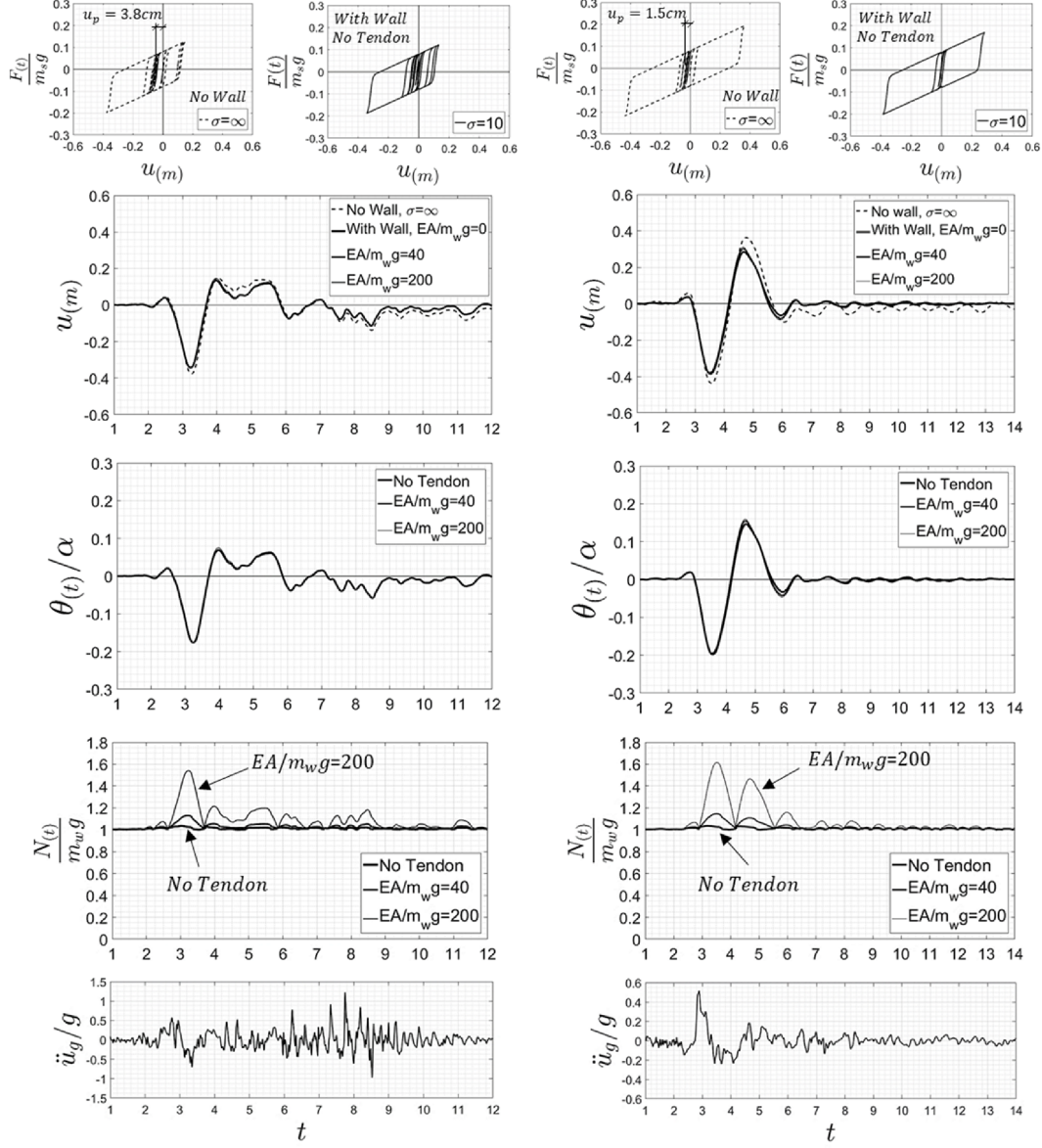


Figure 3.3: Time-history analysis of a nonlinear SDOF oscillator coupled with a vertically restrained stepping rocking wall with preyielding period, $T_1 = 0.8$ sec, normalized strength $Q/m_s = 0.08g$, wall size ratio, $\omega_1/p = 10$ and structure-to-wall mass ratio, $\sigma = 10$ when subjected to the 1971 Pacoima Dam/164 ground motion (left) and the 1992 Erzincan NS, Turkey ground motion (right). Even stiff tendons ($EA/m_w g = 200$) have a marginal effect on the response, except of drastically increasing the vertical reaction (more than 50%) at the pivot points. Tendons are not prestressed, $P_o/m_w g = 0$.

$$T_1 = 1.5s, \frac{Q}{m_s g} = 0.12, \frac{\omega_1}{p} = 10, \tan \alpha = \frac{1}{6}, \sigma = 10, \xi = 0.03, \frac{P_o}{m_w g} = 0$$

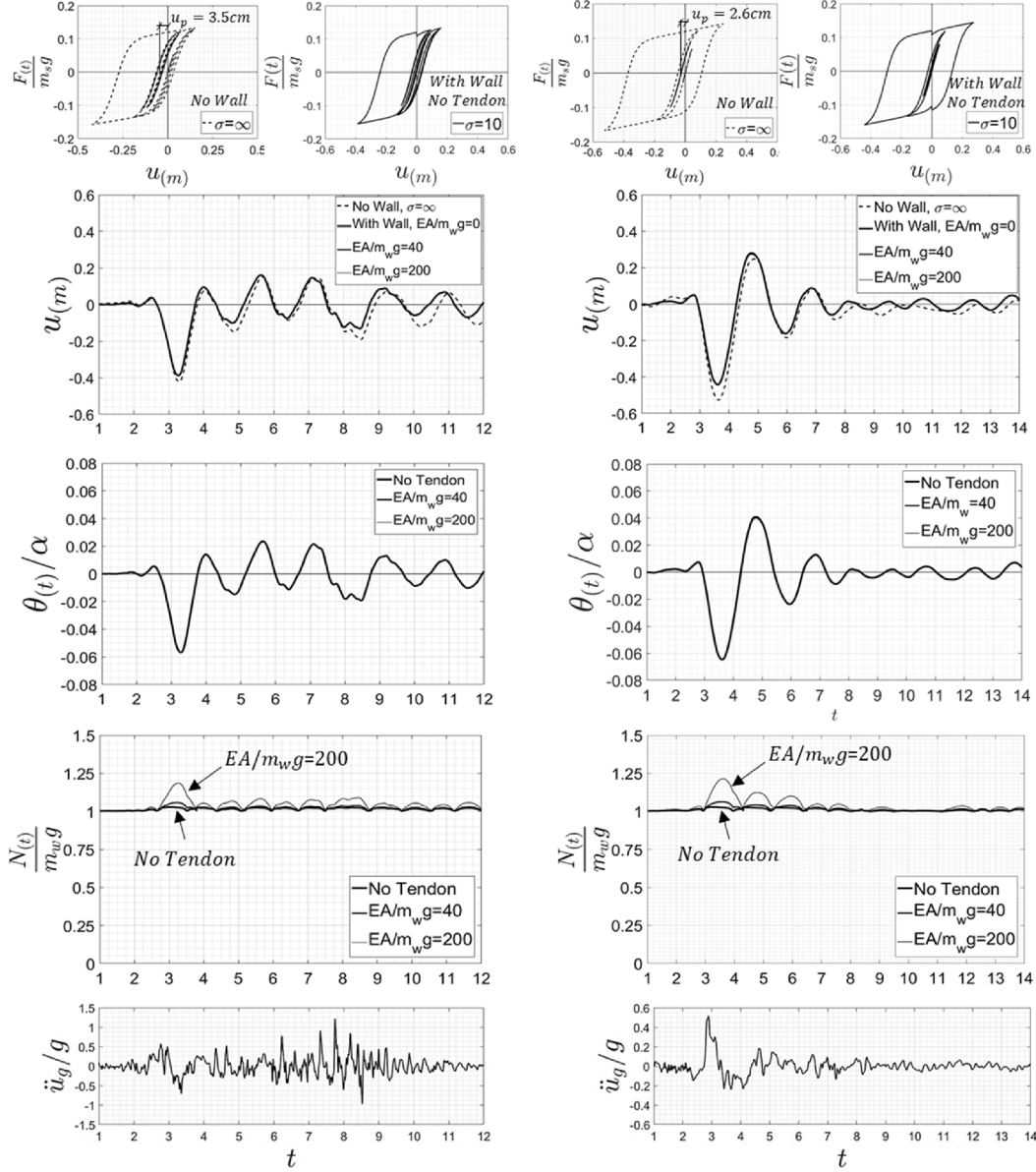


Figure 3.4: Time-history analysis of a nonlinear SDOF oscillator coupled with a vertically restrained stepping rocking wall with preyielding period, $T_1 = 1.5$ sec, normalized strength $Q/m_s = 0.12g$, wall size ratio, $\omega_1/p = 10$ and structure-to-wall mass ratio, $\sigma = 10$ when subjected to the 1971 Pacoima Dam/164 ground motion (left) and the 1992 Erzincan NS, Turkey ground motion (right). Even stiff tendons ($EA/m_w g = 200$) have a marginal effect on the response, except of drastically increasing the vertical reaction (more than 50%) at the pivot points. Tendons are not prestressed, $P_o/m_w g = 0$.

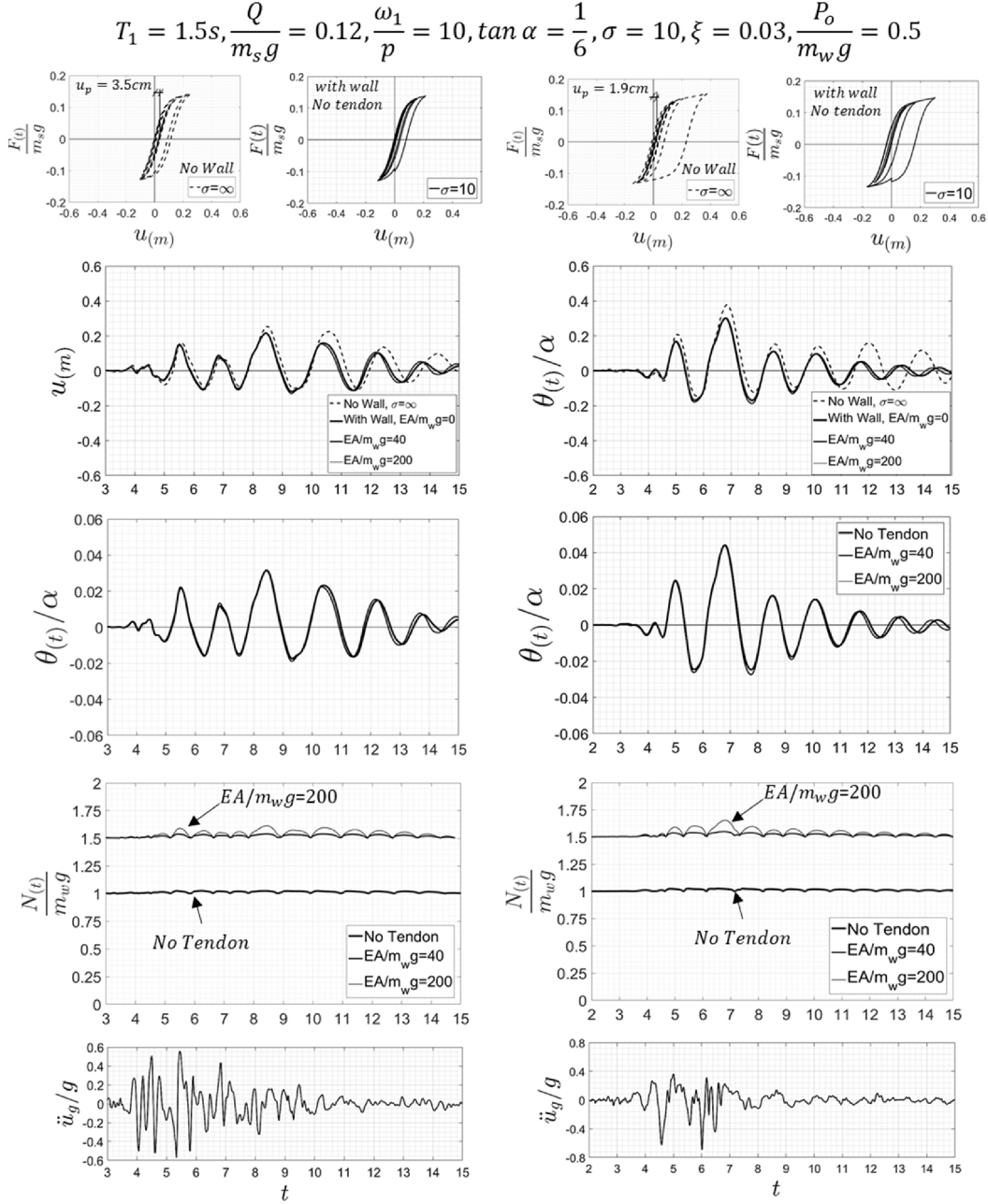


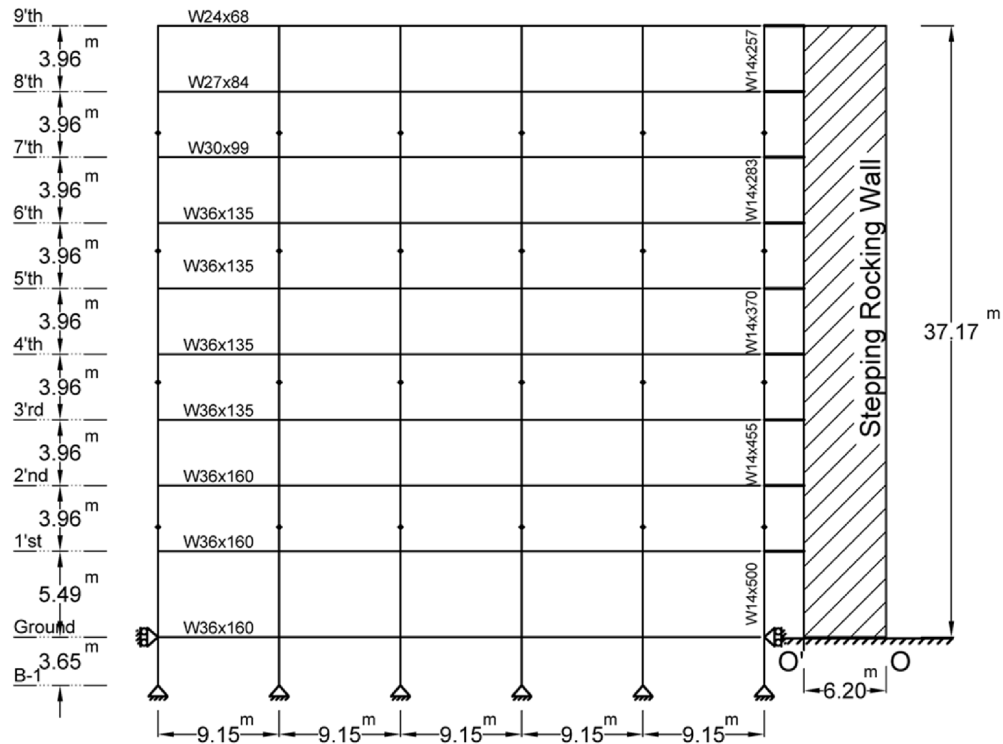
Figure 3.5: Time-history analysis of a nonlinear SDOF oscillator coupled with a vertically restrained stepping rocking wall with preyielding period, $T_1 = 1.5$ sec, normalized strength $Q/m_s = 0.12g$, wall size ratio, $\omega_1/p = 10$ and structure-to-wall mass ratio, $\sigma = 10$ when subjected to the 1994 Newhall/360 ground motion (left) and the 1995 Takarazuke/000, Japan ground motion (right). Even stiff tendons ($EA/m_w g = 200$) have a marginal effect on the response, except of drastically increasing the vertical reaction (more than 50%) at the pivot points. Tendons are not prestressed, $P_o/m_w g = 0$.

Validation of the SDOF-Idealization

In this section the dependability of the single-degree-of-freedom idealization shown in Figure 3.1 is examined against the results obtained with the open-source code OpenSees [78] when analyzing the nine-story moment resisting steel structure designed for the SAC Phase II Project [79]. This structure that is well-known to the literature [80, 81] was designed to meet the seismic code (pre-Northridge Earthquake) and represents typical medium-rise buildings designed for the greater area of Los Angeles, California.

This moment-resisting, steel building is 40.82 *m* tall with 9-stories above ground level and a basement. The bays are 9.15 *m* wide, with five bays in north-south (N-S) and east-west (E-W) directions. Floor-to-floor height of each story is 3.96 *m*, except for the basement and first floor which are 3.65 *m* and 5.49 *m* respectively as shown in Figure 3.6. Columns splices are on the 1st, 3rd, 5th and 7th floors and located 1.83 *m* above the beam-column joint. The column bases are modeled as pinned connection and it is assumed that the surrounding soil and concrete foundation walls are restraining the structure in horizontal direction at the ground level. The columns are 345 MPa wide-flange steel sections and the floor beams are composed of 248 MPa wide-flanges steel sections. All beam column connections of the frames are rigid except for the corner columns which are pinned in order to avoid bi-axial bending of the members. In this study, the exterior frame in N-S direction is chosen for the 2-D validation of our planar analysis.

To model the rocking surface of the wall the method used by Vassiliou et al. [66] is implemented. The rocking surface is modeled by zero-length fiber cross-section element placed between the ground and base of the wall as it described by Vassiliou et al. [66]. The fiber material is defined by non-linear material with no resistance in tension and elastic response in compression defined by using "*ENT=Elastic-No Tension*" material in OpenSees. The surface material is non-dissipative therefore, Hilder-Hughes-Taylor [84] dissipative time-stepping integration procedure is used [66].



Geometric and Physical Characteristics			
Beams [248 MPa]		Columns [345 MPa]	
• Ground-2nd level	W36x160	• B1-1st level	W14x500
• 3rd-6th level	W36x135	• 1st-3rd level	W14x455
• 7th level	W30x99	• 3rd-5th level	W14x370
• 8th level	W27x84	• 5th-7th level	W14x283
• 9th level	W24x68	• 7th-9th level	W14x257
Columns			
• Column sizes change at splices and they are marked on the figure. Indicates column splices			
Seismic mass:		Restraints:	
• Ground level	$9.5 \times 10^5 \text{ kg}$	Column splices are at 1.83 m w.r.t. beam-to-column joint; Columns pinned at base; Structure laterally restrained at 1st level.	
• 1st level	$1.0 \times 10^6 \text{ kg}$		
• 2nd-8th level	$9.89 \times 10^5 \text{ kg}$		
• 9th level	$1.07 \times 10^6 \text{ kg}$		

Figure 3.6: Top: Nine-story moment-resisting steel frame designed for the SAC Phase II Project coupled with a stepping rocking wall. Bottom: Geometric and physical characteristics pertinent to the 9-story SAC building.

The nonlinear response of the nine-story MDOF structure is computed with the nonlinear built-in model "Steel01" in OpenSees. It is a bilinear model at the stress-strain level with a backbone curve that is similar to the force-displacement curve shown in Figure 3.1. Accordingly, we have used an elastic modulus of $E = 210$ GPa, a strain hardening ratio (post-yield to elastic, pre-yield modulus ratio), $a = 0.03$ and a yield strength, $\sigma_y = 248$ MPa for beams and $\sigma_y = 345$ MPa for columns.

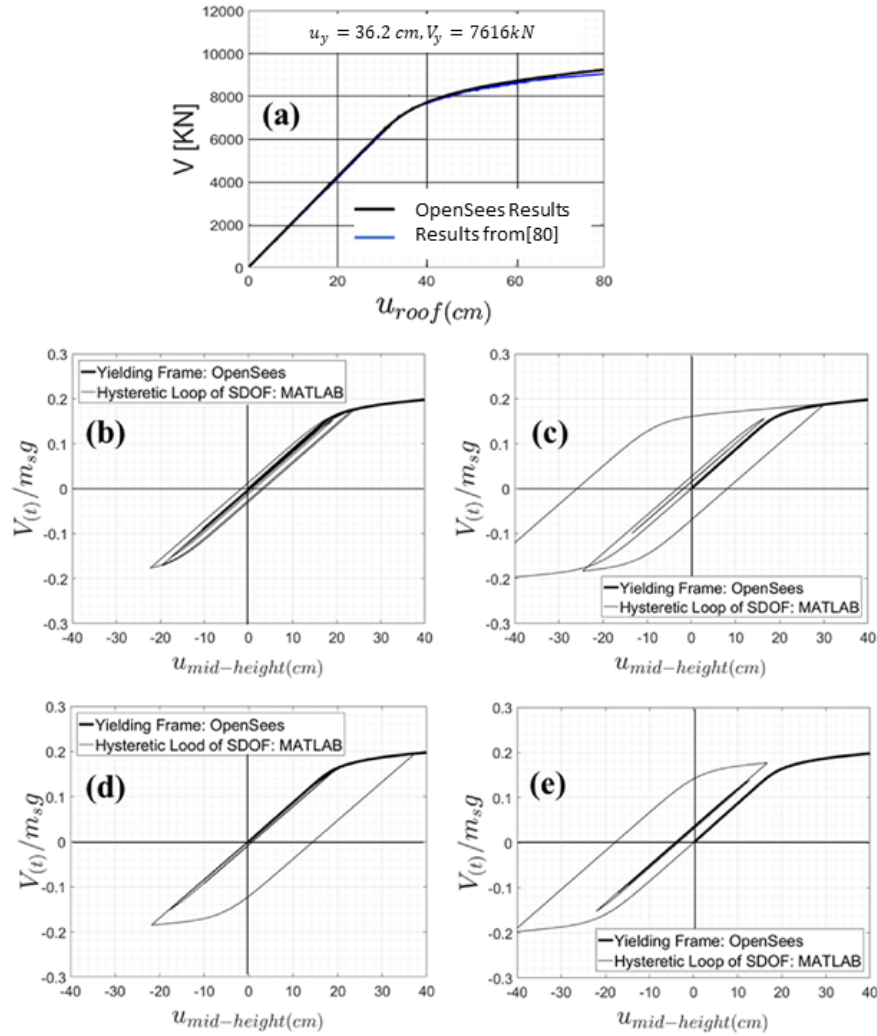


Figure 3.7: (a): Comparison of the computed push-over curve (base-shear vs roof displacement) of the 9-story moment-resisting steel building with the results reported by [80]. Base-shear versus displacement at mid-height computed with OpenSees of the 9-story steel building without rocking wall together with the corresponding force-displacement loops computed with MATLAB of the SDOF inelastic model shown in Figure 1 when excited with the 1994 Newhall/360, Northridge (b), the 1992 Erzincan NS, Turkey (c), the 1995 Takarazuka/000, Kobe (d) and the 1971 Pacoima Dam/164, Imperial Valley (e) ground motions.

Figure 3.7 (top) plots the computed push-over curve (base shear vs roof displacement) of the 9-story moment resisting steel building without rocking wall, which is essentially identical with the push-over curve presented in past investigations [80, 80, 81, 85, 86]. The resulting pre-yielding period of the building is $T_1 = 2.27\text{sec}$, while its normalized strength is $Q/m_s = 0.17g$.

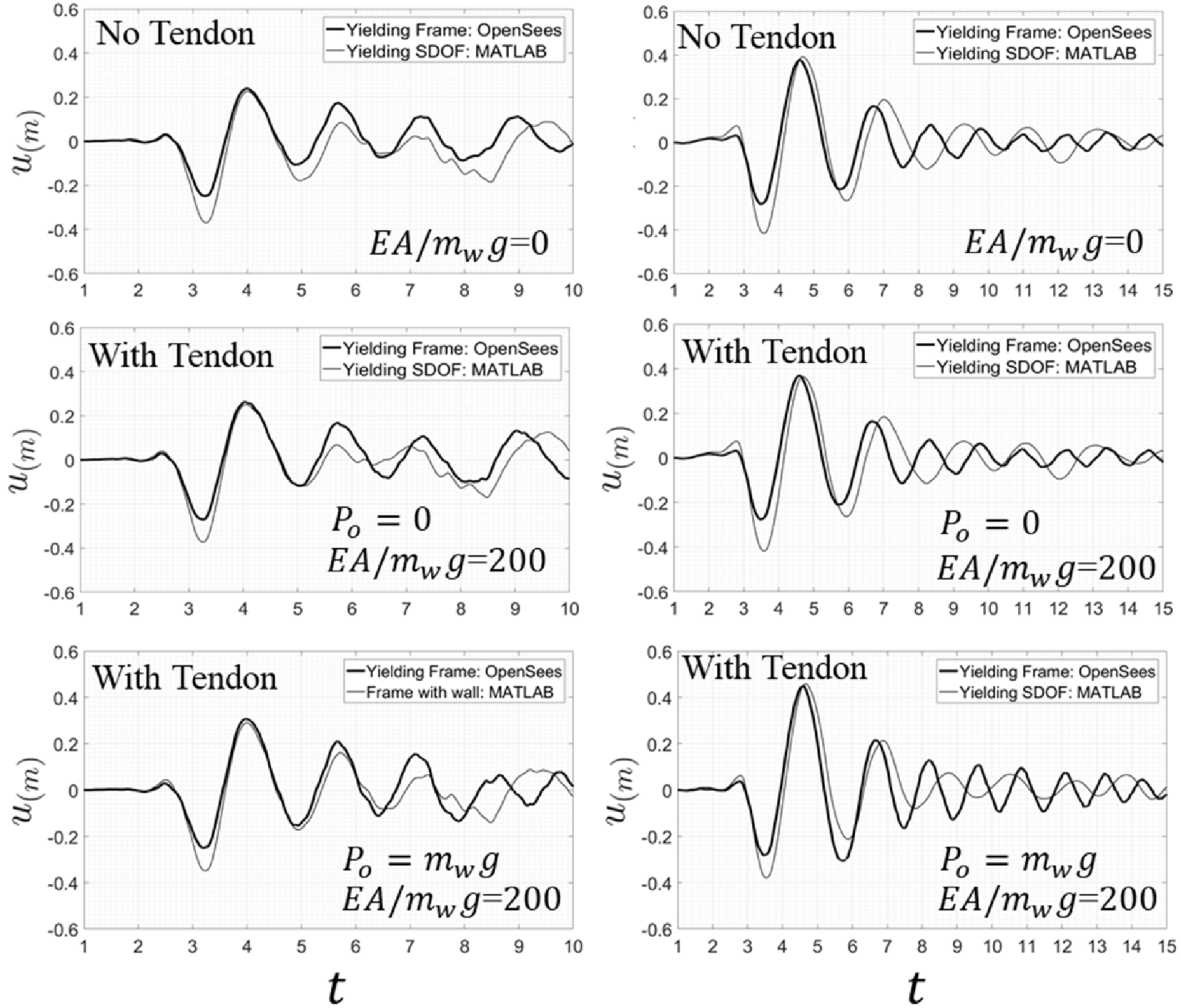


Figure 3.8: Comparison of the displacement time histories at mid-height of the 9-story steel building shown in Figure 6, computed with OpenSees with the displacement time-histories of the SDOF idealization shown in Figure 1, when excited with the 1971 Pacoima Dam/164, San Fernando, California (left) and the 1992 Erzincan NS, Turkey (right) ground motions.

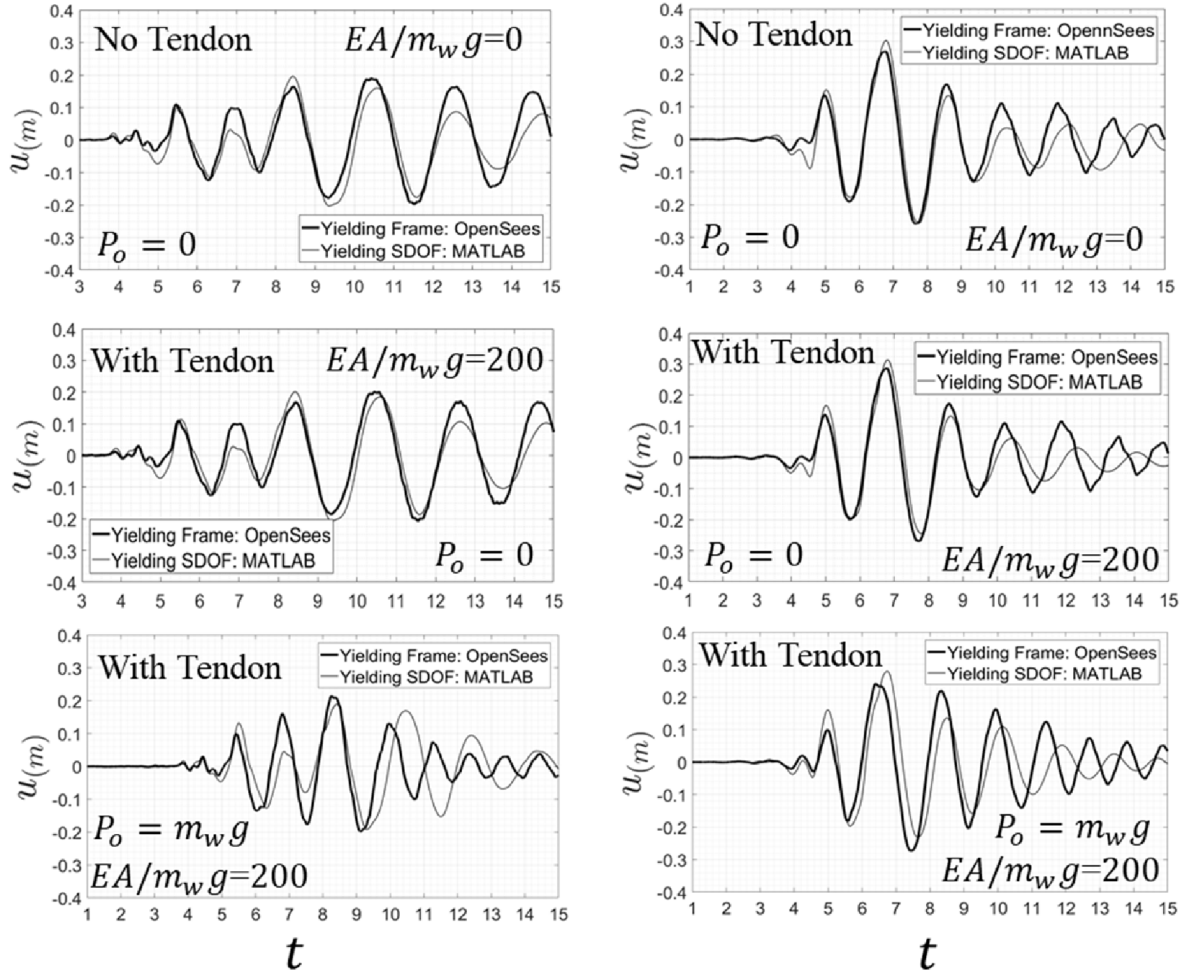


Figure 3.9: Comparison of the displacement time histories at mid-height of the 9-story steel building shown in Figure 6, computed with OpenSees with the displacement time-histories of the SDOF idealization shown in Figure 1, when excited with the 1994 Newhall/360, Northridge, California (left) and the 1995 Takarazuka/000, Kobe, Japan (right) ground motions.

The remaining four subplots in Figure 3.7 plot the base-shear versus the mid-height displacement of the 9-story building without rocking wall together with the corresponding force-displacement loops computed with Matlab of the SDOF inelastic model shown in Figure 3.1 when excited with the 1994 Newhall/360, Northridge (b), 1992 Erzincan NS, Turkey (c), the 1995 Takarazuka/000, Kobe (d) and the 1971 Pacoima Dam/164, Imperial Valley (e) ground motions. All four subplots show that the inelastic force-displacement loops of the SDOF model shown in Figure 1 follow with

fidelity the inelastic back-bone curve of the 9-story SAC building that is computed with OpenSees.

Figure 3.8 compares response histories computed with OpenSees at mid-height of the 9-story SAC steel building with the solutions obtained with MATLAB for the SDOF idealization shown in Figure 1. The top plots are when the rocking wall is not restrained (No tendon), the center plots are when the rocking wall is restrained with a stiff tendon with $EA/m_w g = 200$ without being prestressed ($P_o = 0$); while, the bottom plots are when the tendon with $EA/m_w g = 200$ is prestressed with $P_o = m_w g$. The left plots are when the structure is subjected to the Pacoima Dam/164 ground motion recorded during the 1971 San Fernando, California earthquake whereas the right plots are when the structure is subjected to the Erzincan NS ground motion recorded during the 1992 Erzincan, Turkey earthquake. The comparison of the OpenSees and Matlab solutions are in good agreement in particular for the peak-response values and supports the use of the SDOF idealization introduced in Figure 3.1.

Equally good comparisons are plotted in Figure 3.9 when the inelastic structure coupled with the rocking wall is subjected to the Newhall/360 ground motion recorded during the 1994 Northridge, California earthquake (left plots) and the Takarazuka/000 ground motion recorded during the 1995 Kobe, Japan earthquake.

Earthquake Spectra of a Yielding Oscillator Coupled with a Rocking Wall

Following the verification of the single-degree of freedom idealization by comparing its response with that of the 9-story steel SAC building computed with OpenSees [78], the equations of motion 3.8 and 3.9 are used to generate inelastic response spectra. Figure 3.10 plots displacement spectra of a yielding SDOF oscillator coupled with a vertically prestressed, stepping rocking wall when excited by the Newhall/360 ground motion recorded during the 1994 Northridge, CA earthquake.

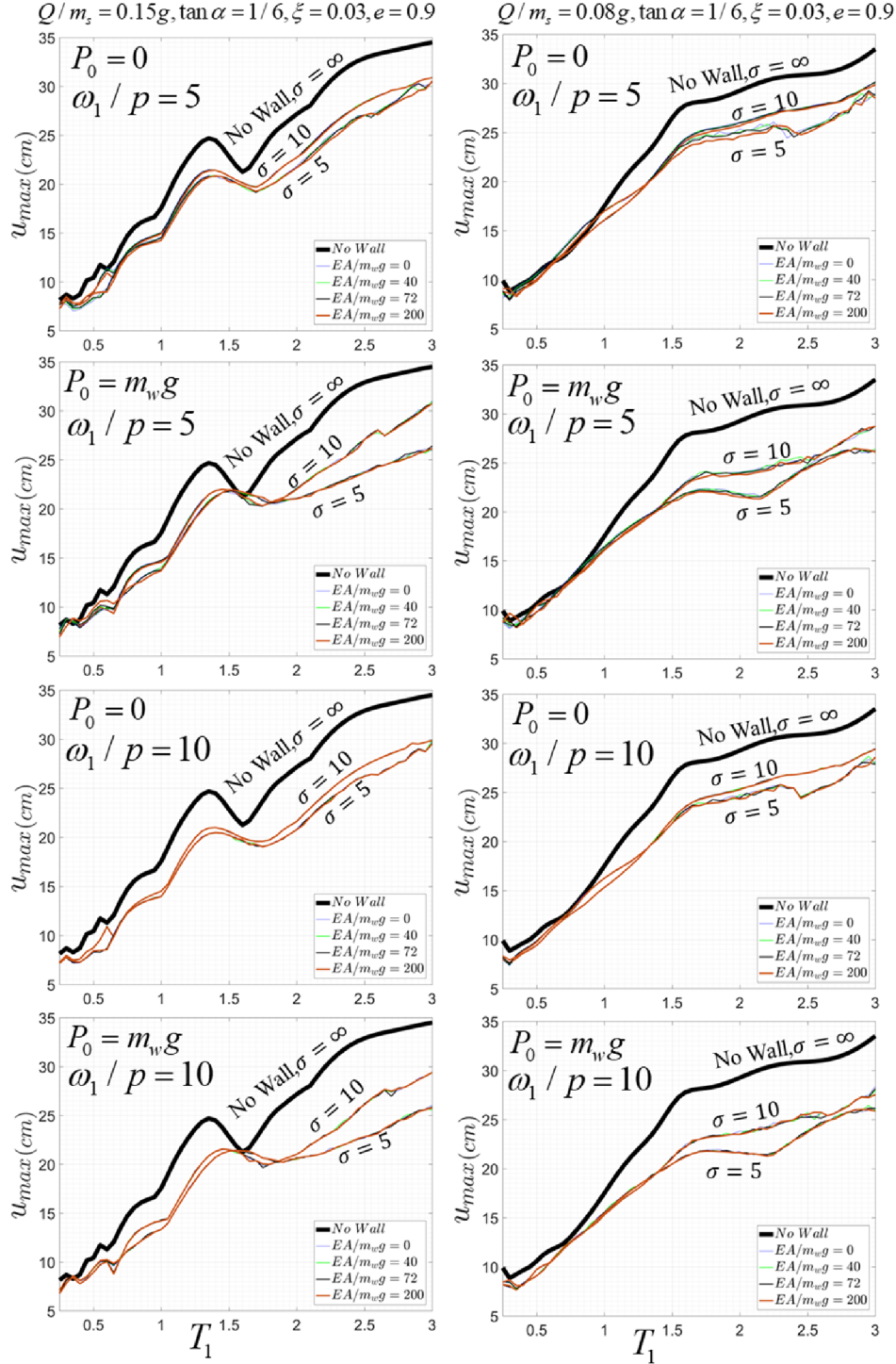


Figure 3.10: Displacement spectra of a yielding SDOF oscillator coupled with a vertically restrained stepping rocking wall with slenderness $\tan \alpha = 1/6$, for two valued of strength, $Q/m_s = 0.15g$ (left column) and $Q/m_s = 0.08g$ (right column) with mass ratios, $\sigma = 5, 10$ and ∞ (no wall); several values of tendon stiffness ($EA/m_w g = 0, 40, 72$ and 200) with ($P_o = m_w g$) and without ($P_o = 0$) pre-tensioning when subjected to the Newhall/360 ground motion recorded during the 1994, Northridge California earthquake.

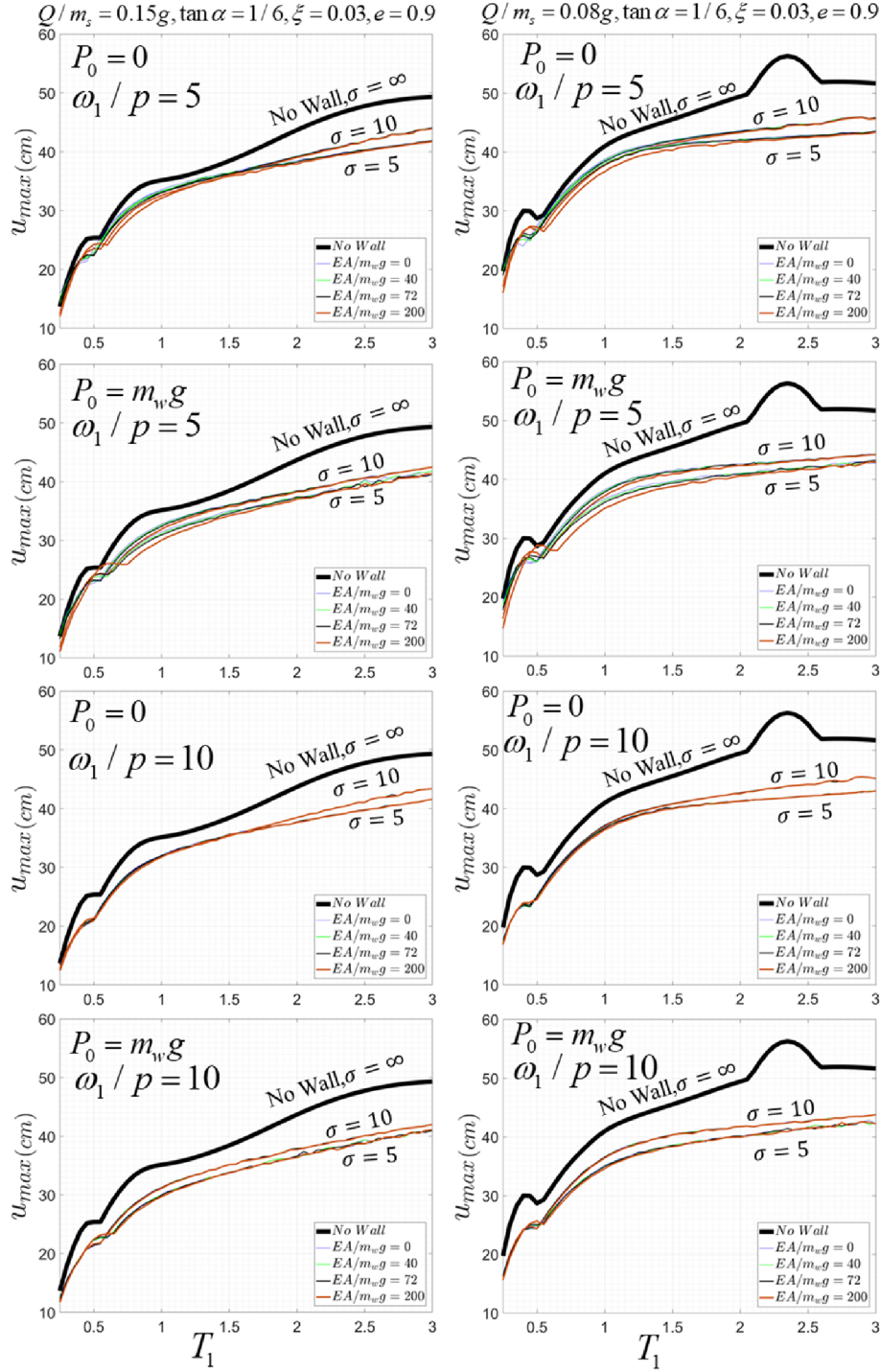


Figure 3.11: Displacement spectra of a yielding SDOF oscillator coupled with a vertically restrained stepping rocking wall with slenderness $\tan \alpha = 1/6$, for two values of strength, $Q/m_s = 0.15g$ (left column) and $Q/m_s = 0.08g$ (right column) with mass ratios, $\sigma = 5, 10$ and ∞ (no wall); several values of tendon stiffness ($EA/m_w g = 0, 40, 72$ and 200) with ($P_0 = m_w g$) and without ($P_0 = 0$) pre-tensioning when subjected to the Pacoima Dam/164 ground motion recorded during the 1971 San Fernando, California earthquake.

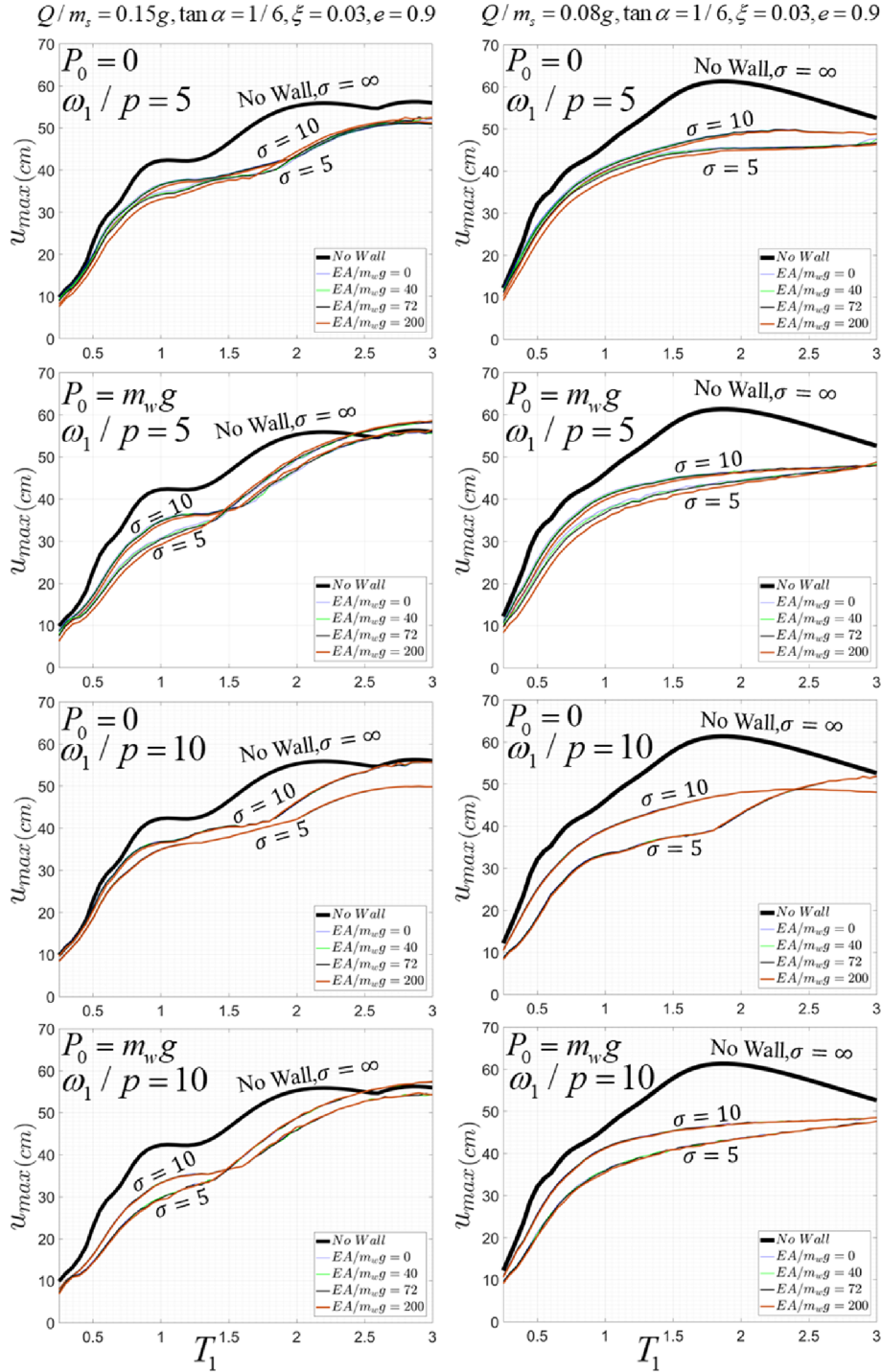


Figure 3.12: Displacement spectra of a yielding SDOF oscillator coupled with a vertically restrained stepping rocking wall with slenderness $\tan \alpha = 1/6$, for two valued of strength, $Q/m_s = 0.15g$ (left column) and $Q/m_s = 0.08g$ (right column) with mass ratios, $\sigma = 5, 10$ and ∞ (no wall); several values of tendon stiffness ($EA/m_w g = 0, 40, 72$ and 200) with ($P_o = m_w g$) and without ($P_o = 0$) pre-tensioning when subjected to the Erzincan NS ground motion recorded during the 1992 Erzincan, Turkey earthquake.

The left plots are for a structure with a yielding strength $Q/m_s = 0.15g$; whereas, the right plots are for a weaker structure, $Q/m_s = 0.08g$. The first and most important observation is that the effect of vertical tendons even when they are stiff ($EA/(m_w g) = 200$) and highly prestressed ($p_o = m_w g$) is marginal. In contrast, the weight of the rocking wall has more noticeable effects with the heavier wall ($\sigma = 5$) being more effective in some regions of the spectra. The same conclusions are drawn from the inelastic spectra presented in Figure 3.11 and 3.12 where the inelastic structure-rocking wall system is excited by the Pacoima Dam/164 ground motion recorded during the 1971 San Fernando, California earthquake and the Erzincan NS ground motion recorded during the 1992 Erzincan, Turkey earthquake.

Conclusion

In this chapter the dynamic response of a yielding SDOF oscillator coupled with a vertically restrained, stepping rocking wall is investigated. The full nonlinear equations of motion were derived, and the dependability of the one-degree-of-freedom idealization is validated against the nonlinear time-history response analysis of the 9-story SAC steel building. The equations of motion of the SDOF idealization show explicitly that the contribution of vertical tendons, even when they are stiff, is two orders of magnitude less than the inertia forces on the moment frame-rocking wall system. This chapter offers a comprehensive parametric analysis which reaches the following conclusions:

- The participation of the stepping rocking wall suppresses peak inelastic displacements with the heavier wall being in most cases more effective. In contrast, the effect of the vertical tendons even when they are stiff ($\frac{EA}{m_w g} = 200$) and highly prestressed ($P_o = m_w g$) is marginal. Given that the vertical tendons increase the vertical reactions at the pivoting corners by more than 50%, the study concludes that for medium- to high-rise buildings, vertical tendons in

rocking walls are not recommended.

- The SDOF idealization presented in this study compares satisfactory with finite-element analysis of a 9-story steel SAC building coupled with a stepping rocking wall; therefore, the SDOF idealization can be used with confidence for preliminary analysis and design.

CHAPTER 4: YIELDING STRUCTURES COUPLED WITH DAMPED ROCKING WALLS

Introduction

The concept of coupling the lateral response of a moment resisting frame with a rigid core system goes back to the early work of Paulay [87] and Fintel [88]. With this design, interstory drift demands are reduced at the response of transferring appreciable shear-forces and bending moments at the foundation of the rigid core wall.

About the same time, the early concepts of the alternative strategy for seismic protection by modifying the response of a structure with specially designed supplemental devices were brought forward in the seminal papers by Kelly et al. [89].

Clearly, the 1972 paper by Kelly et al. [89] marks the beginning of the use of response modification devices for the seismic protection of structures and among several original contributions it suggests the use of rocking shear-walls in association with energy dissipation devices for the seismic protection of moment-resisting frames (Figure 2 of the paper by Kelly et al. [89] that is reproduced in this chapter as Figure 4.1 (a)). In this way, the stepping core wall does not suffer from large ductility demands and possible cyclic degradation while recentering happens invariably due to gravity. Despite its remarkable originality and technical merit, the paper by Kelly et al. 1972 did not receive the attention it deserved and it was some two decades later that the PRESSS Program [7, 8] reintroduced the concept of uplifting and rocking of the joint shear wall system [9, 10].

Following the PRESSS program a number of publications presented experimental and analytical studies on the cyclic loading of structural systems coupled with vertically restrained rocking walls [11, 12]. Given that damping during impact as the wall alternate pivot points is low ([27, 90, 91]

(a)

Stepping Rocking Wall

$2h$

$2b$



These subsequent studies were partly motivated from the need to eliminate the generation of a weak-story failure in multi-story buildings together with the need to ensure recentering of the yielding frame [17, 18, 22]. At the same time alternative proposals on the use of pinned rocking walls [19, 20, 23], where the weight of the wall works against the stability of the structure motivated a series of recent studies that revisited the dynamics of a moment-resisting frame coupled with a rocking wall either stepping or pinned [46, 47, 49] by accounting explicitly of the role of the rotational inertia of the rocking wall. These studies led to valuable conclusions, including that the vertical tendons in tall, stiff, stepping rocking walls have marginal contribution even when they offer a high axial stiffness [49].

In view of these recent findings, this chapter examines the contribution of viscous and hysteretic dampers to the response of a yielding frame coupled with a rocking wall shown in Figure 4.1.

Dynamics of a Yielding Oscillator Coupled with a Stepping Rocking Wall with Supplemental Damping

With reference to Figure 4.1(b), this study examines the dynamic response of a yielding single-degree-of-freedom (SDOF) structure, with mass, m_s , pre-yielding stiffness, k_1 , post-yielding stiffness, k_2 and strength, Q , that is coupled with a free-standing stepping rocking wall of size, $R = \sqrt{b^2 + h^2}$, slenderness, $\tan \alpha = b/h$, mass m_w and moment of inertia about the pivoting (stepping) points O and O' , $I = \frac{4}{3}m_w R^2$. Vertical energy dissipation devices are mounted to the rocking wall at a distance, d , from the pivoting points of the wall as shown in Figures 4.1(b) and 4.2 In the interest of simplicity, it is assumed that the arm with length L , that couples the motion is articulated at the center mass of the rocking wall at a height, h from its foundation as shown in Figure 4.1(a).

Kinematics of the Structural System

During rocking motion of the wall, the upward displacement; v_1 of the damper appended at the side of the wall across the pivoting point is

$$v_1 = S_1 [\sin(\phi_1 \pm \theta) - \sin \phi_1] \quad (4.1)$$

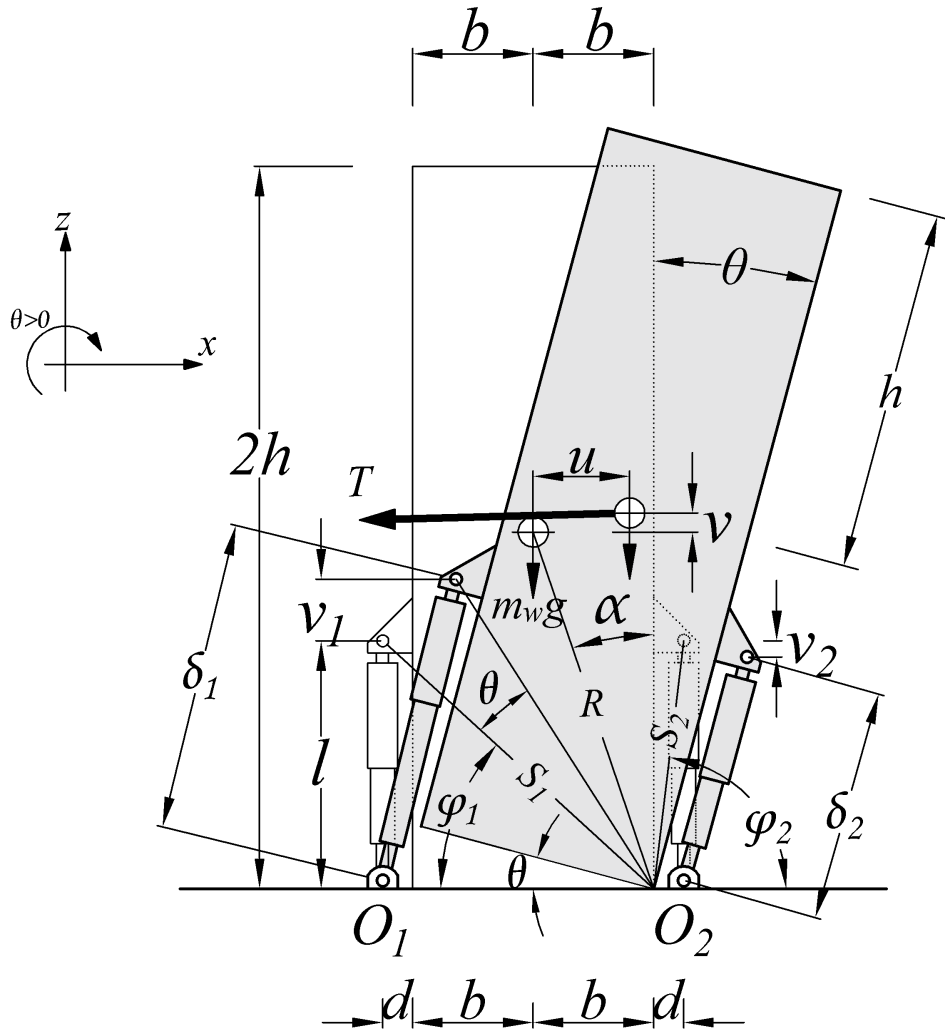


Figure 4.2: Geometric quantities pertinent to the dynamic analysis of a rocking wall with additional energy dissipators.

whereas the downward displacement; v_2 of the damper appended at the side of the wall that is

stepping on the pivoting point is

$$v_2 = S_2[\sin \phi_2 - \sin(\phi_2 \mp \theta)] \quad (4.2)$$

where $S_1 = \sqrt{(2b+d)^2 + l^2}$, $S_2 = \sqrt{d^2 + l^2}$, $\sin \phi_1 = l/S_1$ and $\sin \phi_2 = l/S_2$.

The elongation of damper, e_1 appended at the side of the column across the pivoting point is:

$e_1 = \delta_1 - l$, where δ_1 is offered by the cosine rule:

$$\delta_1 = S_1 \sqrt{1 + \cos^2 \varphi_1 - 2 \cos \varphi_1 \cos(\varphi_1 \pm \theta)} \quad (4.3)$$

and by using that $e_1 = \delta_1 - l$, the elongation of the damper is

$$e_1(t) = S_1 \left[\sqrt{1 + \cos^2 \varphi_1 - 2 \cos \varphi_1 \cos(\varphi_1 \pm \theta)} - \sin \varphi_1 \right] \quad (4.4)$$

The time derivative of the elongation $e_1(t)$ is expressed in terms of the independent variable θ and its time derivative, $\dot{\theta}$:

$$\dot{e}_1(t) = \frac{S_1 \cos \varphi_1 \dot{\theta} \sin(\varphi_1 \pm \theta)}{\sqrt{1 + \cos^2 \varphi_1 - 2 \cos \varphi_1 \cos(\varphi_1 \pm \theta)}} \quad (4.5)$$

Similarly, the contraction of the dampers appended at the side of the column that is stepping on the pivoting point is $e_2 = l - \delta_2$, where δ_2 is

$$\delta_2 = S_2 \sqrt{1 + \cos^2 \varphi_2 - 2 \cos \varphi_2 \cos(\varphi_2 \mp \theta)} \quad (4.6)$$

and by using that $e_2 = l - \delta_2$, the contraction of the damper is

$$e_2(t) = S_2 \left[\sin \varphi_2 - \sqrt{1 + \cos^2 \varphi_2 - 2 \cos \varphi_2 \cos(\varphi_2 \mp \theta)} \right] \quad (4.7)$$

The time derivative of the contraction $e_2(t)$ is expressed in terms of the independent variable θ and its time derivative, $\dot{\theta}$

$$\dot{e}_2(t) = \frac{S_2 \cos \varphi_2 \dot{\theta} \sin(\varphi_2 \mp \theta)}{\sqrt{1 + \cos^2 \varphi_2 - 2 \cos \varphi_2 \cos(\varphi_2 \mp \theta)}} \quad (4.8)$$

Constitutive Laws of Non-Linear Viscous and Hysteretic Dissipation Devices

The energy dissipation devices appended to the rocking wall as shown in Figure 4.2 can be either linear or nonlinear fluid dampers [92–94] or hysteretic (yielding) dampers such as buckling restrained braces [95–98].

$$F_d = C_q |\dot{e}(t)|^q \text{sgn}[\dot{e}(t)] \quad (4.9)$$

where $0 < q \leq 1$ is the exponent of the damper, C_q is the damping constant with units: $[m][L]^{1-q}[T]^{q-2}$, and $\text{sgn}[\]$ is the signum function. $e(t)$ is the stroke of the damper that is given by equation (4.4) when the damper is in elongation ($e(t) = e_1(t)$) and by equation (4.7) when the damper is in contraction ($e(t) = e_2(t)$). When $q = 1$, equation (4.9) reduces to a linear viscous law: $F_d = c_1 \dot{e}(t)$.

When torsionally yielding steel-beam dampers, buckling restrained braces (BRB) or other yielding devices are used, their constitutive law can be expressed by the Bouc-Wen model [52, 57, 59]

$$F_d = ak_d e(t) + (1 - a)k_d u_y z(t) \quad (4.10)$$

in which, k_d is the preyielding stiffness of the device, u_y is the yield displacement, a is the post-to-pre-yielding stiffness ratio and $-1 \leq z(t) \leq 1$ is the dimensionless internal variable described by

$$\dot{z}(t) = \frac{1}{u_y} \left[\dot{e}(t) - \beta \dot{e}(t) |z(t)|^n - \gamma |\dot{e}(t)| z(t) |z(t)|^{n-1} \right] \quad (4.11)$$

Again, $e(t)$ is the stroke of the hysteretic device that is given by equation (4.4) when the damper is in elongation ($e(t) = e_1(t)$) and by equation (4.7) when the damper is in contraction ($e(t) = e_2(t)$). In equation (4.11), constants β , γ and n are model parameters to be discussed later in the chapter.

Equation of Motion of the Entire System

With reference to Figure 4.1(b) dynamic equilibrium of the mass m_s gives:

$$m_s(\ddot{u} + \ddot{u}_g) = -F_s - c\dot{u} + T \quad (4.12)$$

where F_s is the force the develops in the nonlinear spring and is described by the Bouc-Wen model [52, 57, 59].

$$F_s(t) = ak_1u(t) + (1 - a)k_1u_yz(t) \quad (4.13)$$

in which, $a = k_2/k_1$ is the post-to-pre- yielding stiffness ration of the nonlinear oscillator and $-1 \leq z(t) \leq 1$ is a dimensionless internal variable described similarly with equation (2.7) but with constants β , γ and n defined based on oscillator hysteretic behavior.

Case I. $\theta > 0$:

For positive rotations ($\theta > 0$), dynamic equilibrium of the rotating wall with mass, m_w , equipped with vertical dampers installed on each of its side as shown in Figures 4.1(b) and 4.2 gives

$$I\ddot{\theta} = -TR\cos(\alpha - \theta) - m_w g R \sin(\alpha - \theta) - m_w \ddot{u}_g R \cos(\alpha - \theta) - F_{d1}r_1 - F_{d2}r_2 \quad (4.14)$$

in which F_{d1} and F_{d2} are the damping forces in the damper across the pivoting point and the damper at the pivoting point side respectively and r_1 and r_2 are moment arms of the dampers about pivoting

point

$$r_1 = S_1 \cos \varphi_1 \frac{\sin(\varphi_1 \pm \theta)}{\sqrt{1 + \cos^2 \varphi_1 - 2 \cos \varphi_1 \cos(\varphi_1 \pm \theta)}} \quad (4.15)$$

$$r_2 = S_2 \cos \varphi_2 \frac{\sin(\varphi_2 \mp \theta)}{\sqrt{1 + \cos^2 \varphi_2 - 2 \cos \varphi_2 \cos(\varphi_2 \mp \theta)}} \quad (4.16)$$

Figure 4.3 shows how lever-arm r_1 and r_2 depend on the rotation, θ of the rocking column. In the entire analysis, subscript 1 is for the damper across the pivoting point and subscript 2 is for the damper next to the pivoting point.

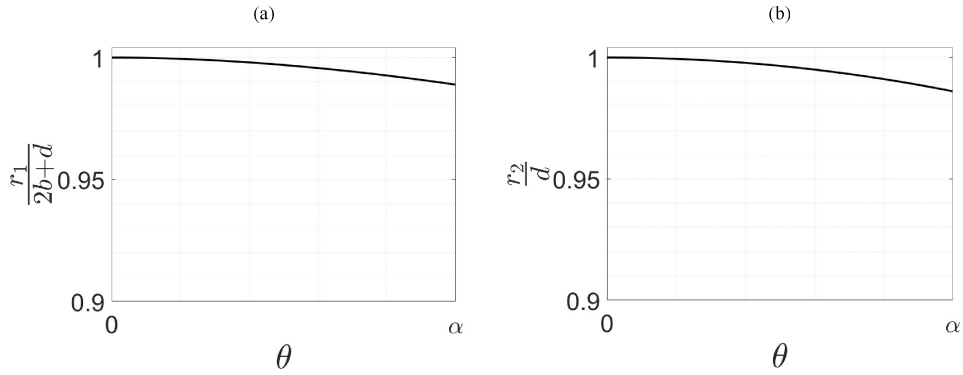


Figure 4.3: Reduction of the lever arm r_1 of the damping force across the pivoting point (a) and lever arm of the damping force next to the pivoting point (b) as a function the column rotation θ .

The axial force T appearing in equation 4.12 is replaced with the help of equations (4.13) and (2.7), whereas for a rectangular stepping wall, $I = 4/3 m_w R^2$. Accordingly, equation (4.14) assumes the form:

$$\begin{aligned} & \frac{4}{3} m_w R^2 \ddot{\theta} + [m_s(\ddot{u} + \ddot{u}_g) + a k_1 u(t) + (1-a) k_1 u_y z(t) + c \dot{u}] R \cos(\alpha - \theta) \\ & = -m_w R [\ddot{u}_g \cos(\alpha - \theta) + g \sin(\alpha - \theta)] - F_{d1} r_1 - F_{d2} r_2 \end{aligned} \quad (4.17)$$

upon dividing with $m_w R$ equation (4.17) gives:

$$\begin{aligned} & \frac{4}{3} R \ddot{\theta} + \left[\sigma(\ddot{u} + \ddot{u}_g) + a \frac{k_1}{m_w} u(t) + (1-a) \frac{k_1}{m_w} u_y z(t) + \frac{c}{m_w} \dot{u} \right] \cos(\alpha - \theta) \\ & = -[\ddot{u}_g \cos(\alpha - \theta) + g \sin(\alpha - \theta)] - \frac{F_{d1} r_1}{m_w R} - \frac{F_{d2} r_2}{m_w R} \end{aligned} \quad (4.18)$$

in which $\sigma = m_s/m_w$ is the mass ratio parameter.

Substitution of the expressions of the relative displacement, velocity and acceleration given by equations (2.2) to (2.4) for positive rotations, and after dividing with R equation (4.18) is expressed only in terms of the variable, $\theta(t)$.

$$\begin{aligned} & \left(\frac{4}{3} + \sigma \cos^2(\alpha - \theta)\right) \ddot{\theta} + \sigma \cos(\alpha - \theta) \left[a \omega_1^2 (\sin \alpha - \sin(\alpha - \theta)) + 2\xi \omega_1 \dot{\theta} \cos(\alpha - \theta) \right. \\ & \left. + \dot{\theta}^2 \sin(\alpha - \theta) + (1 - a) \omega_1^2 \frac{u_y}{R} z(t) \right] \\ & = -\frac{g}{R} \left[(\sigma + 1) \frac{\ddot{u}_g}{g} \cos(\alpha - \theta) + \sin(\alpha - \theta) + \frac{F_{d1}}{m_w g} \frac{r_1}{R} + \frac{F_{d2}}{m_w g} \frac{r_2}{R} \right] \end{aligned} \quad (4.19)$$

Case 2. $\theta < 0$:

For negative rotations one can follow the same reasoning and the equation of the coupled system is:

$$\begin{aligned} & \left(\frac{4}{3} + \sigma \cos^2(\alpha + \theta)\right) \ddot{\theta} - \sigma \cos(\alpha + \theta) \left[a \omega_1^2 (\sin \alpha - \sin(\alpha + \theta)) - 2\xi \omega_1 \dot{\theta} \cos(\alpha + \theta) \right. \\ & \left. + \dot{\theta}^2 \sin(\alpha + \theta) - (1 - a) \omega_1^2 \frac{u_y}{R} z(t) \right] \\ & = -\frac{g}{R} \left[(\sigma + 1) \frac{\ddot{u}_g}{g} \cos(\alpha + \theta) - \sin(\alpha + \theta) + \frac{F_{d1}}{m_w g} \frac{r_1}{R} + \frac{F_{d2}}{m_w g} \frac{r_2}{R} \right] \end{aligned} \quad (4.20)$$

Parameters of the Problem

The Bouc-Wen model described by equations (2.6) and (2.7) is a phenomenological model of hysteresis originally proposed by Bouc 1967 [57] and subsequently generalized by Wen [52, 58] and Baber and Wen [59]. It is a versatile model that can capture various details of the nonlinear force-displacement loop. Subsequent studies on the modeling of yielding systems by Constantinou and Adnane [60] concluded that when certain constraints are imposed on the parameters β and γ ($\beta + \gamma = 1$), the model reduces to a viscoplastic element with well-defined physical characteristics. The Bouc-Wen model essentially builds on the bilinear idealization shown in the bottom-left of Figure 2.1.

For the five-parameter system shown with the bilinear idealization. (k_1 = pre-yielding stiffness, k_2 = post-yielding stiffness, u_y = yield displacement, Q = strength and F_y = yielding force), only three parameters are needed to fully describe the bilinear behavior (see for instance [61]). In this work, the authors select the pre-yielding stiffness $k_1 = m_s \omega_1^2$, the post-yielding stiffness $k_2 = a k_1$ and the strength of the structure Q . With reference to Figure 2.1 (bottom-left), $F_y = k_1 u_y = Q + k_2 u_y$. Accordingly, $u_y = Q/(k_1 - k_2)$ and $F_y = k_1 Q/(k_1 - k_2)$. The parameters β , γ and n appearing in equation 3.7 are established from past studies on the parameter identification of yielding concrete structures and assume the values: $\beta = 0.95$, $\gamma = 0.05$ and $n = 2$ [62, 63]. With the parameters $\beta = 0.95$, $\gamma = 0.05$ and $n = 2$ being established, the peak inelastic displacement, u_{max} of the SDOF system shown in Figures 4.1(b) and 4.2 is a function of the following parameters:

$$u_{max} = f(\omega_1, \frac{Q}{m_s}, a, \xi, p, \tan \alpha, \sigma, g, \frac{F_d}{m_w g}, \frac{r}{R}, \text{parameters of excitation}) \quad (4.21)$$

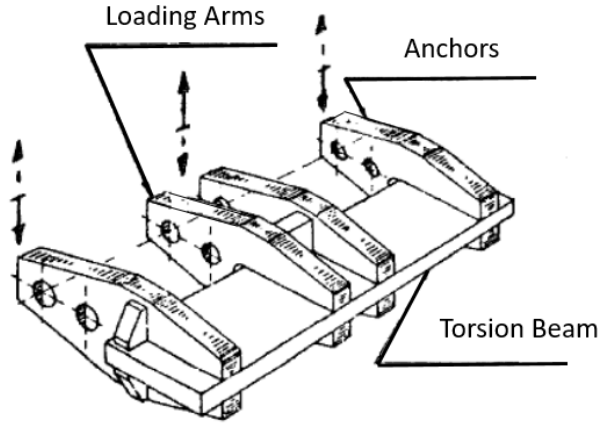


Figure 4.4: Example of torsionally yielding steel-beam damper installed at the base of the stepping pier of the South Rangitikei Rail Bridge in New Zealand which delivers a yield force of $2 \times 45kN$ which is equivalent to $\frac{k_d u_y}{m_w g} = 0.05$.

Here, it is assumed that upon yielding, the structure maintains a mild, positive, post-yielding stiff-

ness = $k_2 = 0.05k_1$, therefore $a = 0.05$ [62, 63]. Furthermore, it is assumed that the pre-yielding damping ratio, $\xi = C/(2m_s\omega_1) = 0.03$ and rocking walls with slenderness, $\tan \alpha = 1/6$.

In this study, torsionally yielding steel-beam damper similar to one that has been used in the stepping pier of the South Rangitikei Rail Bridge in New Zealand is assumed to be used [89, 99–101], hence hysteretic dampers with $\frac{k_d u_y}{m_w g} = 0.05$ is selected.

First, zero-length dampers attached at the pivoting points are considered ($l = \phi_1 = \phi_2 = d = S_2 = 0$ and $S_1 = 2b$); therefore equations (4.4) and (4.15) simplify to

$$e_1 = 2\sqrt{2}b\sqrt{1 - \cos \theta} \quad \text{and} \quad r_1 = \sqrt{2}\frac{b \sin \theta}{\sqrt{1 - \cos \theta}} \quad (4.22)$$

For small rotations $\cos \theta = 1 - \theta^2/2$ and $\sin \theta = \tan \theta = \theta$, therefore, the expressions given by equation 4.22 further simplify to

$$e_1 = 2b \tan \theta \quad \text{and} \quad r_1 = 2b \frac{\sin \theta}{\theta} \approx 2b \quad (4.23)$$

Accordingly, the full nonlinear equation of the stepping pier with zero-length hysteretic dampers at its pivoting points can be found by plugging in values of F_{d_1} from equation (4.11), r_1 from equation (4.22) and $F_{d_2} = r_2 = 0$ into equations (4.19) and (4.20).

In the case when viscous damper is used in the similar location as for the hysteretic dampers, the time derivative of the stroke is

$$\dot{e}_1 = \sqrt{2}b\dot{\theta}\sqrt{1 + \cos \theta} \quad (4.24)$$

which for small rotations simplifies to $\dot{e}_1(t) = 2b\dot{\theta}$.

By comparing, the right hand-side of the equation of motion for each cases of hysteretic and viscous damper, a peak damping force from the viscous dampers $C_q[2b\dot{\theta}_{max}]^q$, will match the yield capacity of the torsionally yielding hysteretic dampers when

$$C_q = \frac{k_d u_y}{(2b\dot{\theta}_{max})^q} \quad (4.25)$$

which for the case of linear viscous damper equation (4.25) simplifies to

$$C = \frac{k_d u_y}{2b\dot{\theta}_{\max}} \quad (4.26)$$

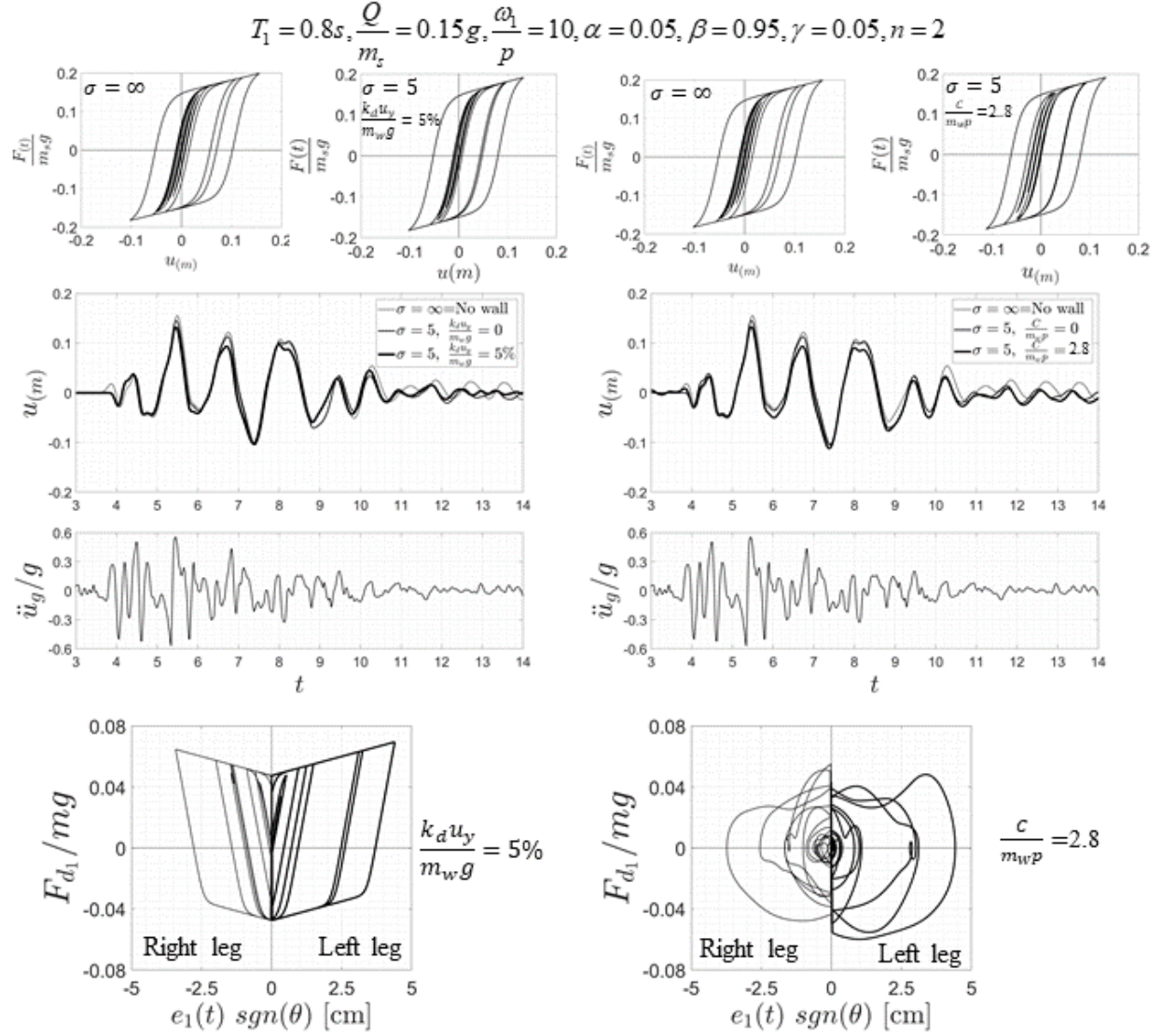


Figure 4.5: Time history analysis of a nonlinear SDOF oscillator coupled with a stepping rocking wall with normalized strength $Q/m_s = 0.15g$, mass ratio, $\sigma = m_s/m_w = 5$, wall size, $\omega_1/p = 10$, and pre-yielding period of $T_1 = 0.8\text{sec}$, when subjected to the Newhall/360 ground motion recorded during the 1994 Northridge, California earthquake. Thin lines: No wall, Heavy solid lines: (thinner) with wall and no dampers (heavier) wall with hysteretic ($k_d u_y/m_w g = 5\%$) (left) and linear viscous ($C/m_w p = 2.8$) (right) zero-length dampers. Bottom: Force-displacement loops of the hysteretic (left) and linear (right) dampers installed at each leg of the rocking wall.

Before proceeding with earthquake response spectra, Figure 4.5 plots force-displacement loops, together with displacement $u(t)$ time histories with a structure having $T_1 = 0.8\text{sec}$, $Q/m_s = 0.15g$ which is coupled with a rocking wall $\omega_1/P = 10$, $\sigma = m_s/m_w = 5$ with supplemental hysteretic dampers (left) and linear viscous dampers (right) when subjected to the Newhall/360 ground motion recorded during 1994 Northridge, California earthquake.

To have comparable damping forces in each case, using equation (4.26) equivalent damping constant calculated for the case $\dot{\theta}_{max} = 0.058\text{ rad/sec}$ which gives $C_1 = 479\text{ Mg/sec}$.

Figure 4.5 in both cases shows that the rocking wall suppress the maximum response and use of dampers plays in favor of reducing the peak displacements. Also yielding oscillator with wall has no residual in contrast with the oscillator with residual of about 2cm .

In Figure 4.5 (bottom) force-deformation relations of hysteretic (left) and viscous (right) is shown. The loops at the bottom show left leg damper (heavier line) when the wall is rotating on right corner and right leg damper when the wall is on left pivoting point. It should be noted that since the dampers are at the pivoting point they will work only when they are appended at the side of the wall across the pivoting point.

Figure 4.6 plots force-displacement loops, together with displacement $u(t)$ time histories with a structure having $T_1 = 0.8\text{sec}$, $Q/m_s = 0.15g$ which is coupled with a rocking wall $\omega_1/P = 10$, $\sigma = m_s/m_w = 5$ with supplemental hysteretic dampers (left) and linear viscous dampers (right) this time with distance of ($d = 0.1h$) when subjected to the Newhall/360 ground motion recorded during 1994 Northridge, California earthquake. In this case both dampers will work and values of e_1 and e_2 should be calculated using equations (4.4) and (4.7).

Figure 4.6 shows that having a bigger lever arm makes the response slightly better. It can also be seen from the force-displacement loops for either viscous or hysteretic dampers that the damper

close to the pivoting point does not generate much damping force since it is not being compressed much and the moment of it will be small since it is close to the pivoting point.

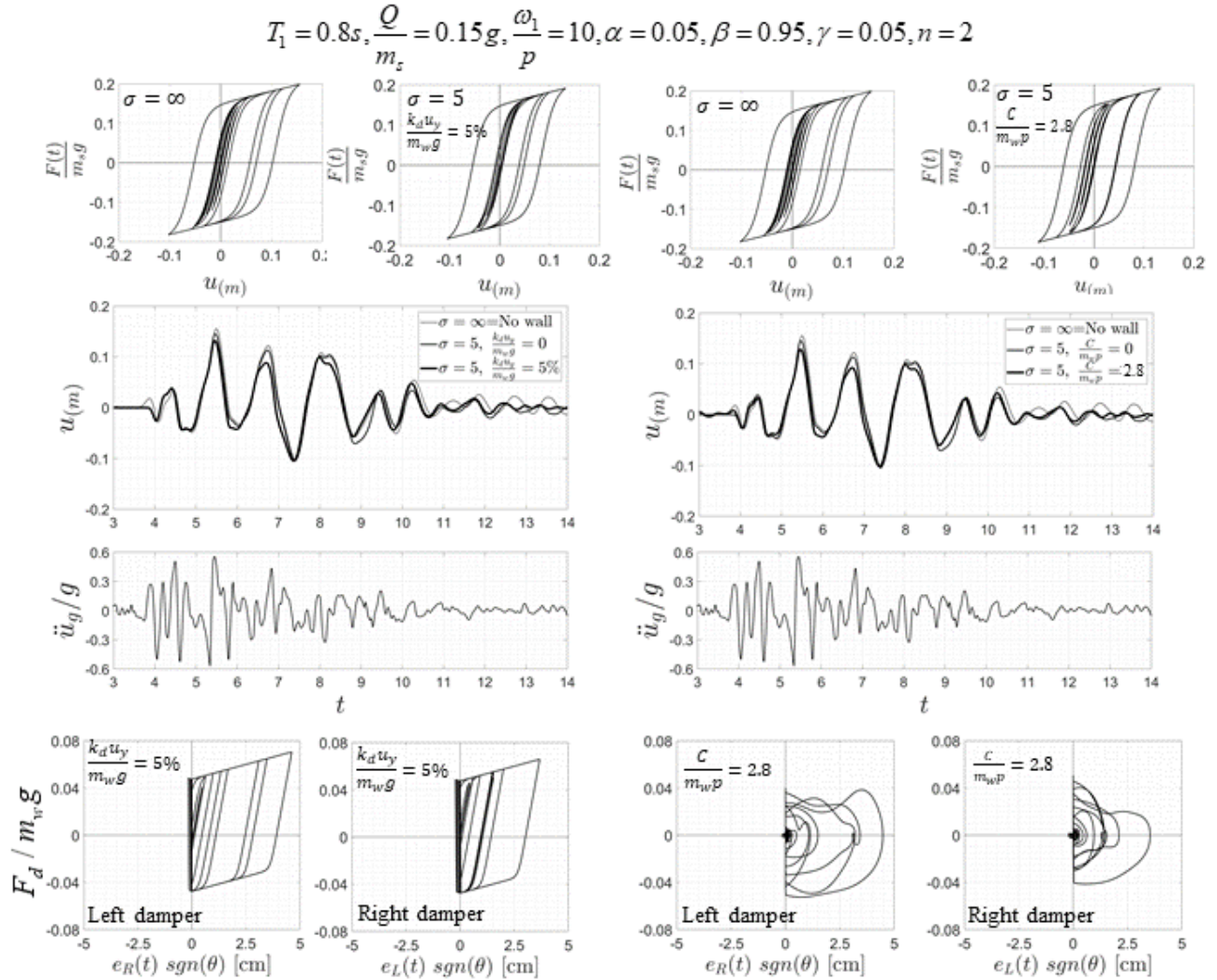


Figure 4.6: Time history analysis of a nonlinear SDOF oscillator coupled with a stepping rocking wall with normalized strength $Q/m_s = 0.15g$, mass ratio, $\sigma = m_s/m_w = 5$, wall size, $\omega_1/p = 10$, and pre-yielding period of $T_1 = 0.8sec$, when subjected to the Newhall/360 ground motion recorded during the 1994 Northridge, California earthquake. Thin lines: No wall, Heavy solid lines: (thinner) with wall and no dampers (heavier) wall with hysteretic ($k_d u_y/m_w g = 5\%$) (left) and linear viscous ($C/m_w p = 2.8$) (right) dampers located at $d = 0.1b$ and $L = 0.2h$. Bottom: Force-displacement loops of the hysteretic (left) and linear (right) dampers installed at each leg of the rocking wall.

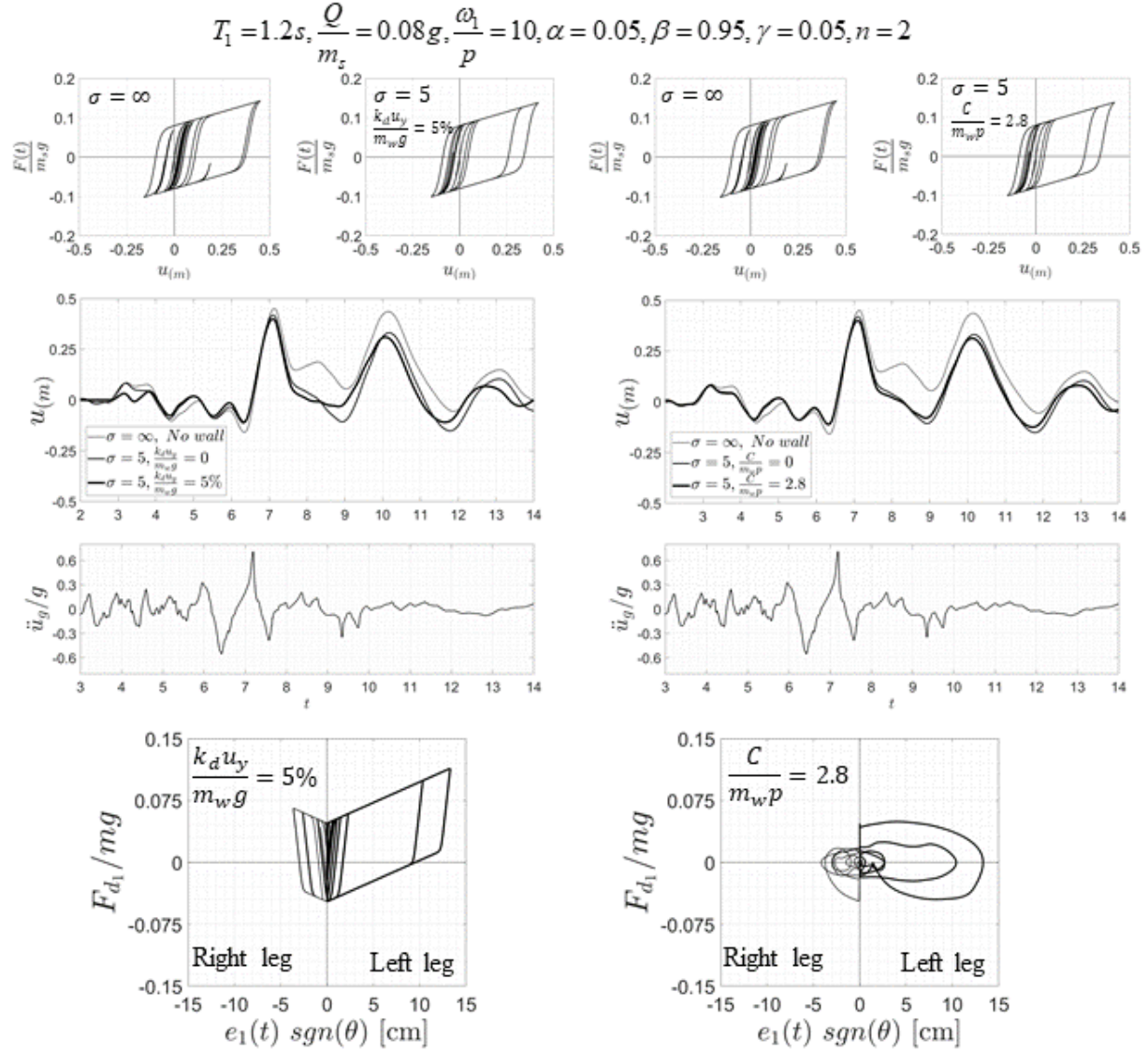


Figure 4.7: Time history analysis of a nonlinear SDOF oscillator coupled with a stepping rocking wall with normalized strength $Q/m_s = 0.08g$, mass ratio, $\sigma = m_s/m_w = 5$, wall size, $\omega_1/p = 10$, and pre-yielding period of $T_1 = 1.2sec$, when subjected to the REHS ground motion recorded during the 2011 Christchurch, New Zealand earthquake. Thin lines: No wall, Heavy solid lines: (thinner) with wall and no dampers (heavier) wall with hysteretic ($k_d u_y/m_w g = 5\%$) (left) and linear viscous ($C/m_w p = 2.8$) (right) zero-length dampers. Bottom: Force-displacement loops of the hysteretic (left) and linear (right) dampers installed at each leg of the rocking wall.

Figure 4.7 plots force-displacement loops, together with displacement $u(t)$ time histories with a structure having $T_1 = 1.2sec$, $Q/m_s = 0.08g$ which is coupled with a rocking wall $\omega_1/P = 10$,

$\sigma = m_s/m_w = 5$ with supplemental hysteretic dampers (left) and linear viscous dampers (right) when subjected to the REHS ground motion recorded during 2011 Christchurch, New Zealand earthquake. Similar to the results presented in Figures 4.5 and 4.6 Figure 4.7 shows that the damped system has smaller maximum deformation and the coupled system has minimal residual deformation. In this case since maximum velocity is $\dot{\theta}_{max} = 0.038$ damping constant is calculated from equation 4.26, which is equal to $C_1 = 1700 \text{ Mg/sec}$.

Earthquake Spectra of a Yielding Oscillator Coupled with a Stepping Rocking Wall with Supplemental Damping

In this section, equations of motion (4.19) and (4.20) are used to generate inelastic response spectra. Figures 4.8 and 4.9 plot displacement spectra of a yielding SDOF oscillator coupled with a stepping rocking wall with supplemental zero-length linear ($q = 1$) viscous and hysteretic dampers when excited by the earthquakes introduced previously in the study and labeled each accordingly.

First observation is that use of dampers are effective way of reducing maximum deformation in the coupled system and more damping leads to smaller deformations. Also, in some cases like in the case of hysteretic damper under 2011 REHS, Christchurch, New Zealand ground motion, damped system maximum response exceeds the undamped yielding oscillator coupled with stepping wall system, which shows that the effectiveness of hysteretic supplemental damping in suppressing the rocking response depends strongly on the kinematic characteristics of the ground motion. Whenever the damped response exceeds that undamped response, the exceedance is marginal and in most cases the damped response is lower than the undamped response.

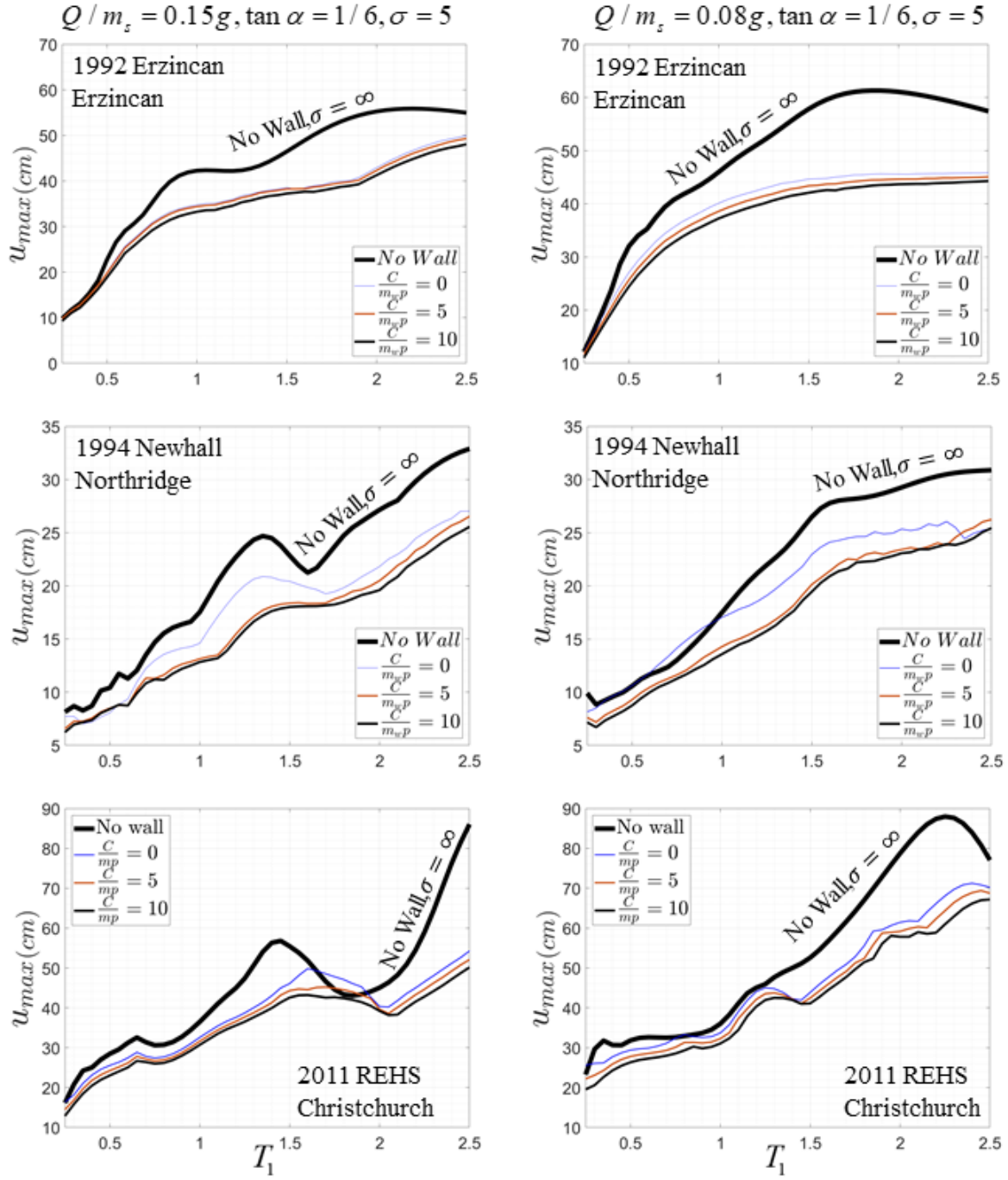


Figure 4.8: Peak response of SDOF yielding oscillator coupled with a stepping wall with slenderness $\tan \alpha = 1/6$ with zero-length supplemental viscous dampers ($q=1$) appended at the pivoting points ($d=0$) when excited by the three strong ground motions presented earlier in this study. Figures on the left are corresponding to stronger oscillator with strength of $Q/m_s = 0.15g$ and on the right with an oscillator with strength of $Q/m_s = 0.08g$.

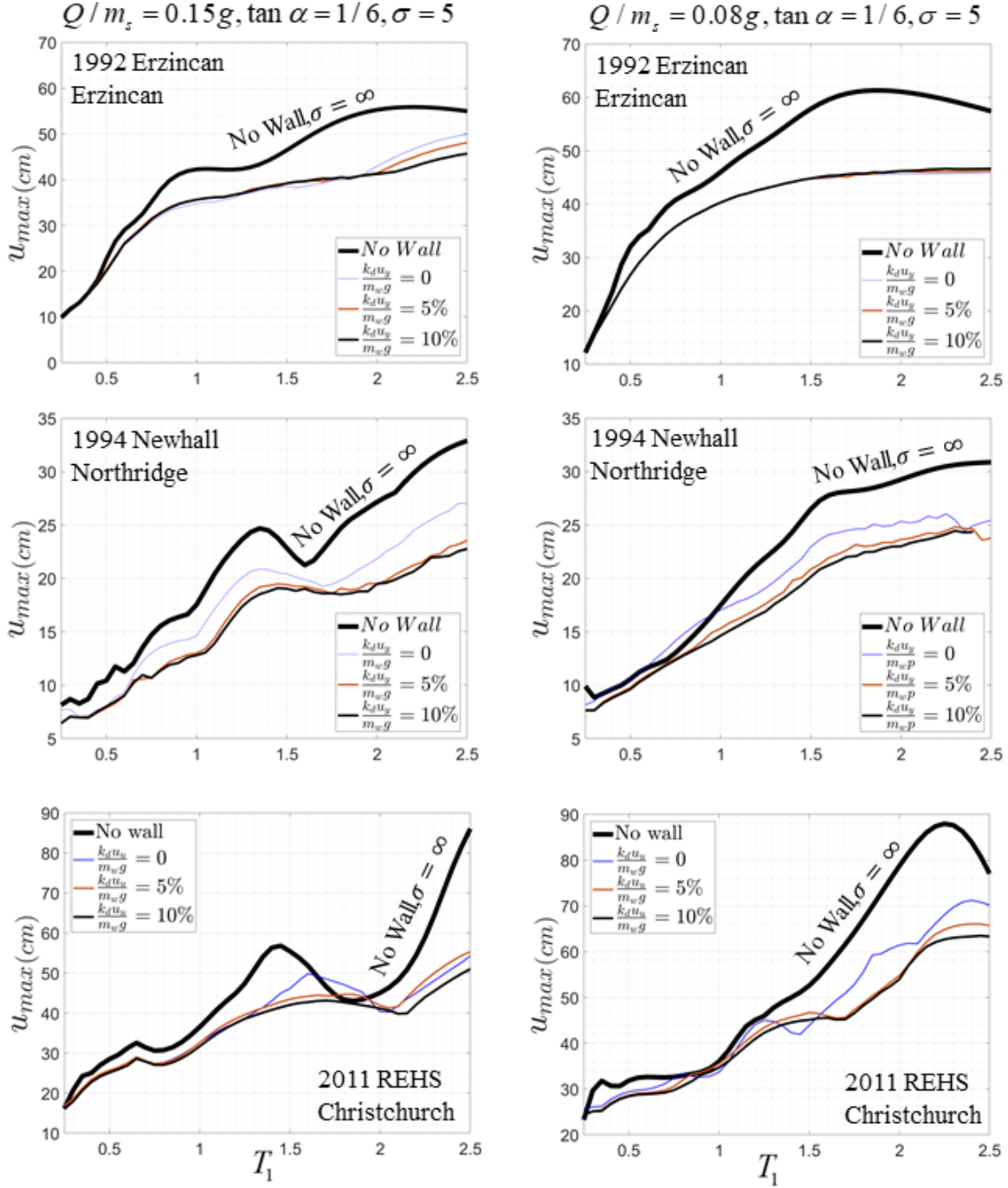


Figure 4.9: Peak response of SDOF yielding oscillator coupled with a stepping wall with slenderness $\tan \alpha = 1/6$ with zero-length supplemental hysteretic dampers appended at the pivoting points ($d=0$) when excited by the three strong ground motions presented earlier in this study. Figures on the left are corresponding to stronger oscillator with strength of $Q/m_s = 0.15g$ and on the right with an oscillator with strength of $Q/m_s = 0.08g$.

There are several situations where it is suitable to place the supplemental energy dissipation devices along the sides of rocking columns or a rocking walls [89, 99] as it is shown in Figure 4.2. In this case two additional parameters appear in the analysis, the distance d of the connection of the dissipation device from the pivoting point and the length, l of the dissipation device.

Figure 4.10 plots maximum response diagrams for yielding oscillator coupled with rocking wall with slenderness $\tan \alpha = 1/6$ with finite-length supplemental viscous damper with $l/h = 0.2$ and $d/b = 0.1$ and normalized damping constant $\frac{C}{m_w p} = 5$ and 10; while Figure 4.11 plots maximum response diagram for yielding oscillator coupled with rocking wall with finite length supplemental hysteretic dampers (say buckling-restrained braces) with $l/h = 0.2$ and $d/b = 0.1$ and normalized yield-strength $\frac{k_d u_y}{m_w g} = 5\%$ and 10%.

In Figures 4.10 and 4.11 similar trends as those discussed for the corresponding Figures 4.8 and 4.9 are observed; while the additional lever arm $d = 0.1b$ appears to have marginal effect on the peak response in particular for taller columns.

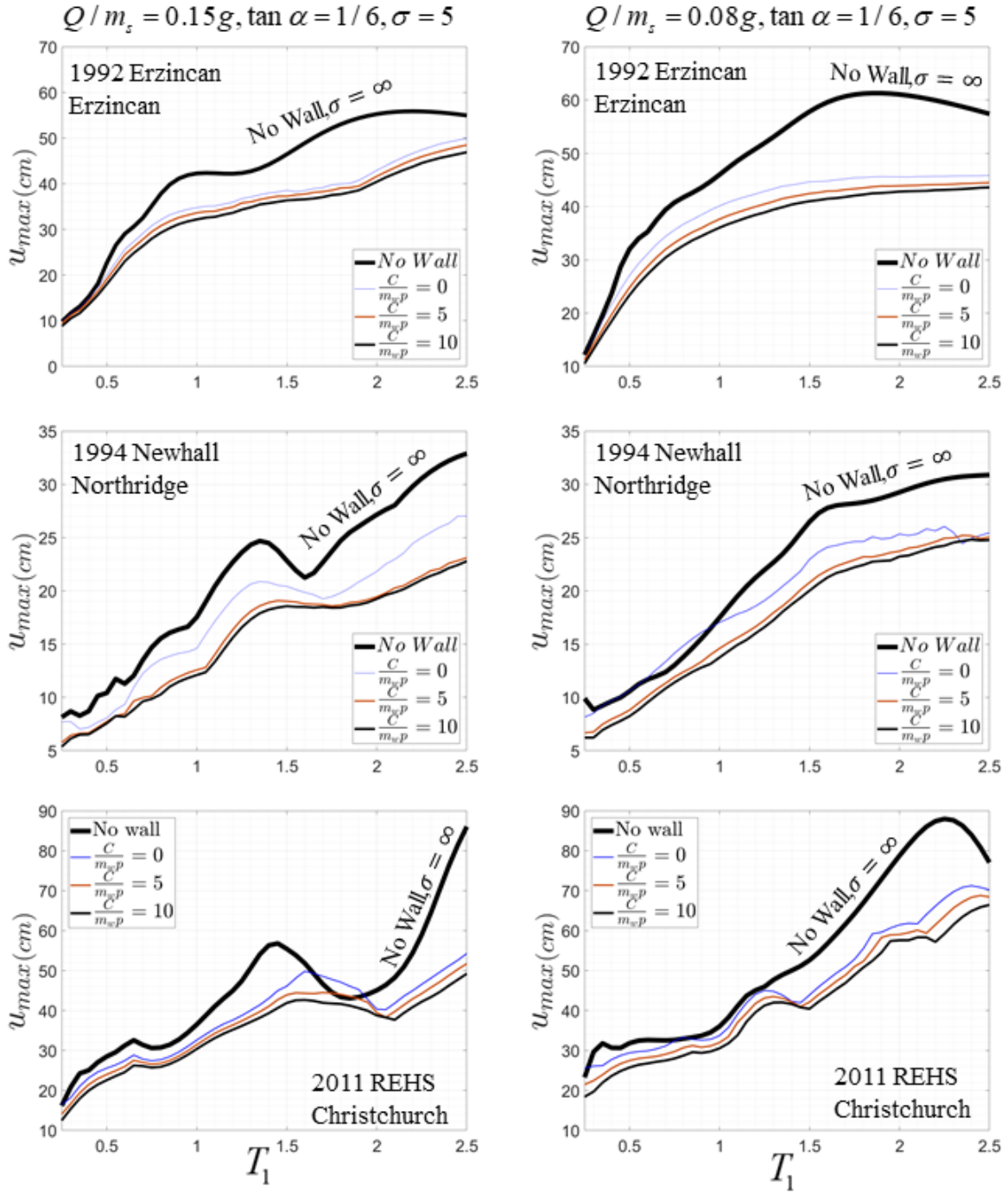


Figure 4.10: Peak response of SDOF yielding oscillator coupled with a stepping wall with slenderness $\tan \alpha = 1/6$ with supplemental viscous dampers ($q=1$) with length of ($l = 0.2h$) installed along the sides of the rocking wall at the distance ($d = 0.1b$) when excited by the three strong ground motions presented earlier in this study. Figures on the left are corresponding to stronger oscillator with strength of $Q/m_s = 0.15g$ and on the right with an oscillator with strength of $Q/m_s = 0.08g$.

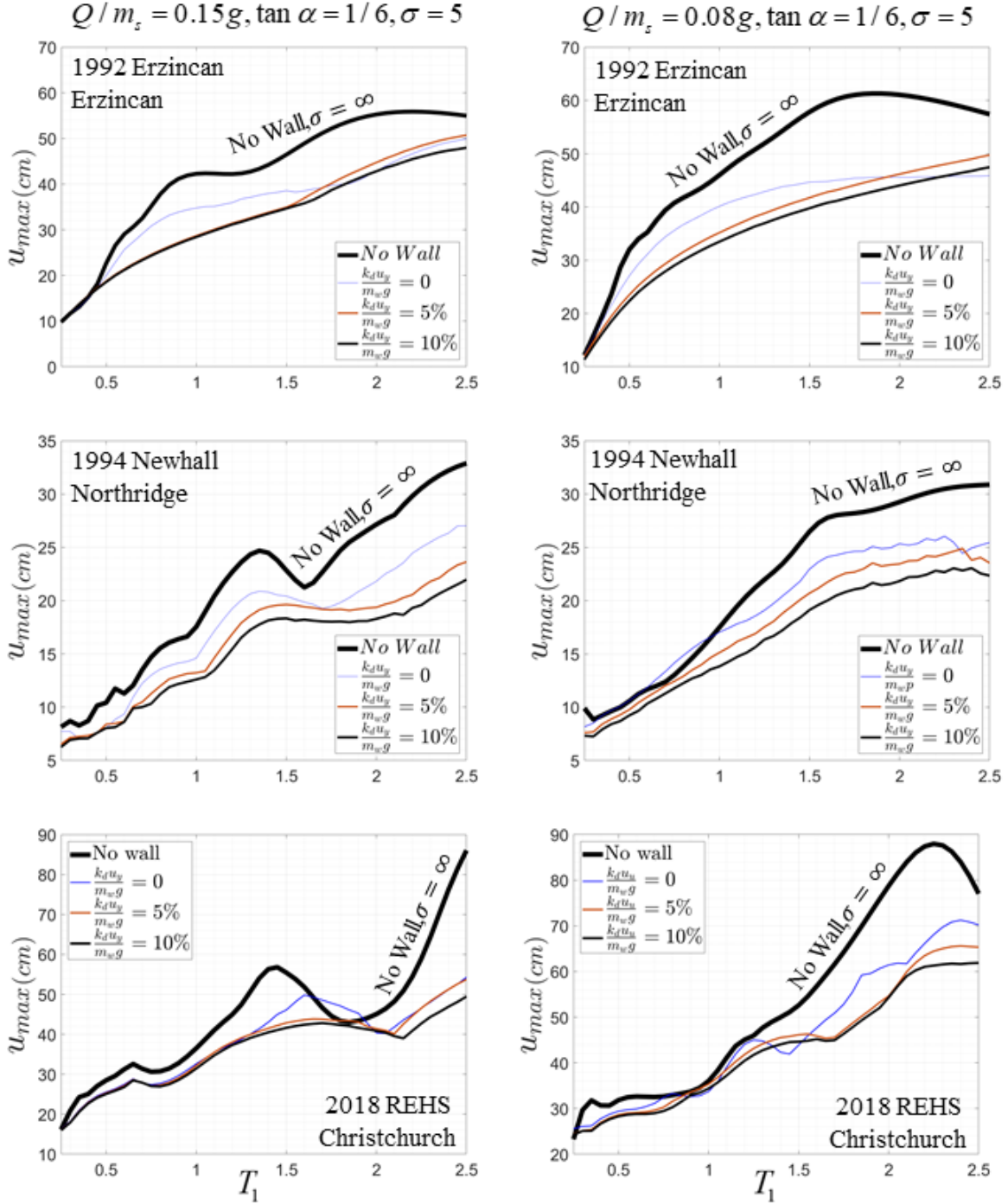


Figure 4.11: Peak response of SDOF yielding oscillator coupled with a stepping wall with slenderness $\tan \alpha = 1/6$ with supplemental hysteretic dampers with length of ($l = 0.2h$) installed along the sides of the rocking wall at the distance ($d = 0.1b$) when excited by the three strong ground motions presented earlier in this study. Figures on the left are corresponding to stronger oscillator with strength of $Q/m_s = 0.15g$ and on the right with an oscillator with strength of $Q/m_s = 0.08g$.

Difference between Viscous and Hysteretic Dampers Behavior

In equations (4.19) and (4.20) parameters $\sigma = \omega_1 = \xi = 0$ the equations of motion collapse to equations of motions for solitary rocking column with supplemental damping. Figures 4.12 and 4.13 shows response of solitary column with supplemental hysteretic and viscous dampers respectively. Each figures shows normalized rotation θ/α , velocity $\dot{\theta}$, normalized damping moment M_{damper} and normalized column weight moment M_{weight} time histories under sine pulse with maximum acceleration $a_p = 0.5g$ and period of $T_p = 0.5sec$.

From time history figures of 4.12 and 4.13 it can be seen that the dampers moment sign is always the same with the velocity direction. When the rocking column rotation increases till it reaches the maximum, the damper's force is against the rotation and it is in the same side with the weight moment. Once the rocking wall reached the maximum and it is returning to its origin (impact) the viscous damper immediately starts to prevent the wall to reach back to the floor, but in the case of hysteretic damper, the damper force first acts in the same direction of weight trying to push back the system to its origin (when the hysteretic loop is coming back to reach zero force) and then it acts against the weight direction. In the figure 4.12, the shaded areas are when the damper force is opposite to velocity direction and it is in the direction of weight when the wall goes back to its origin.

Also it worth noting that each time column hits the floor and changes pivoting points hysteretic damper preserves some residual force which activates once it starts to work again. In contrast for the viscous damper there is no residual force preserved.

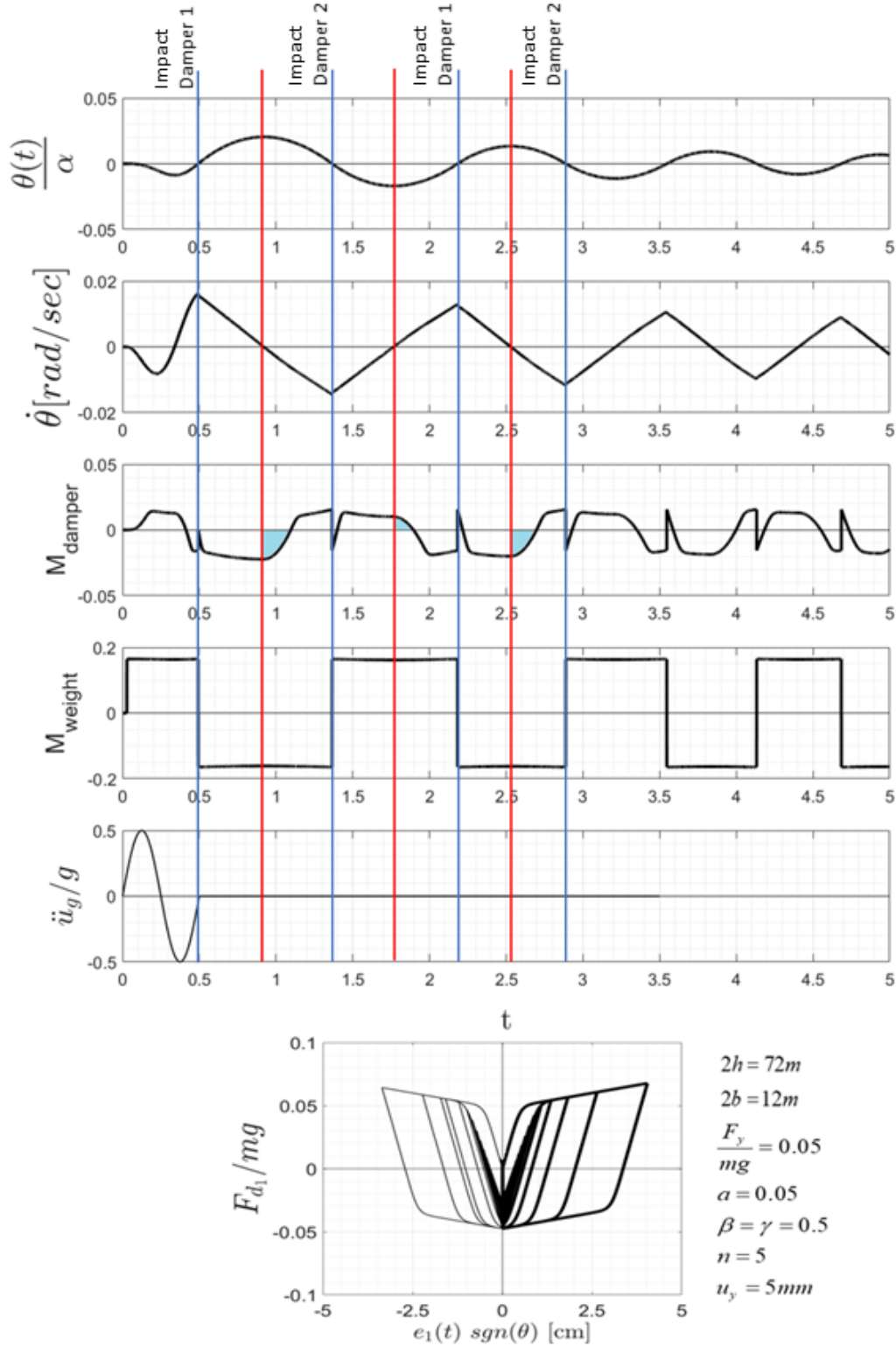


Figure 4.12: Time history analysis of a solitary stepping rocking wall size $\tan \alpha = 1/6$ with supplemental hysteretic dampers with normalized strength of $k_d u_y / m_w g = 0.05$ attached at the pivoting points when subjected to the sine pulse with $t_p = 0.5 \text{sec}$ and $a_p = 0.5g$.

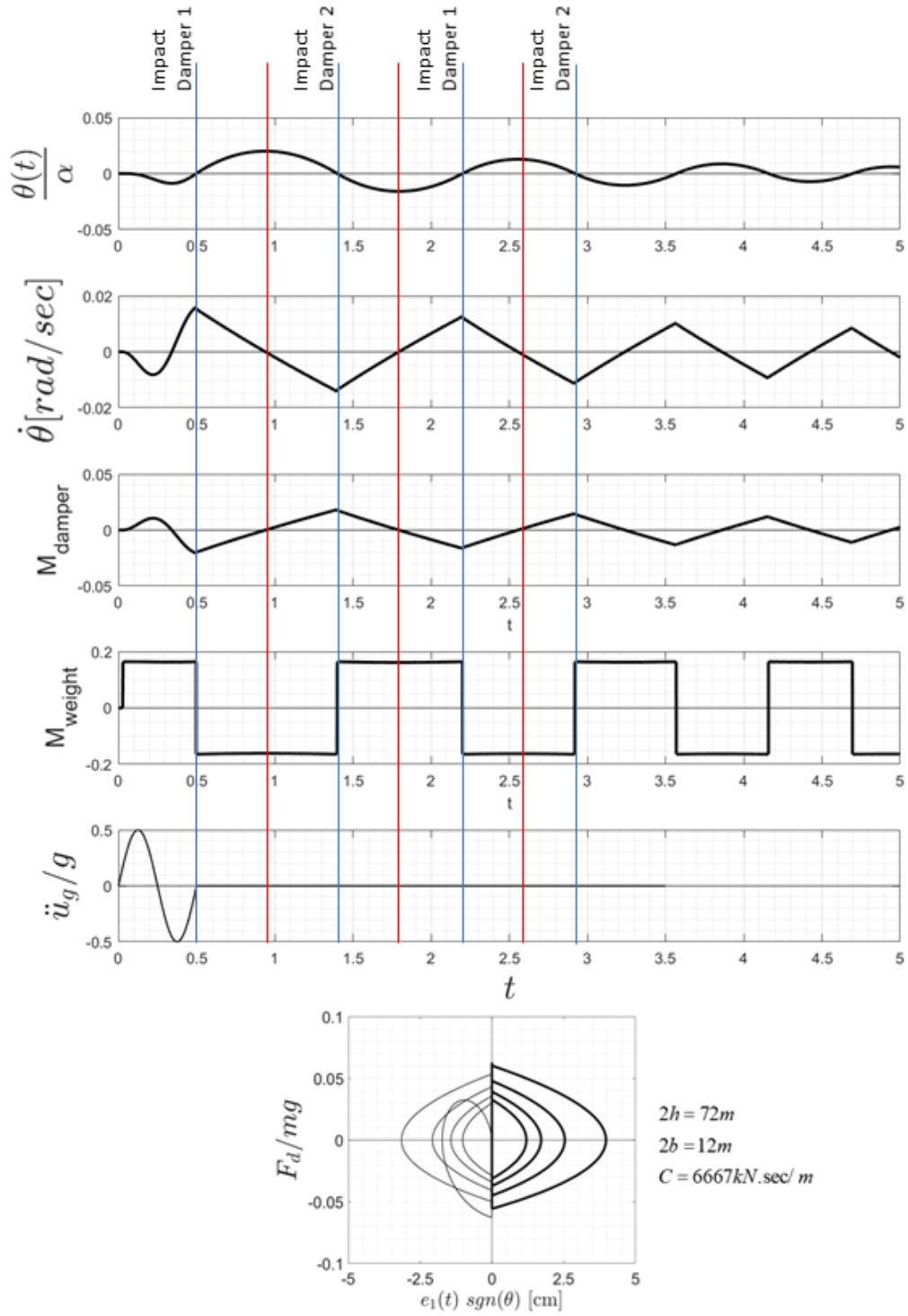


Figure 4.13: Time history analysis of a solitary stepping rocking wall size $\tan \alpha = 1/6$ with supplemental linear viscous dampers with $C = 6667 \text{ kN} \cdot \text{sec} / m$ attached at the pivoting points when subjected to the sine pulse with $t_p = 0.5 \text{ sec}$ and $a_p = 0.5g$.

The Effect of Supplemental Hysteretic and Viscous Damping on the Rocking Response of Free-Standing Columns

The remarkable seismic stability of tall, free-standing columns was first studied systematically in the seminal paper by Kirkpatrick [102]. His work brings forward the two key quantities other than the peak ground acceleration that are responsible for the stability of a slender, free-standing column: (a) the size of the column which enters the equations via the moment of inertia; and (b) the duration of the period of the excitation. Kirkpatrick [102] after correctly deriving the minimum acceleration amplitude of a harmonic excitation that is needed to overturn a free-standing column with a given size and slenderness, proceeds by presenting the first minimum-acceleration overturning spectrum (Fig. 6 of Kirkpatrick [102] paper) and shows that as the period of the excitation decreases, a larger acceleration is needed to overturn a free-standing column. While P. Kirkpatrick worked in Hawaii, it appears that his contributions were not known in Japan. Nevertheless, in the late 1940's Ikegami and Kishinouye published two important papers, one following the December 21, 1946 Nankai Earthquake [103] and the other following the December 26, 1949 Imaichi Earthquake [104]. These two papers come to confirm Kirkpatrick's theoretical findings on the rocking response of free-standing columns; since they indicate that the static threshold, $g(\text{width}/\text{height})$, is too low and is not able to explain the observed stable response of more slender; yet, larger tombstones. In their own words Ikegami and Kishinouye [104] write *"In our field investigations, we often met with cases where gravestones had not overturned because of their large dimensions in spite of the small value of the ratio between width and height"*.

About a decade later Muto et al. [105] built upon the work of Ikegami and Kishinouye [103, 104] and showed explicitly that the dynamic response of a rocking column is governed by a negative stiffness; therefore, its free-vibration response is not harmonic; rather, it is described by hyperbolic sines and cosines.

The pioneering work of Kirkpatrick [102] in association with the systematic work conducted in Japan on rocking and overturning during the first-half of the 20th century matured the knowledge on this subject to the extent that Housner [26] after introducing the concept of pulse excitations elucidated a size-frequency scale effect that explained why (a) the larger of two geometrically similar blocks can survive the excitation that will topple the smaller block and (b) out of two same acceleration amplitude pulses, the one with longer duration is more capable to induce overturning.

Following Housner's [26] paper a scarce number of publications studied the rocking response of free-standing blocks and columns [32, 35, 106–111]. The dynamics of free-standing and anchored rocking structures received increasing attention in late 1990s, after witnessing the 1994 California and 1995 Kobe, Japan earthquakes which were responsible for the overturning of a wide range of electric substation equipment [36, 54, 112].

At that time, the most common approach to prevent overturning of slender, rigid equipment was the use of restrainers (hold downs); however, a large number of restrained equipment overturned by failing the restrainers with strengths comparable to the weight of the equipment. Makris and Zhang [112] and Makris and Black [54] analyzed the rocking stability of rigid blocks when anchored with brittle and ductile restrainers and concluded that in several occasions the restrainers work against the stability of the block—that is free-standing blocks can be more stable than when are restrained.

About a decade later, the "countertuitive" findings of Makris and his coworkers were confirmed by Dimitrakopoulos and DeJong [113] who proceeded by studying the rocking stability of a slender column with supplemental linear and non-linear viscous damping at the pivoting points. Contrary to the "countertuitive" finding that is reached, when supplemental hysteretic dissipation is offered by yielding and fracturing the ductile restrainers [54, 112], the Dimitrakopoulos and DeJong [113] study concluded that supplement viscous (linear or nonlinear) dissipation enhances invariably the stability of slender rocking columns.

In view of the growing interest in rocking isolation ([27] and references reported therein) in association with the wide acceptance of supplemental energy dissipation devices and buckling restrained braces (BRBs) [95, 97, 98, 114, 115], this section first revisits the seismic response of the South Rangitikei Rail Bridge and subsequently presents a comprehensive study on the rocking seismic response of a tall, slender column equipped along its sides with vertical energy dissipation devices with finite length which offer either viscous (linear or nonlinear) or hysteretic dissipation (say from the use of vertical BRBs).

Equation of Motion of a Rocking Column with Vertical Energy Dissipators

Case 1. $\theta > 0$

For positive rotations ($\theta > 0$), since there is no oscillator attached to the column in this case ($\sigma = \omega_1 = \xi = 0$) equation (4.19) collapses to the following form

$$\ddot{\theta} = -p^2 \left[\sin(\alpha - \theta) + \frac{\ddot{u}_g}{g} \cos(\alpha - \theta) + \frac{F_{d1}}{mg} \frac{r_1}{R} + \frac{F_{d2}}{mg} \frac{r_2}{R} \right] \quad (4.27)$$

Case 2. $\theta < 0$

For negative rotation ($\theta < 0$), one can follow the same reasoning and the equation of motion is

$$\ddot{\theta} = -p^2 \left[-\sin(\alpha + \theta) + \frac{\ddot{u}_g}{g} \cos(\alpha + \theta) + \frac{F_{d1}}{mg} \frac{r_1}{R} + \frac{F_{d2}}{mg} \frac{r_2}{R} \right] \quad (4.28)$$

By virtue of the signum function, $\text{sgn}(\theta)$, equation 4.27 and 4.28 can be expressed in the compact form

$$\ddot{\theta} = -p^2 \left\{ \sin(\alpha \text{sgn}\theta - \theta) + \frac{\ddot{u}_g}{g} \cos(\alpha \text{sgn}\theta - \theta) + \frac{F_{d1}}{mg} \frac{r_1}{R} + \frac{F_{d2}}{mg} \frac{r_2}{R} \right\} \quad (4.29)$$

in which F_{d1} and F_{d2} are expressed either by equations 4.9 or 4.10 and r_1 and r_2 are the respective lever arms given by equations 4.13 and 4.14. In the special case of a zero-length damper ($l = \phi_1 = \phi_2 = 0$) attached at the corner of the column ($d = 0, S_1 = 2b, S_2 = 0$), equation 4.17 reduces to

the equation of motion presented by Dimitrakopoulos and DeJong [113] for the case of viscous dampers.

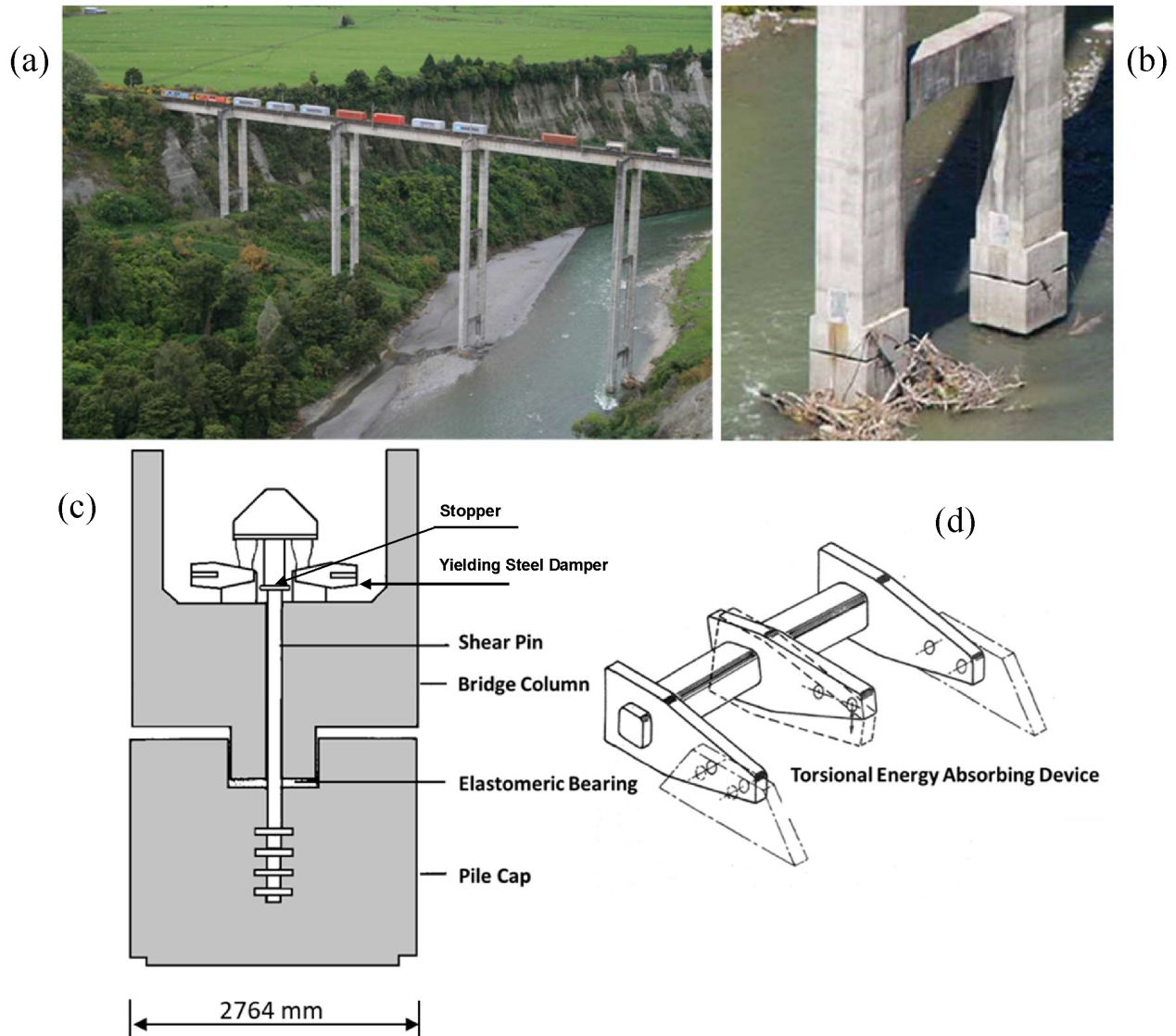


Figure 4.14: (a) View of the South Rangitikei Rail Bridge in New Zealand and (b) close-up view of the rocking interface. The piers are allowed to uplift by 12.5 cm; while the rocking motion is controlled by torsionally yielding steel-beam damper shown below. (c) Detail of the torsionally yielding steel-beam damper installation at the base of the stepping piers atop the pile cap that delivers a yield force of $2 \times 45\text{kN}$. (d) Schematic of the torsionally yielding steel-beam damper.

Review of The Transverse Rocking Response of The South Rangitikei Rail Bridge

Statement of the problem

Before examining the role of supplemental damping, either hysteretic or viscous, for a wide range of slender free-standing columns and bridge piers, this section revisits the planar (transverse) rocking response of one of the center piers of the South Rangitikei Rail Bridge shown in Figure 4.14. While the bridge piers are free to rock atop their foundation as shown in Figure 4.14, they are rigidly connected with the box-girder deck that runs atop the piers. So, the free-standing pier shown in Figure 4.15 is merely an idealization of the actual system that supports the weight of the deck with a finite transverse stiffness. Nevertheless, given the feeble transverse stiffness of the 56m long deck-span, the immense size of the bridge piers controls the dynamics of the structural system and the solitary, free-standing pier idealization shown in Figure 4.15 (right) becomes realistic [91, 116].

The prestressed concrete single-box girder deck is of uniform cross-section, that is 3.9m deep and 3.0m wide with a uniform thickness of 0.35m. By assuming a weight density of concrete = $24\text{kN}/\text{m}^3$, the weight of the 56m span-deck that is supported by each center pier is approximately 6000kN. The legs of the piers of the bridge are hollow tubes of uniform rectangular 2.79m by 2.03m cross section with a uniform thickness of 0.3m. Together with the weight of the shear cross beams, the weight of the center pier alone is estimated in the vicinity of 13000kN. Accordingly, the entire weight that reaches the rocking interface of the stepping piers is $W = mg \approx 13000\text{kN} + 6000\text{kN} = 19000\text{kN}$,[117].

At the same time the yield force from each torsionally yielding steel beam damper is $F_y = 450\text{KN}$ [100] therefore, the combined yield force from a pair of dampers is $2F_y = k_d u_y = 2 \times 450\text{kN} = 900\text{kN}$. Accordingly, the ratio $2F_y/W = k_d u_y/mg = 900\text{kN}/19,000\text{kN} = 0.047$.

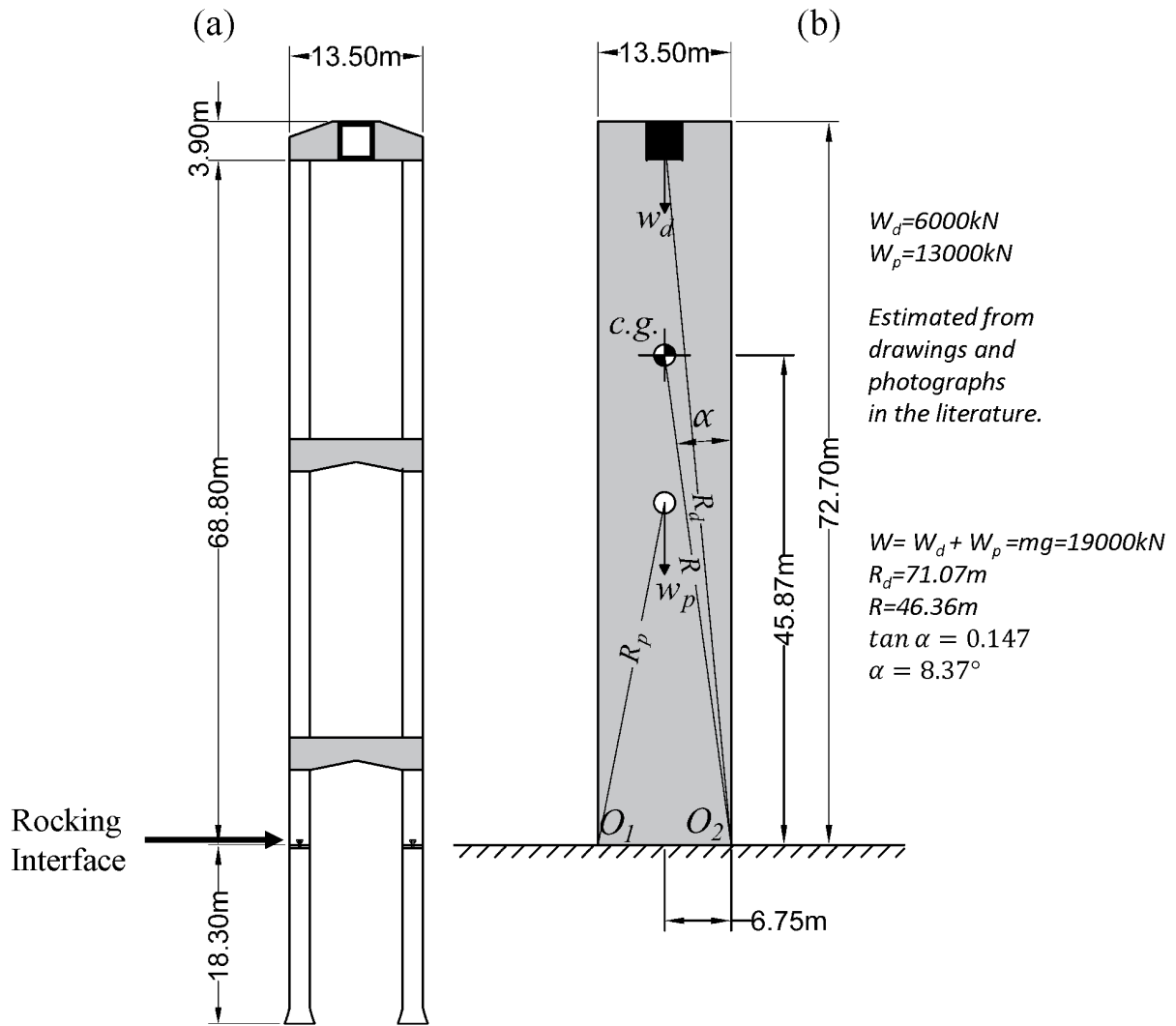


Figure 4.15: Schematic of the stepping center pier of the South Rangitikei Rail Bridge (a) together with the geometric parameters needed for planar dynamic response analysis (b).

With reference to previously derived equations of motion for yielding oscillator coupled with a rocking wall with supplemental dampers, for the case of no oscillator, the full nonlinear equation

of the stepping column with zero-length hysteretic dampers at its pivoting points is

$$\ddot{\theta} = -p^2 \left\{ \sin(\alpha \operatorname{sgn}(\theta) - \theta) + \frac{\ddot{u}_g}{g} \cos(\alpha \operatorname{sgn}(\theta) - \theta) + \sqrt{2} \sin \alpha \sqrt{1 + \cos \theta} \left[2\sqrt{2} a \frac{k_d b}{mg} \sqrt{1 - \cos \theta} + (1 - a) \frac{k_d u_y}{mg} z(t) \right] \right\} \quad (4.30)$$

which for small rotation simplifies to

$$\ddot{\theta} = -p^2 \left\{ \sin(\alpha - \theta) + \frac{\ddot{u}_g}{g} \cos(\alpha - \theta) + \frac{2 \sin \alpha}{mg} [2ak_d b \tan \theta + (1 - a)k_d u_y z(t)] \right\} \quad (4.31)$$

During the oscillatory rocking motion of a free standing rigid column (no dampers) energy is lost only during impact, when the angle of rotation reverses. When the angle of rotation reverses, it is assumed that the rotation continues smoothly from points O_2 to O_1 and that the impact force is concentrated at the new pivot point O_1 . With this idealization, the impact force applies no moment about O_1 ; hence, the angular momentum is conserved. Conservation of angular momentum about point O_1 just before the impact and right after the impact gives that the angular velocity after the impact= $\dot{\theta}_a$ is only η times the angular velocity before the impact= $\dot{\theta}_b$; where η depends solely on geometry

$$\eta = \frac{\dot{\theta}_a}{\dot{\theta}_b} = 1 - \frac{3}{2} \sin^2 \alpha \quad (4.32)$$

The result offered by equation 4.32 is merely the minimum energy dissipation required during impact for a column with slenderness α to engage in rocking motion (not to jump). It so happens that in several occasions, the mechanical energy lost during the impacts of rocking slender columns is close to the amount demanded by equation 4.32 and this is why rocking materializes. However, this energy loss is too little to suppress rocking vibrations and slender structures have the tendency to rock free for repeated cycles. Accordingly, additional energy dissipation is required as was implemented in the case of the South Rangitikei Rail Bridge with the torsional yielding steel-beam

dampers shown in Figure 4.1.

Time history response analysis of the South Rangitikei Rail Bridge

In the late 1960s when the design of the stepping South Rangitikei Rail Bridge was conceived, there were available a handful of strong earthquake records such as the N-S component of the 1940 El Centro, California Earthquake and the *CO2/065* record from the 1966 Parkfield, California Earthquake. These motions were considered strong at that time, merely because of their high peak ground acceleration (PGA) and were used for the dynamic response analysis during the preliminary design of the South Rangitikei Rail Bridge [90, 91]. The concept of coherent acceleration pulses radiating from a rapidly slipping fault was in its infancy at that time and started receiving attention only after the 1971 San Fernando, California earthquake [1, 118–120]. Accordingly, in this section we first present results on the planar rocking response of the center pier (together with the weight of its corresponding deck) of the South Rangitikei Rail Bridge when subjected to pre-1971 known strong records; and subsequently we present its response when subjected to pulse-like near-source ground motions containing coherent, long-duration acceleration pulses which are particularly destructive to a variety of structures. With reference to Figure 4.15, the elevated center of mass of the center pier due to the weight of the deck ($w_{deck} = 6000\text{kN}$) that is supported by the pier is at $h_p = 45.87\text{m}$; therefore the dynamic slenderness of the pier is $\tan \alpha = 0.5 \times 13.5\text{m} / 45.87\text{m} = 0.147$ ($\alpha = 8.372^\circ$). Its moment of inertia about the pivoting points O_1 and O_2 is approximately $I_o = \frac{4}{3} \frac{W_p}{g} R_p^2 + \frac{W_d}{g} R_d^2 = 5.2 \times 10^6 M g.m^2$.

According to the final design, the installation of the torsionally yielding steel-beam dampers at the base of the stepping piers have a stopper that limits the uplift of each leg to 12.5cm. Consequently, the maximum allowed rotation is $\tan \theta_{stop} = 0.125\text{m} / 13.5\text{m} = 0.0092$; therefore, $\theta_{stop} / \alpha = \tan \theta_{stop} / \tan \alpha = 0.063$.

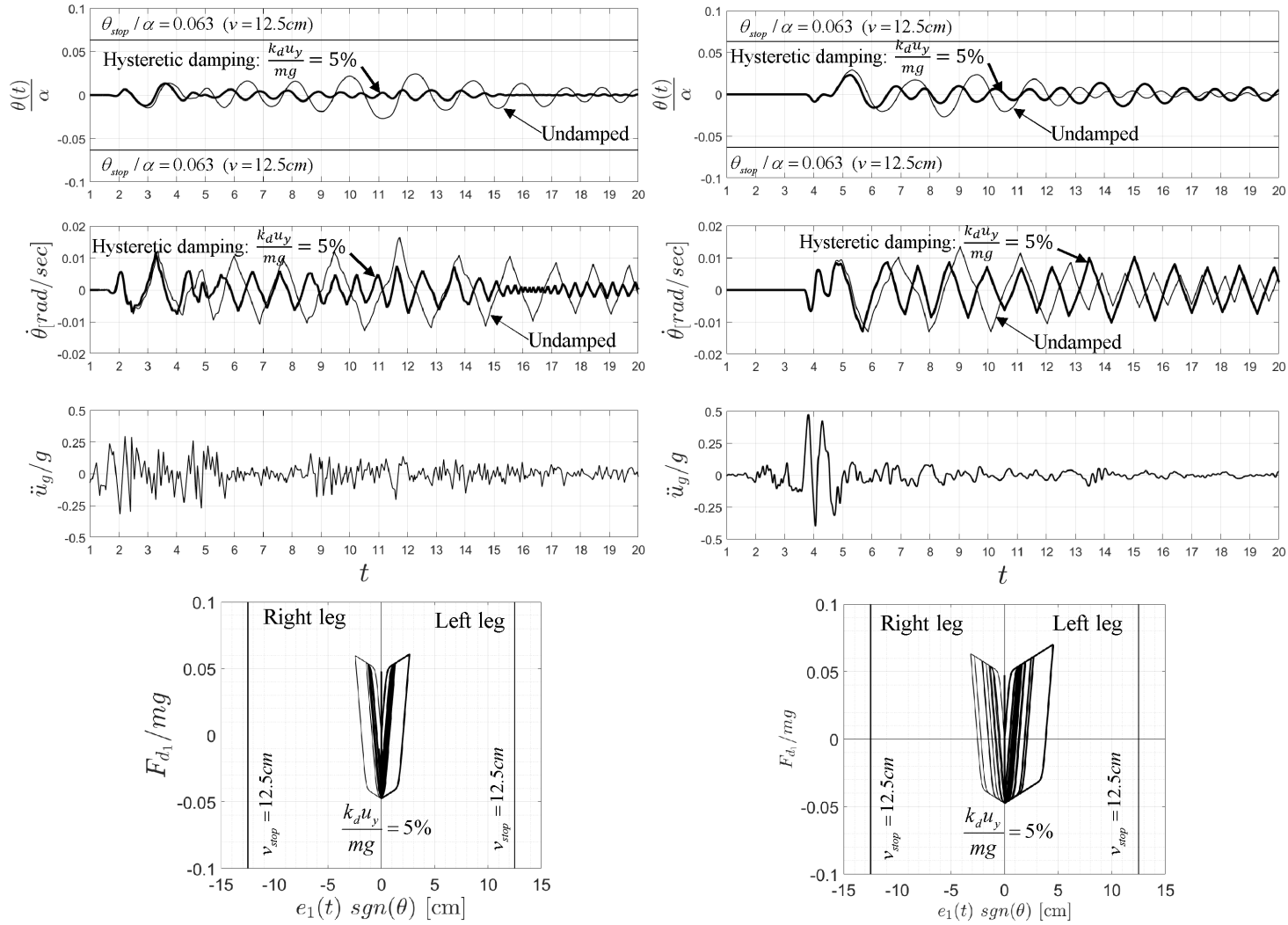


Figure 4.16: Rotation and angular velocity time histories of the 72.7m tall center pier of the South Rangitikei Rail Bridge when subjected to the North-South component of the El Centro ground motion recorded during the 1940 Imperial Valley, California earthquake (left) and the CO2/064 ground motion recorded during the 1966 Parkfield, California earthquake (right). Thin lines: No dampers. Heavy solid lines: Hysteretic dampers with $k_d u_y / (mg) = 5\%$. Bottom: Force-displacement loops of the 900kN hysteretic dampers installed at each leg of the pier. Positive rotation is clockwise.).

Figure 4.16 (left) plots with a thin solid line rotational and angular velocity time histories of the undamped center pier of the South Rangitikei Rail Bridge by including the 6000kN weight of its corresponding deck at the pier head when subjected to the N-S component of the 1940 El Centro, California recorded ground motion also shown in Figure 4.16 (left). The center pier undergoes small rotations which are less than 1/3 of the peak allowed rotation ($\theta_{stop}/\alpha = 0.063$) before the stopper engages. While the rotations are small, the amount of damping given by equation 4.32—that is the minimum damping needed for the pier to engage in rocking motion, is too small and the rocking pier experiences repeated cycles as shown in Figure 4.16 for the undamped response. It is these repeated cycles that motivated the design and installation of the torsionally yielding steel-beam dampers at the base of the stepping piers shown in Figure 4.14. The solid dark line in Figure 4.16 shows the rocking response of the center pier of the South Rangitikei Bridge when the torsionally yielding steel-beam dampers are engaged (as described by equations 4.30 or 4.31) where $(k_d u_y)/mg = 5\%$ and $(k_d b)/mg = 67.5$ (we have assumed that yield displacement of the torsionally yield steel-beam damper is $u_y = 5mm = 0.005m$; whereas $b = 13.5m/2 = 6.75m$). The post-to-preyielding stiffness ratio, a , of the torsionally yielding steel-beam dampers has been assumed equal to 5% ($a = 0.05$) after observing recorded hysteretic loops from tests on scale models presented in Figure 10 of the Kelly et al. [89] paper. The numerical integration of the nonlinear equation of motion given by equation 4.30 shows that the center pier undergoes very small rotations ($\theta_{max}/\alpha = 0.013$) which are less than 1/4 of the peak allowed rotations, θ_{stop} , while the hysteretic dampers are effective in suppressing the successive rocking cycles. The force-displacement loops of the torsionally yielding steel-beam dampers are shown in Figure 4.16 (left) below the recorded ground motion.

Figure 4.16 (right) plots the same response quantities as those discussed for Figure 4.16 (left) when the pier of the South Rangitikei Rail Bridge is subjected to the CO2/065 ground motion recorded during the 1966 Parkfield, California earthquake. The center pier undergoes small rota-

tions ($\theta_{max}/\alpha = 0.022$ —that is the bridge enjoys a factor of safety: $FS = 1/0.022 = 45$), which are less than half the peak allowed rotations ($\theta_{stop}/\alpha = 0.063$). The heavy solid lines show the response when hysteretic dampers with $k_d u_y/(mg) = 5\%$ are engaged, whereas the force-displacement loops of the torsionally yielding steel-beam dampers are shown at the bottom of Figure 4.16 (right).

Scholia

Figure 4.16 reveals that when the South Rangitikei Rail Bridge is excited along the transverse direction by the strongest records available at the time of its design (late 1960s-early 1970s), the nonlinear response of this 72.7m tall stepping bridge is precisely what was predicted during its design and the bridge does exactly what was intended to do [89–91, 99, 100, 121, 122]. Its peak rotation is somewhere between 1.5% and 2.5% of its slenderness α —that is the ultimate rotation of the verge of overturning (a factor of safety of 40 and above), while the 900kN–capacity hysteretic dampers installed at the base of each leg of the stepping piers dissipated effectively the rocking vibration of these immense stepping piers. The stopper of the base of the pier is wisely gauged at 12.5cm of uplift—that is 2.8 times larger than the computed peak uplift demands shown in Figure 4.16. All the above make the analysis, design and construction of the South Rangitikei Rail Bridge a remarkable engineering accomplishment in modern times.

The reader needs to also recognize that the innovative design of the stepping South Rangitikei Rail Bridge was a seminal moment in seismic isolation by introducing the implementation of response modification devices for seismic protection of structures [89, 99]. Furthermore, the innovative design of the rocking bridge is in accordance with current engineering concepts of resilient engineering where recentering of the structures is achieved invariably due to gravity without the bridge experiencing any damage even when excited by most violent earthquakes. Despite its remarkable design and its 1/2 century-long outstanding seismic performance, the stepping design of the South

Rangitikei Rail Bridge has not received the attention it deserves since even at present the design of nearly all tall, valley bridges remains entrenched into capacity design leading to disproportionately large and expensive pile or caisson foundations.

Response of the South Rangitikei Rail Bridge to more Violent Earthquake Records

As the design of the South Rangitikei Rail Bridge was underway, the 1971 San Fernando earthquake occurred on February 9 in the foothills of the San Gabriel Mountains in South California. Damage was severe in the northern San Fernando Valley including the spectacular failure of several major freeway bridges and the Olive View Hospital.

Figure 4.17 (left) shows rotation and angular velocity time histories of the planar rocking response of the 72.7m-tall center pier of the South Rangitikei Rail Bridge when subjected to Pacoima Dam/164 ground motion recorded some 3 miles east of the well-engineered at that time Olive View Hospital which reached the verge of collapse by developing a soft first story failure. The Pacoima Dam record shown in Figure 4.17 is a well-known record in the literature since from its 2nd second to its 4th second contains a long acceleration pulse that imposes severe deformation demands on structures [1, 120].

Despite the most devastating kinematic characteristics of the 1971 Pacoima dam record shown in Figure 4.17 (left), the damped 72.7m tall center pier of the South Rangitikei Rail Bridge undergoes small rotations ($\theta_{max}/\alpha = 0.0497$) which are still less than the peak allowed rotation ($\theta_{stop}/\alpha = 0.063$). The 900kN capacity torionally yielding steel-beam dampers are most effective in suppressing the overall response and all the response results shown in Figure 4.17 (left) demonstrate that the stepping bridge performs remarkably well (essentially the bridge performs at a serviceability level) even when excited by the 1971 Pacoima Dam record which may induce collapse to most code-compliant structures when designed with the ductile capacity philosophy.

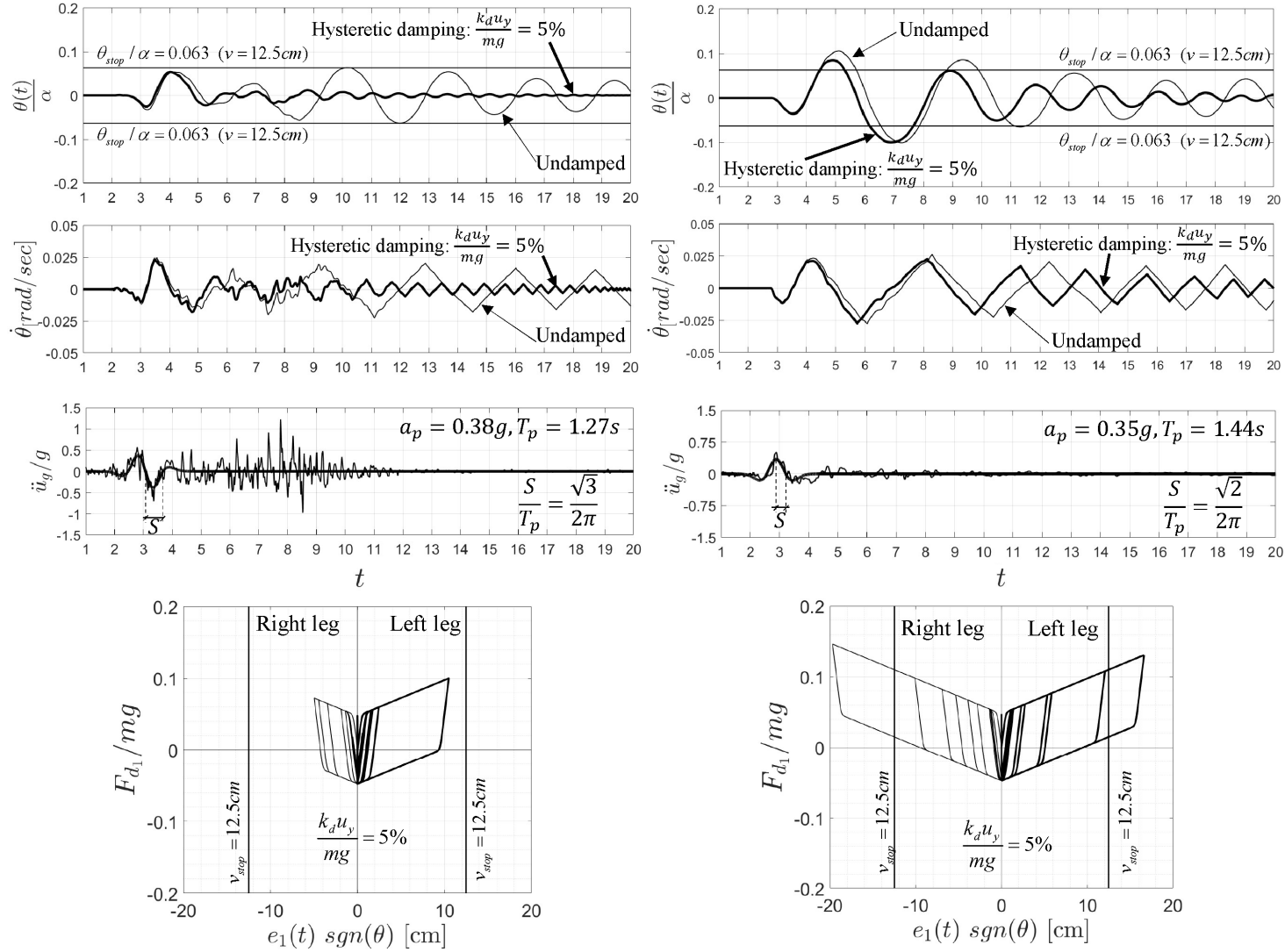


Figure 4.17: Rotation and angular velocity time histories of the 72.7m tall center pier of the South Rangitikei Rail Bridge when subjected to the Pacoima Dam/164 ground motion recorded during the 1971 San Fernando, California earthquake (left) and the North-South component of the ground motion recorded during the 1992, Erzincan, Turkey earthquake (right). Thin lines: No dampers. Heavy solid lines: Hysteretic dampers with $k_d u_y / (mg) = 5\%$. Bottom: Force-displacement loops of the 900kN hysteretic dampers installed at each leg of the pier. Positive rotation is clockwise.

Figure 4.17 (right) plots the same response quantities as these discussed in Figure 4.17 (left) when the 72.7m tall pier of the South Rangitikei Rail Bridge is subjected to the most violent North-South component of the ground motion recorded during the 1992 Erzincan, Turkey earthquake. The rotations of the stepping pier when the hysteretic dampers are engaged exceed the threshold rotation from the stoppers ($\theta_{stop}/\alpha = 0.063$); yet, they are below 10% of the slenderness α —that is a factor of safety $FS \geq 1/0.098 \approx 10\%$. Furthermore, the damped motion shown with a heavy solid line is systematically inferior to the undamped motion shown with a thin solid line.

An "Unexpected" Combination of Gravity, Inertia and Hysteretic Forces

In the previous section we computed the nonlinear response of the center pier of the South Rangitikei Rail Bridge and it was shown that the hysteretic damping offered by the torsionally yielding steel beam-dampers ($ku_y/mg = 0.05$, $a = 0.05$, $u_y = 0.5cm$) suppress invariably the rocking response; while the overall dynamic response of the bridge is precisely what was predicted during its original design [89–91, 99, 100].

Figure 4.18 (left) plots with a thin solid line rotational and angular velocity time histories of the undamped stepping center-pier of the South Rangitikei Rail Bridge when subjected to the Newhall/360 ground motion recorded during 1994 Northridge, California earthquake. What is interesting with this particular ground motion is that when hysteretic damping is added ($((k_d u_y)/mg = 5\%)$), the peak response of the damped pier $= \theta_{max}/\alpha = 0.030$, exceeds the peak response of the undamped pier $= \theta_{max}/\alpha = 0.024$. While this difference is insignificant, it is worth noting that while the hysteretic damping forces may reduce the rotations when the pier is rocking in one direction (the damped pier is leaning back less than the undamped pier); it may happens that during the next half cycle of the ground acceleration, the damped pier that is leaning less backwards is more prone to rotate forward than the undamped pier.

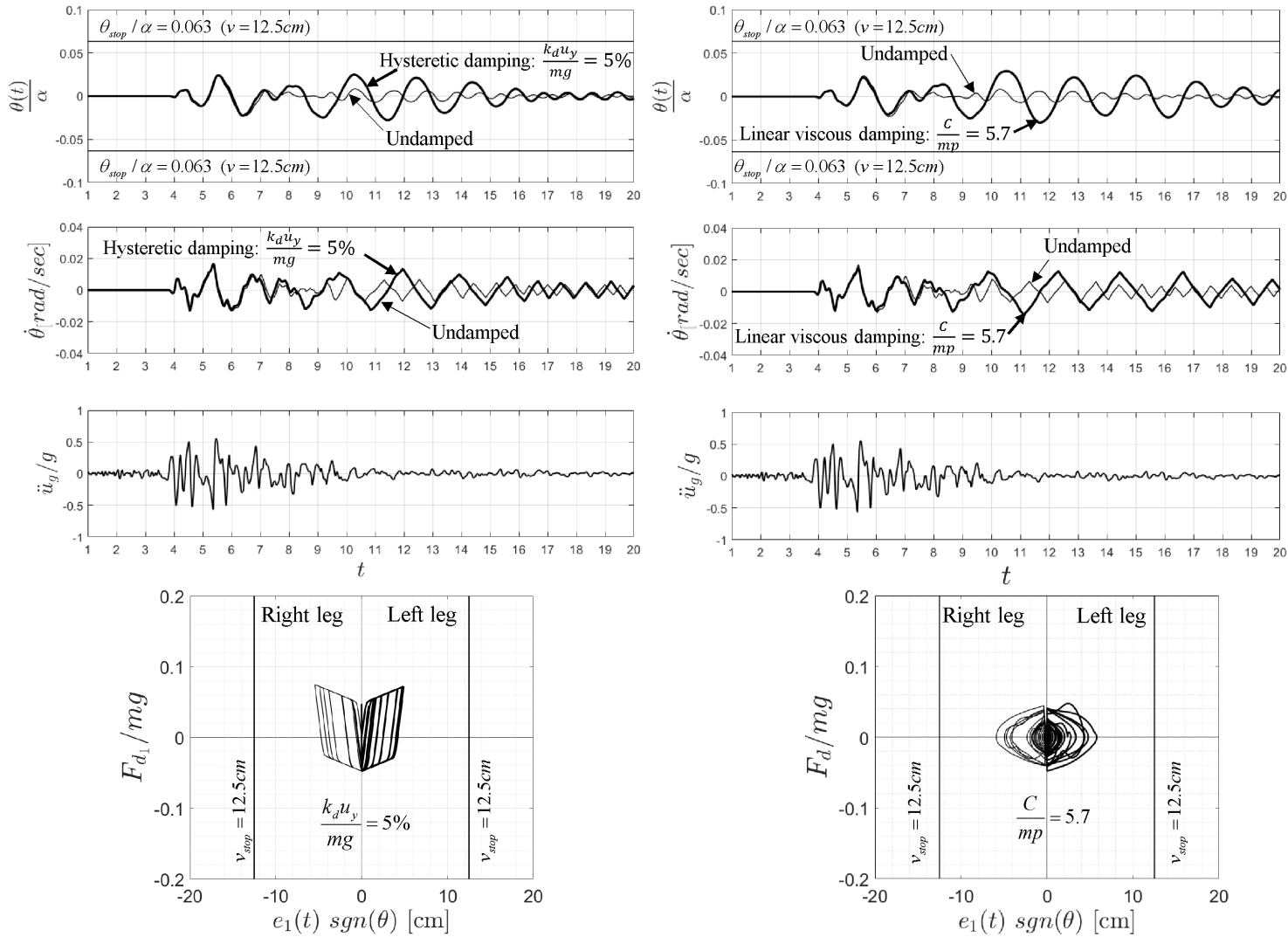


Figure 4.18: Rotation and angular velocity time histories of the 72.7m tall center pier of the South Rangitikei Rail Bridge when subjected to the Newhall/360 ground motion recorded during the 1994 Northridge, California earthquake. Thin lines: No dampers. Heavy solid lines: Hysteretic dampers with $k_d u_y / (mg) = 5\%$ (left) and linear viscous dampers with $C / (mp) = 5.7$ (right). Bottom: Force-displacement loops of the 900kN hysteretic (left) and linear viscous (right) dampers installed at each leg of the pier. Positive rotation is clockwise.

Rocking Response with Viscous Dampers

In view of the "unexpected" amplification of the response of the stepping bridge shown in Figure 4.18 (left) when hysteretic energy dissipators are used, this section examines whether this unfavorable combination of gravity, inertia and hysteretic forces also happens when viscous dissipation is used. We first consider that the installation of viscous dampers is similar to the installation of the torsionally yielding hysteretic dampers at the bottom of the stepping piers of the South Rangitikei Rail Bridge.

This configuration is essentially the configuration studied by Dimitrakopoulos and DeJong [113] and corresponds to zero-length elements ($l = \phi_1 = \phi_2 = 0$) at the pivoting points of the stepping pier ($d = S_2 = 0$ and $S_1 = 2b$). In this case equations (4.4) and (4.15) simplify to the equation given by (4.22); while the time derivative of the stroke is given by equation (4.24).

Accordingly, the full nonlinear equation of the stepping pier with zero-length viscous (linear or nonlinear) dampers at its pivoting points is

$$\ddot{\theta} = -p^2 \left\{ \sin(\alpha - \theta) + \frac{\ddot{u}_g}{g} \cos(\alpha - \theta) + \frac{\sqrt{2} \sin \alpha}{mg} \sqrt{1 + \cos \theta} C_q \left| \sqrt{2} b \dot{\theta} \sqrt{1 + \cos \theta} \right|^q \text{sgn}[\dot{\theta}] \right\} \quad (4.33)$$

which for small rotations simplifies to

$$\ddot{\theta} = -p^2 \left\{ \sin(\alpha - \theta) + \frac{\ddot{u}_g}{g} \cos(\alpha - \theta) + \frac{2 \sin \alpha}{mg} C_q |2b \dot{\theta}|^q \text{sgn}[\dot{\theta}] \right\} \quad (4.34)$$

By comparing, the right hand-side of the equation (4.31) and (4.34), a peak damping force from the viscous dampers $C_q [2b \dot{\theta}_{max}]^q$, will match the yield capacity of the torsionally yielding hysteretic dampers when

$$C_q = \frac{k_d u_y}{(2b \dot{\theta}_{max})^q} \quad (4.35)$$

Figure 4.18 (left) shows that when the pier of the South Rangitikei Rail Bridge is subjected to the 1994 Newhall/360 record the peak angular velocity $\dot{\theta}_{max} = 0.015$ rad/sec. Accordingly for the pair of torsionally yielding steel-beam dampers with yield capacity $k_d u_y = 900$ kN, the corresponding damping constant C_1 for linear viscous dampers ($q = 1$) is $C_1 = \frac{900 \text{ kN}}{(13.5 \text{ m})(0.015 \text{ rad/sec})} = 4444.4 \text{ kNsec/m} = 4444.4 \text{ Mg/sec}$ and $C_{1/2}$ for nonlinear viscous ($q = 1/2$) is $C_{1/2} = \frac{900 \text{ kN}}{\sqrt{(13.5 \text{ m})(0.015 \text{ rad/sec})}} = 2000 \text{ kNsec}^{1/2}/\text{m}^{1/2} = 2000 \text{ Mg m}^{1/2}\text{sec}^{-3/2}$.

Figure 4.18 (right) compares the undamped and viscously damped response of the stepping center-pier of the South Rangitikei Rail Bridge when subjected to the Newhall/360 ground motion recorded during the 1994 Northridge, California earthquake. As in the case where hysteretic dampers are used (Figure 4.18 (left)), Figure 4.18 (right) shows that the rocking response of the pier when equipped at each pivot points with a linear viscous damper with damping constant, $C = 4444.4 \text{ kNsec/m} = 4444.4 \text{ Mg/sec}$, the damped response is more aggravated than the undamped response.

To this end, the remarkable seismic performance of the South Rangitikei Rail Bridge along the transverse direction is shown in Figure 4.19 which plots rotational and angular velocity time histories of the undamped and damped center pier when subjected to the Lyttleton REHS ground motion recorded during the 2011 Christchurch, New Zealand earthquake [123]. The peak rotation of the undamped pier when excited by this most violent motion is $\theta_{max}/\alpha = 0.1225$ —that is a factor of safety, $FS = \alpha/\theta_{max}$ that is larger than 8. Figure 4.19 shows that when either hysteretic damper is added ($\frac{k_d u_y}{mg} = 5\%$, shown in Figure 4.19 (left)) or its equivalent viscous damping ($\frac{C}{mp} = 4.3$, shown in Figure 4.19 (right)), the damped response is (as expected) inferior than the undamped response.

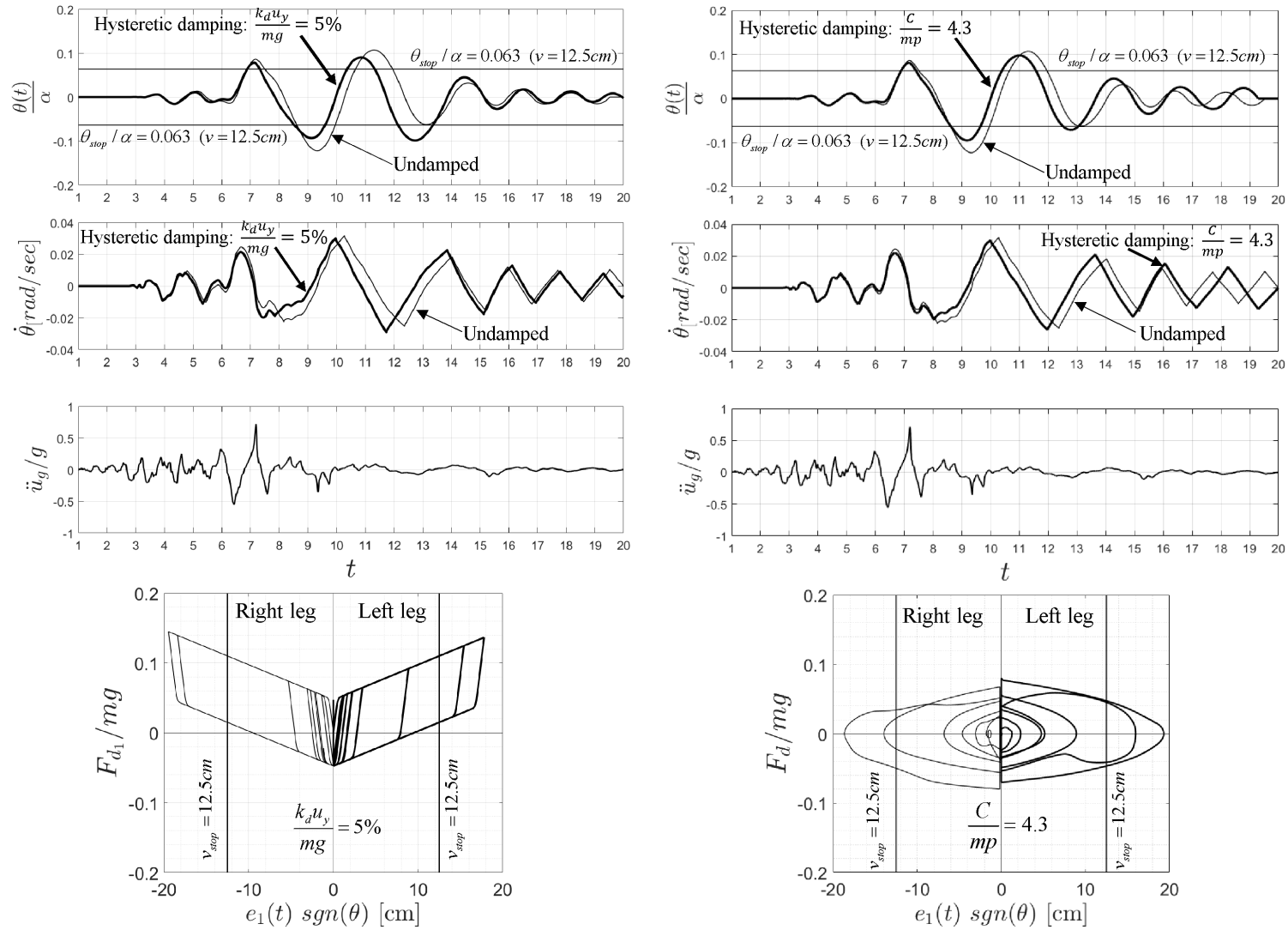


Figure 4.19: Rotation and angular velocity time histories of the 72.7m tall center pier of the South Rangitikei Rail Bridge when subjected to the REHS ground motion recorded during the 2011 Christchurch, New Zealand earthquake. Thin lines: No dampers. Heavy solid lines: Hysteretic dampers with $k_d u_y / (mg) = 5\%$ (left) and linear viscous dampers with $C / (mp) = 4.3$ (right). Bottom: Force-displacement loops of the 900kN hysteretic (left) and linear viscous (right) dampers installed at each leg of the pier. Positive rotation is clockwise.

Response To Mathematical Pulses

In an effort to better understand the origin of the occasional crossing of the rocking response diagrams this study proceeds by examining the response of supplementaly damped rocking columns to smooth mathematical pulses that can approximate the coherent, distinguishable pulses of recorded strong ground motions. Such mathematical acceleration pulses can be either simple rectangular pulses [50, 70], trigonometrix pulses [4, 68, 124] or more sophisticated wavelet functions [125, 126].

The heavy dark line in Figure 4-17 (right) that approximates the coherent, long-period acceleration pulse of the NS component of the 1992 Erzincan, Turkey record is scaled expression of the second derivative of the Gaussian function, $e^{-t^2/2}$, known in the seismological literature as the symmetric Ricker wavelet [73, 75].

$$\psi(t) = a_p \left(1 - \frac{2\pi^2 t^2}{T_p^2} \right) e^{-\frac{1}{2} \frac{2\pi^2 t^2}{T_p^2}} \quad (4.36)$$

The value of $T_p = \frac{2\pi}{\omega_p} = \pi\sqrt{2}s$ is the period that maximizes the Fourier spectrum of the symmetric Ricker wavelet; whereas, the time scale s , is the time from the peak acceleration of the wavelet to its first zero-crossing. Similarly, the heavy dark line in Figure 4-17 (left) which approximates the long-period acceleration pulse of the Pacoima Dam motion recorded during the February 9, 1971 San Fernando, California earthquake is a scaled expression of the third derivative of the Gaussian function.

$$\psi(t) = \frac{a_p}{\beta} \left(\frac{4\pi^2}{3T_p^2} - 3 \right) \frac{2\pi t}{\sqrt{3}T_p} e^{-\frac{1}{2} \frac{4\pi^2 t^2}{3T_p^2}} \quad (4.37)$$

in which β is a factor equal to 1.3801 that enforces the expression given by equation 4.37 to have

a maximum equal to a_p .

Figure 4-20 plots rocking spectra of free-standing columns with constant slenderness, $\tan \alpha = 1/6$ as a function of $\omega_p/p = \frac{2\pi}{pT_p}$ with zero-length supplemental hysteretic damping (left) with normalized yield-strength $\frac{k_d u_y}{mg} = 5\%$ and 10% and linear viscous dampers (right) with normalized damping constant $\frac{C}{mp} = 5$ and 10 which are appended at the pivoting points of the stepping column ($d = 0$). The top plots are for symmetric Ricker pulses with acceleration amplitude, $a_p = 0.35g$; whereas, the bottom pulses are for stronger symmetric Ricker pulses with acceleration amplitude, $a_p = 0.5g$. Figure 4-20 indicates the rocking spectra due to a symmetric mathematical pulse are ordered in terms of the amount of damping without showing any crossings. In contrast, Figure 4-21 which plots rocking spectra of damped free-standing columns when subjected to the antisymmetric Ricker wavelet expressed by equations provided, shows that there are situations when the response with higher values of damping exceeds the response with lower damping.

Rocking Response Diagrams

In view of the unexpected findings shown in Figure 4.18 which are due to the nonlinear dynamics of rocking, the peak rocking response of free standing columns with supplemental hysteretic or viscous dampers is summarized in the rocking response diagrams shown in Figures 4.22 to 4.25, which for a given ground motion plot the normalized to the slenderness peak rotation as the size of the column is increases. The upper bound of the rocking diagrams, $\theta/\alpha = 10^0 = 1$, is when the column is at the verge of overturning.

Figure 4.22 plots rocking response diagrams for free-standing columns with increasing size R , yet constant slenderness, $\tan \alpha = 1/6 = 0.166$ with zero-length supplemental hysteretic dampers with normalized yield-strength $\frac{k_d u_y}{mg} = 5\%$ and 10% which are appended at the pivoting points ($d = 0$).

The first observation is that as the size of the column, R , increases, the free-standing columns

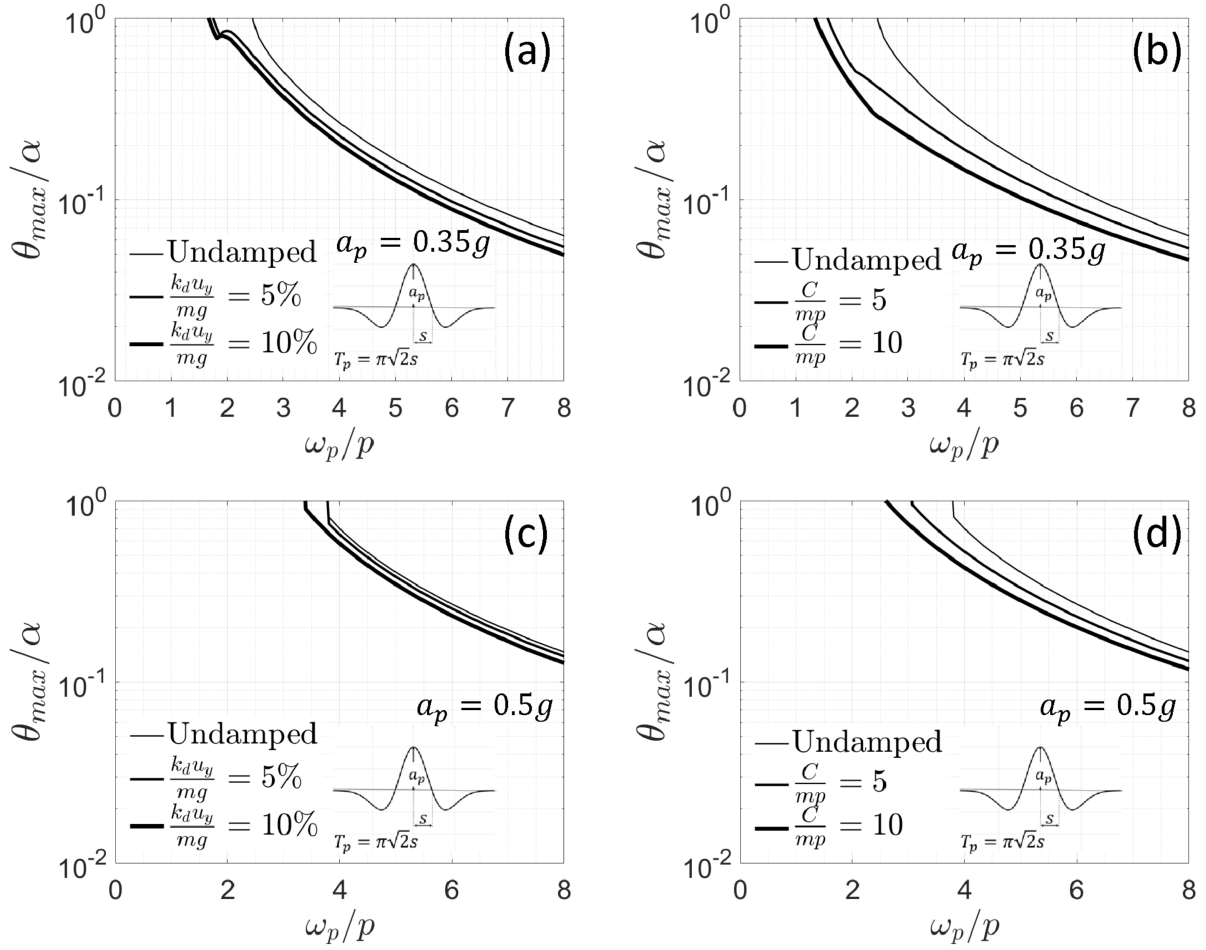


Figure 4.20: Rocking spectra of free-standing columns with slenderness, $\tan \alpha = 1/6$ with various levels of supplemental damping appended at their pivoting points when subjected to a symmetric Ricker wavelet with acceleration amplitude, $a_p = 0.35g$ (plots (a) and (b)) and $a_p = 0.5g$ (plots (c) and (d)).

become remarkably stable. For instance even when excited by the 1971 Pacoima Dam record, or the 1994 Newhall/360 record, any column with $\tan \alpha = 1/6$ that is taller than $40m$ (say a pier of a valley bridge) experiences a peak rotation θ_{max} that is less than $\alpha/10$. Figure 4.22 also indicates that the effectiveness of hysteretic supplemental damping in suppressing the rocking response depends strongly on the kinematic characteristics of the ground motion. Whenever the damped response exceeds that undamped response, the exceedance is marginal and in most cases the damped

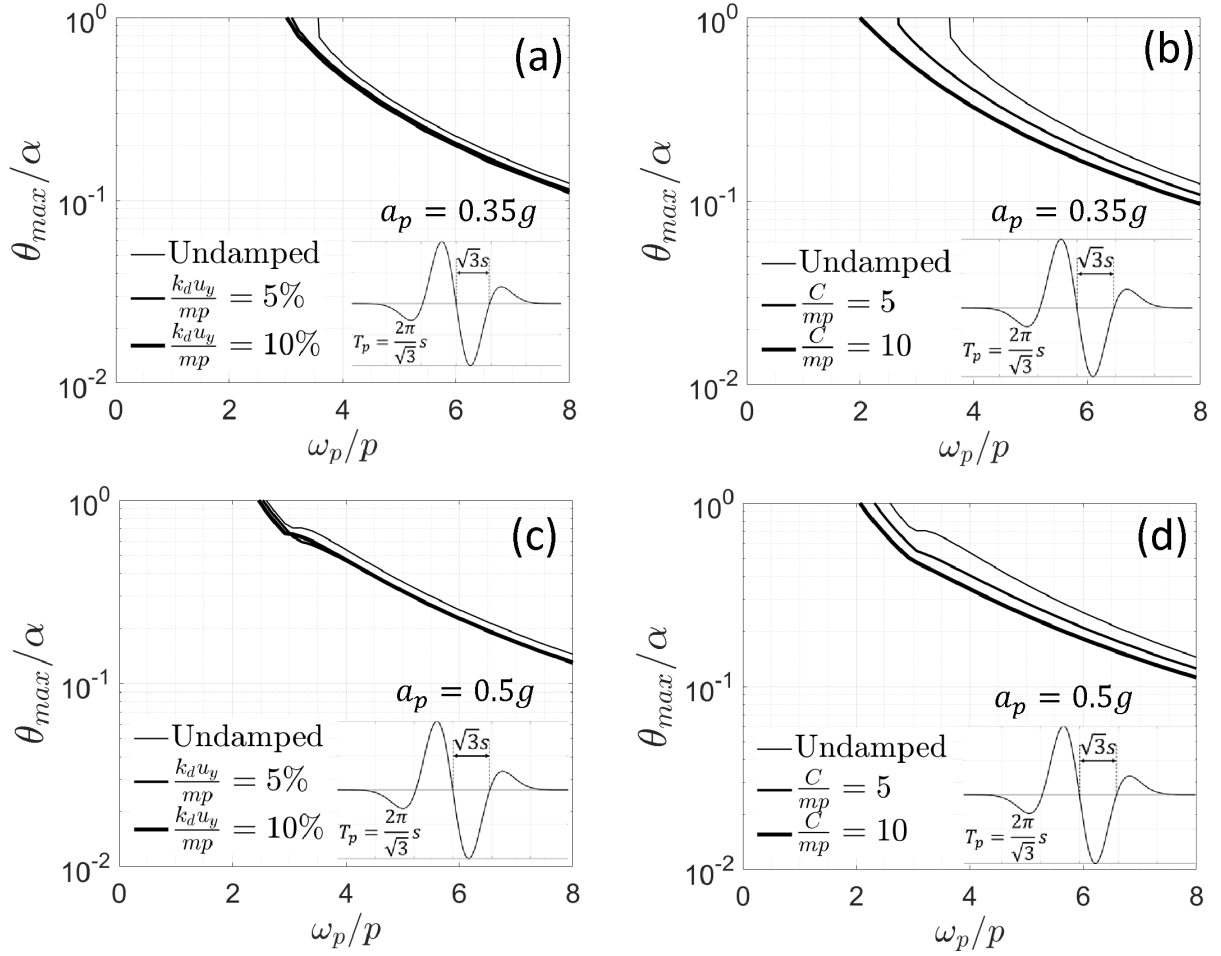


Figure 4.21: Rocking spectra of free-standing columns with slenderness, $\tan \alpha = 1/6$ with various levels of supplemental damping appended at their pivoting points when subjected to a antisymmetric Ricker wavelet with acceleration amplitude, $a_p = 0.35g$ (plots (a) and (b)) and $a_p = 0.5g$ (plots (c) and (d)).

response is lower than the undamped response. The same trends are shown in Figure 4.23 which plots rocking response diagrams for free-standing columns with slenderness $\tan \alpha = 1/6$ with zero-length supplemental viscous dampers with normalized damping constant $\frac{C}{mp} = 5$ and 10 which are appended at the pivoting points of the stepping column ($d = 0$).

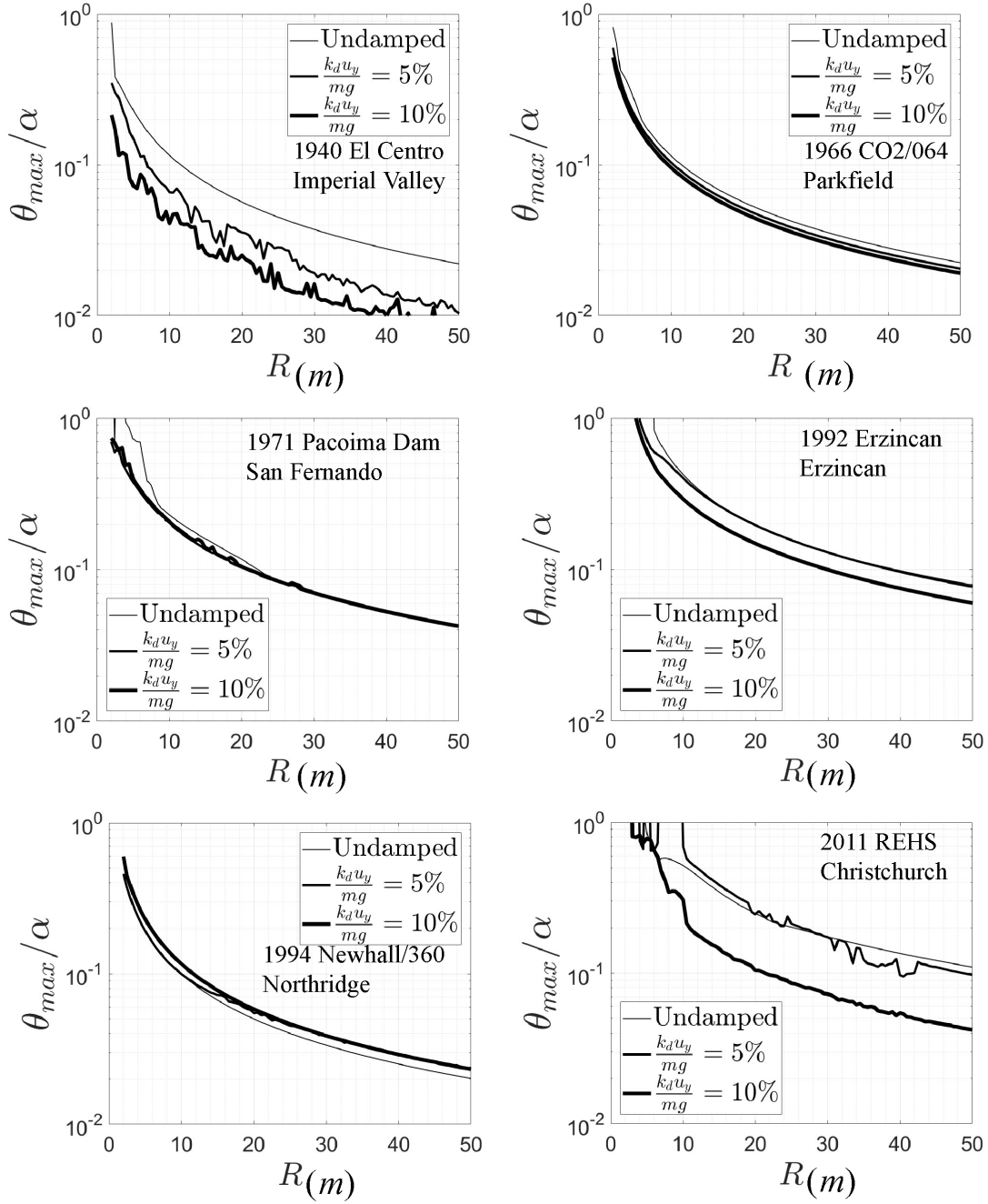


Figure 4.22: Peak rotation as a function of the size of free-standing columns with slenderness $\tan \alpha = 1/6 = 0.167$ with zero-length supplemental hysteretic dampers appended at the pivoting points ($d = 0$) when excited by the six strong ground motions presented in this study.

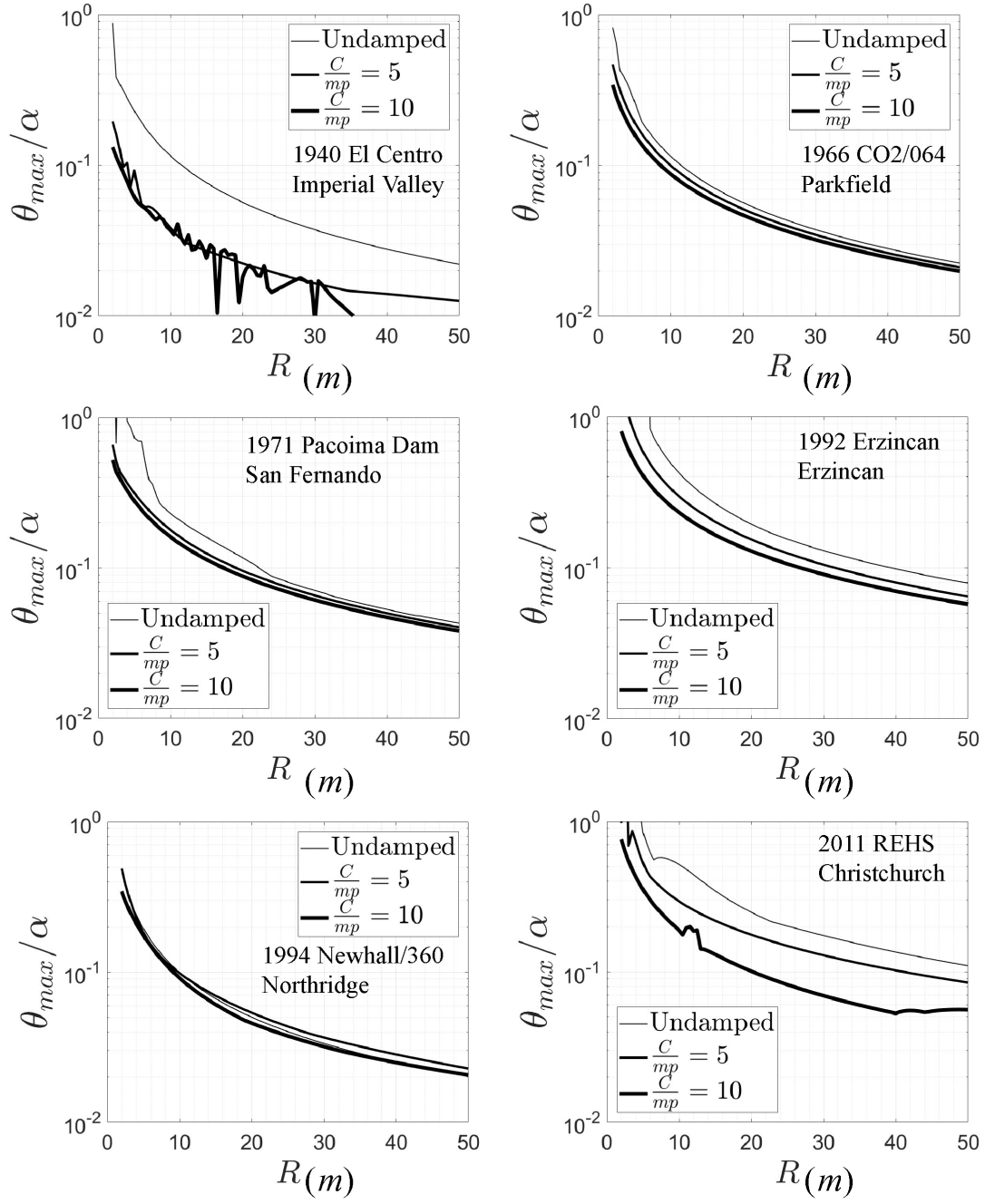


Figure 4.23: Peak rotation as a function of the size free-standing columns with slenderness $\tan \alpha = 1/6 = 0.167$ with zero-length supplemental viscous dampers ($q = 1$) appended at the pivoting points ($d = 0$) when excited by the six strong ground motions presented in this study.

Retrofit of Rocking Columns with Vertical Energy Dissipation Devices with Finite Length

There are several situations where it is suitable to place the supplemental energy dissipation devices along the sides of rocking columns or a rocking walls [89, 99] as it is shown in Figure 4.2. In this case two additional parameters appear in the analysis, the distance d of the connection of the dissipation device from the pivoting point and the length, l of the dissipation device.

Figure 4.24 plots rocking response diagrams for free-standing columns with slenderness $\tan \alpha = 1/6$ with finite-length supplemental hysteretic dampers (say buckling-restrained braces) with $l/h = 0.2$, $b/d = 0.1$ and normalized yield-strength $\frac{k_d u_y}{mg} = 5\%$ and 10% ; while Figure 4.23 plots rocking response diagrams for free-standing columns with slenderness $\tan \alpha = 1/6$ with finite length supplemental viscous ($q = 1$) dampers with $l/h = 0.2$, $b/d = 0.1$ and normalized damping constant $\frac{C}{mp} = 5$ and 10 .

In Figures 4.24 and 4.25 similar trends as those discussed for the corresponding Figures 4.23 and 4.23 are observed; while the additional lever arm $d = 0.1b$ appears to have marginal effect on the peak response in particular for taller columns.

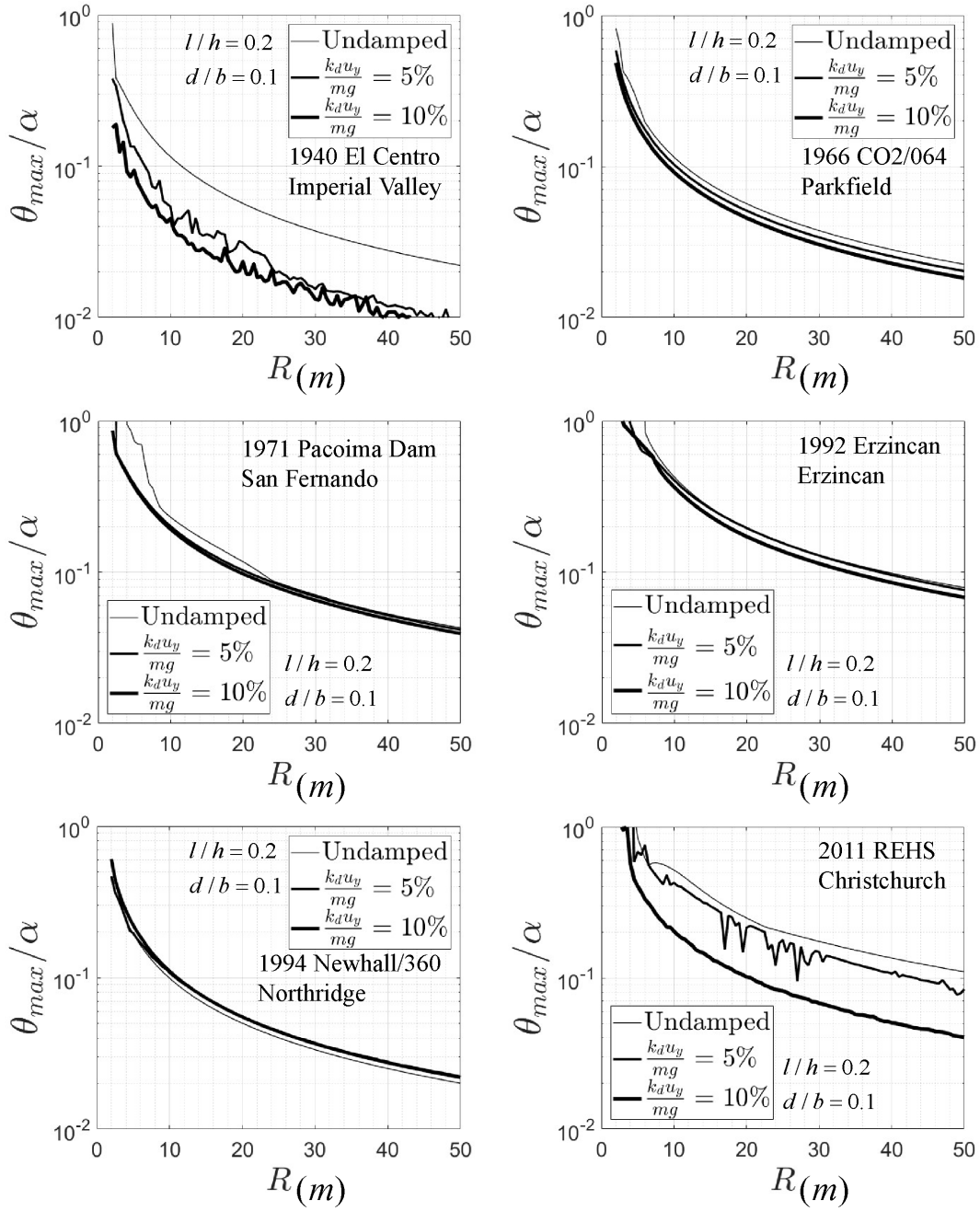


Figure 4.24: Peak rotation as a function of the size of free-standing columns with slenderness $\tan \alpha = 1/6 = 0.167$ with supplemental hysteretic dampers with length ($l = 0.2h$) installed along the sides of the rocking columns at a distance ($d = 0.1b$) when excited by the six strong ground motions presented in this study.

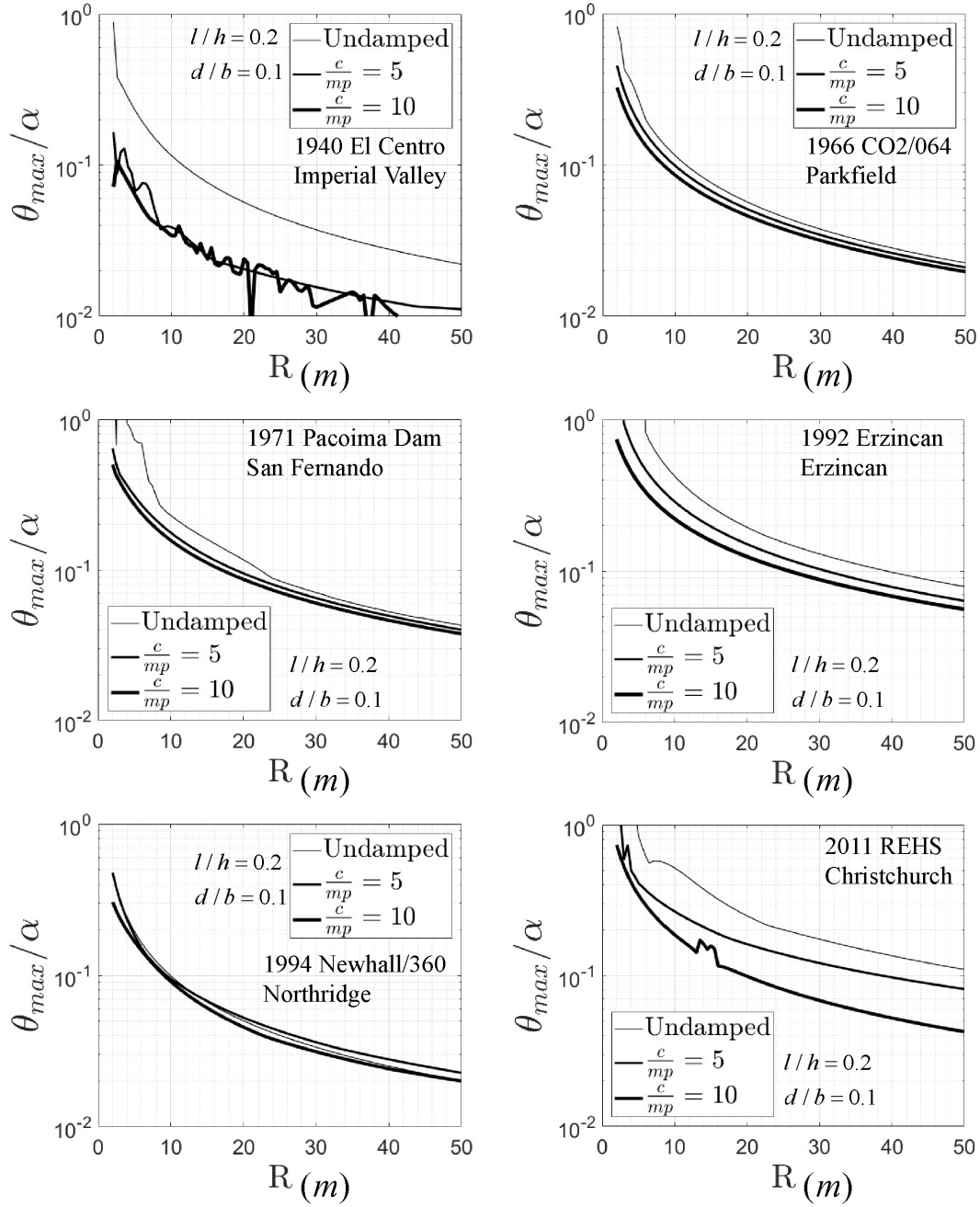


Figure 4.25: Peak rotation as a function of the size of free-standing columns with slenderness $\tan \alpha = 1/6 = 0.167$ with supplemental viscous dampers ($q = 1$) with length ($l = 0.2h$) installed along the sides of the rocking columns at a distance ($d = 0.1b$) when excited by the six strong ground motions presented in this study.

Conclusion

This chapter investigates the nonlinear seismic response of a yielding oscillator coupled with rocking wall equipped with along their side (or at their pivoting point) with vertical energy dissipation devices which offer either hysteretic or viscous (linear or nonlinear) dissipation. The full nonlinear equations of motions are derived and this study offers a comprehensive parametric analysis which reaches the following conclusions:

- When supplemental damping is added to yielding SDOF oscillator coupled with a rocking wall, the damped wall system suppresses the peak inelastic displacements .
- The distance of dampers has marginal effect on the maximum deformation.
- In some cases when SDOF oscillator coupled with a rocking wall with supplemental damping devices, the damped response might exceed the undamped response, which shows that the response of these coupled systems are effected strongly by kinematic characteristics of the ground motions.
- Viscous dampers and hysteretic dampers even with the equivalent force have different behavior, they should be used with caution considering the their force-deformation behavior, since in some cases (specially for large walls) hysteretic dampers might amplify the response.

CHAPTER 5: CONCLUSION

This study first examines different configurations of both stepping rocking walls and pinned rocking walls that have been reported in the literature. Next, effect of additional vertical tendons or vertical damping devices in maximum response of the system is investigated. This research first derives the nonlinear equations of motion of a yielding oscillator coupled with a rocking wall and the dependability of the one-degree of freedom idealization is validated against the nonlinear time-history response analysis of a 9-story moment-resisting frame coupled with a rocking wall and it reaches through a comprehensive parametric analysis the following conclusions

- When the yielding SDOF oscillator is coupled with a stepping rocking wall, the participation of the stepping wall suppresses the peak inelastic displacements in particular for more flexible structures with the heavier wall being most effective
- The participation of the stepping rocking wall reduces drastically the permanent displacements which vanish completely as the weight of the wall increases.
- Pinned rocking wall increases in general the peak inelastic displacements with the heavier wall being most unfavorable.
- The participation of the pinned rocking wall increases the permanent displacements through a wide range of the response spectrum. This unfavorable response is mainly because the moment from the weight of a pinned rocking wall works against the stability of the system. Accordingly, the coupling a yielding frame with a pinned rocking wall may result to unfavorable response and should be used with caution.
- The length of the coupling arm has a marginal effect on the response of the SDOF oscillator when coupled with a rocking wall. Nevertheless, the pinned wall amplifies the response for

most of the range of the spectrum even when short arm lengths are considered.

- The effect of the vertical tendons even when they are stiff ($\frac{EA}{m_w g} = 200$) and highly prestressed ($P_o = m_w g$) is marginal. Given that the vertical tendons increase the vertical reactions at the pivoting corners by more than 50%, the study concludes that for medium- to high-rise buildings, vertical tendons in rocking walls are not recommended.
- The SDOF idealization presented in this study compares satisfactory with finite-element analysis of a 9-story steel SAC building coupled with a stepping rocking wall; therefore, the SDOF idealization can be used with confidence for preliminary analysis and design.
- When supplemental damping is added to yielding SDOF oscillator coupled with a rocking wall, the damped wall system suppresses the peak inelastic displacements.
- The distance of dampers has marginal effect on the maximum deformation.
- In some cases when SDOF oscillator coupled with a rocking wall with supplemental damping devices, the damped response might exceed the undamped response, which shows that the response of these coupled systems are effected strongly by kinematic characteristics of the ground motions.
- Viscous dampers and hysteretic dampers even with the equivalent force have different behavior, when they are used, their force–deformation behavior should be fully considered, since in some cases (specially for large walls) hysteretic dampers might amplify the response.

LIST OF REFERENCES

- [1] Bertero VV, Mahin SA, and Herrera RA (1978), Aseismic design implications of nearfault san fernando earthquake records, *Earthquake Engineering & Structural Dynamics*, **6**(1):31–42.
- [2] Makris N (2005), Near-source earthquakes, base isolated structures and semiactive damper, in: GD Manolis and DE Beskos, eds., *1st International Symposium Earthquake Resisting Engineering Structures*, pages 219–360.
- [3] Alavi B and Krawinkler H (2004), Behavior of momentresisting frame structures subjected to nearfault ground motions, *Earthquake Engineering & Structural Dynamics*, **33**(6):687–706.
- [4] Makris N and Chang SP (2000), Response of damped oscillators to cycloidal pulses, *Journal of engineering mechanics*, **126**(2):123–131.
- [5] Meek J (1978), Dynamic response of tipping core buildings, *Earthquake Engineering & Structural Dynamics*, **6**(5):437–454.
- [6] PCI Ad Hoc Committee on Precast Walls (1997), Design for lateral force resistance with precast concrete shear walls, *PCI journal*, **42**(5).
- [7] Priestley MN (1991), Overview of presss research program, *PCI journal*, **36**(4):50–57.
- [8] Priestley MN (1996), The presss programcurrent status and proposed plans for phase ill, *PCI journal*, **4**(2):22–40.
- [9] Nakaki SD, Stanton JF, and Sritharan S (1999), An overview of the presss five-story precast test building, *PCI journal*, **44**(2):26–39.

- [10] Priestley MN, Sritharan S, Conley JR, and Pampanin S (1999), Preliminary results and conclusions from the presss five-story precast concrete test building, *PCI journal*, **44**(6):42–67.
- [11] Kurama YC, Sause R, Pessiki S, and Lu LW (2002), Seismic response evaluation of unbonded post-tensioned precast walls, *Structural Journal*, **99**(5):641–651.
- [12] Kurama Y, Sause R, Pessiki S, and Lu LW (1999), Lateral load behavior and seismic design of unbonded post-tensioned precast concrete walls, *Structural Journal*, **96**(4):622–632.
- [13] Mander JB and Cheng CT (1997), *Seismic resistance of bridge piers based on damage avoidance design*, Report Report no. NCEER-97-0014.
- [14] Holden T, Restrepo J, and Mander JB (2003), Seismic performance of precast reinforced and prestressed concrete walls, *Journal of Structural Engineering*, **129**(3):286–296.
- [15] Ajrab JJ, Pekcan G, and Mander JB (2004), Rocking wall-frame structures with supplemental tendon systems, *Journal of Structural Engineering*, **130**(6):895–903.
- [16] Lu Y (2005), Inelastic behaviour of rc wallframe with a rocking wall and its analysis incorporating 3d effect, *The Structural Design of Tall and Special Buildings*, **14**(1):15–35.
- [17] Toranzo L, Restrepo J, Mander J, and Carr A (2009), Shake-table tests of confined-masonry rocking walls with supplementary hysteretic damping, *Journal of Earthquake Engineering*, **13**(6):882–898.
- [18] Alavi B and Krawinkler H (2004), Strengthening of momentresisting frame structures against nearfault ground motion effects, *Earthquake Engineering & Structural Dynamics*, **33**(6):707–722.

- [19] Wada A, Qu Z, Motoyui S, and Sakata H (2011), Seismic retrofit of existing src frames using rocking walls and steel dampers, *Frontiers of Architecture and Civil Engineering in China*, **5**(3):259–266.
- [20] Qu Z, Wada A, Motoyui S, Sakata H, and Kishiki S (2012), Pinsupported walls for enhancing the seismic performance of building structures, *Earthquake Engineering & Structural Dynamics*, **41**(14):2075–2091.
- [21] Hu X and Zhang Y (2012), Seismic performance of reinforced concrete frames retrofitted with self-centering hybrid wall, *Advances in Structural Engineering*, **15**(12):2131–2143.
- [22] Nicknam A and Filiatrault A (2014), Numerical evaluation of seismic response of buildings equipped with propped rocking wall systems, in: *10th U.S. National Conference on Earthquake Engineering: Frontiers of Earthquake Engineering*.
- [23] Grigorian CE and Grigorian M (2015), Performance control and efficient design of rocking-wall moment frames, *Journal of Structural Engineering*, **142**(2):04015139.
- [24] Grigorian M and Grigorian C (2016), An introduction to the structural design of rocking wallframes with a view to collapse prevention, selfalignment and repairability, *The Structural Design of Tall and Special Buildings*, **25**(2):93–111.
- [25] Kurama YC, Sritharan S, Fleischman RB, Restrepo JI, Henry RS, Cleland NM, Ghosh S, and Bonelli P (2018), Seismic-resistant precast concrete structures: State of the art, *Journal of Structural Engineering*, **4**(144):03118001.
- [26] Housner GW (1963), The behavior of inverted pendulum structures during earthquakes, *Bulletin of the Seismological Society of America*, **53**(2):403–417.
- [27] Makris N (2014), A half-century of rocking isolation, *Earthquakes and Structures*, **7**(6):1187–1221.

- [28] Makris N (2014), The role of the rotational inertia on the seismic resistance of freestanding rocking columns and articulated frames, *Bulletin of the Seismological Society of America*, **104**(5):2226–2239.
- [29] Makris N and Vassiliou MF (2014), Dynamics of the rocking frame with vertical restrainers, *Journal of Structural Engineering*, **141**(10):04014245.
- [30] Vassiliou MF and Makris N (2015), Dynamics of the vertically restrained rocking column, *Journal of Engineering Mechanics*, **141**(12):04015049.
- [31] Makris N and Vassiliou MF (2014), Are some top-heavy structures more stable?, *Journal of Structural Engineering*, **140**(5):06014001.
- [32] Aslam M, Scalise DT, and Godden WG (1980), Earthquake rocking response of rigid bodies, *Journal of the Structural Division*, **106**(2):377–392.
- [33] Dimitrakopoulos EG and DeJong MJ (2012), Revisiting the rocking block: closed-form solutions and similarity laws, in: *Proc. R. Soc. A*, volume 468, The Royal Society, pages 2294–2318.
- [34] Makris N and Roussos Y (1999), Rocking response of rigid blocks under near-source ground motions, *Geotechnique*, **50**:243–262.
- [35] Yim C, Chopra AK, and Penzien J (1980), Rocking response of rigid blocks to earthquakes, *Earthquake Engineering & Structural Dynamics*, **8**(6):565–587.
- [36] Zhang J and Makris N (2001), Rocking response of free-standing blocks under cycloidal pulses, *Journal of Engineering Mechanics*, **127**(5):473–483.
- [37] Makris N and Konstantinidis D (2003), The rocking spectrum and the limitations of practical design methodologies, *Earthquake engineering & structural dynamics*, **32**(2):265–289.

- [38] Kurama YC (2000), Seismic design of unbonded post-tensioned precast concrete walls with supplemental viscous damping, *ACI Structural Journal*, **97**(4):648–658.
- [39] Cheok GS and Lew H (1993), Model precast concrete beam-to-column connections subject to cyclic loading, *PCI Journal*, **38**(4):80–92.
- [40] Filiatrault A, Restrepo J, and Christopoulos C (2004), Development of self-centering earthquake resisting systems, in: *13th World Conference on Earthquake Engineering*.
- [41] Restrepo JI and Rahman A (2007), Seismic performance of self-centering structural walls incorporating energy dissipators, *Journal of Structural Engineering*, **133**(11):1560–1570.
- [42] Erkmen B and Schultz AE (2009), Self-centering behavior of unbonded, post-tensioned precast concrete shear walls, *Journal of Earthquake Engineering*, **13**(7):1047–1064.
- [43] Belleri A, Schoettler MJ, Restrepo JI, and Fleischman RB (2014), Dynamic behavior of rocking and hybrid cantilever walls in a precast concrete building, *ACI Structural Journal*, **111**(3):661.
- [44] Nazari M, Sritharan S, and Aaleti S (2017), Single precast concrete rocking walls as earthquake force-resisting elements, *Earthquake Engineering & Structural Dynamics*, **46**(5):753–769.
- [45] Sun T, Kurama YC, and Ou J (2018), Practical displacement-based seismic design approach for pwf structures with supplemental yielding dissipators, *Engineering Structures*, **172**:538–553.
- [46] Makris N and Aghagholizadeh M (2017), The dynamics of an elastic structure coupled with a rocking wall, *Earthquake Engineering & Structural Dynamics*, **46**(6):945–962.
- [47] Aghagholizadeh M and Makris N (2017), Seismic response of a yielding structure coupled with a rocking wall, *Journal of Structural Engineering*, **144**(2):04017196.

- [48] Gioiella L, Tubaldi E, Gara F, Dezi L, and Dall'Asta A (2018), Modal properties and seismic behaviour of buildings equipped with external dissipative pinned rocking braced frames, *Engineering Structures*, **172**:807–819.
- [49] Aghagholizadeh M and Makris N (2018), Earthquake response analysis of yielding structures coupled with vertically restrained rocking walls, *Earthquake engineering & structural dynamics*, (<https://doi.org/10.1002/eqe.3116>):1–20.
- [50] Hall JF, Heaton TH, Halling MW, and Wald DJ (1995), Near-source ground motion and its effects on flexible buildings, *Earthquake Spectra*, **11**(4):569–605.
- [51] Makris N and Aghagholizadeh M (2017), Earthquake protection of a yielding frame with a rocking wall, in: *International Workshop On Performance-Based Seismic Design Of Structures (Resilience, Robustness)*, page 1:10.
- [52] Wen YK (1976), Method for random vibration of hysteretic systems, *Journal of the engineering mechanics division*, **102**(2):249–263.
- [53] Makris N and Roussos Y (2000), Rocking response of rigid blocks under near-source ground motions, *Geotechnique*, **50**:243–262.
- [54] Makris N and Black CJ (2002), Uplifting and overturning of equipment anchored to a base foundation, *Earthquake spectra*, **18**(4):631–661.
- [55] Makris N and Roussos Y (1998), *Rocking response and overturning of equipment under horizontal pulse-type motions*, Report Report PEER 1998/05.
- [56] MATLAB (2016), *High performance numerical computation and visualization software*, The Math works, Natick, Mass.
- [57] Bouc R (1967), Forced vibration of mechanical systems with hysteresis, in: *Fourth conference on non-linear oscillation*.

- [58] Wen YK (1975), Approximate method for nonlinear random vibration, *Journal of Engineering Mechanics*, **101**.
- [59] Baber T and Wen YK (1981), Random vibration of hysteretic degrading systems, *Journal of the Engineering Mechanics Division*, ASCE, **107**(EM6):1069–1087.
- [60] Constantinou MC and Adnane MA (1987), *Dynamics of soil-base-isolated structure systems. Report 4: Evaluation of two models for yielding systems*, Report, Drexel University.
- [61] Makris N and Kampas G (2013), The engineering merit of the effective period of bilinear isolation systems, *Earthquakes and Structures*, **4**(4):397–428.
- [62] Goda K, Hong H, and Lee C (2009), Probabilistic characteristics of seismic ductility demand of sdof systems with bouc-wen hysteretic behavior, *Journal of Earthquake Engineering*, **13**(5):600–622.
- [63] Kunnath SK, Mander JB, and Fang L (1997), Parameter identification for degrading and pinched hysteretic structural concrete systems, *Engineering Structures*, **19**(3):224–232.
- [64] McKenna F, Fenves GL, and Scott MH (2000), Open system for earthquake engineering simulation, *University of California, Berkeley, CA*.
- [65] Vassiliou MF, Mackie KR, and Stojadinovi B (2014), Dynamic response analysis of solitary flexible rocking bodies: modeling and behavior under pulselike ground excitation, *Earthquake Engineering & Structural Dynamics*, **43**(10):1463–1481.
- [66] Vassiliou MF, Mackie KR, and Stojadinovi B (2017), A finite element model for seismic response analysis of deformable rocking frames, *Earthquake Engineering & Structural Dynamics*, **46**(3):447–466.
- [67] Aghagholizadeh M (2018), Study on dynamics of an elastic oscillator coupled with a rocking wall, *arXiv preprint arXiv:1803.02669*.

- [68] Veletsos A, Newmark N, and Chelapati C (1965), Deformation spectra for elastic and elastoplastic systems subjected to ground shock and earthquake motions, in: *Proceedings of the 3rd world conference on earthquake engineering*, volume 2, pages 663–682.
- [69] Makris N and Chang SP (2000), Effect of viscous, viscoplastic and friction damping on the response of seismic isolated structures, *Earthquake Engineering & Structural Dynamics*, **29**(1):85–107.
- [70] Alavi B and Krawinkler H (2001), *Effects of near-fault ground motions on frame structures*, John A. Blume Earthquake Engineering Center.
- [71] Vassiliou MF and Makris N (2011), Estimating time scales and length scales in pulselike earthquake acceleration records with wavelet analysis, *Bulletin of the Seismological Society of America*, **101**(2):596–618.
- [72] Barenblatt GI (1996), *Scaling, self-similarity, and intermediate asymptotics: dimensional analysis and intermediate asymptotics*, volume 14, Cambridge: Cambridge University Press.
- [73] Ricker N (1944), Wavelet functions and their polynomials, *Geophysics*, **9**(3):314–323.
- [74] Garini E, Makris N, and Gazetas G (2014), Elastic and inelastic systems under near-fault seismic shaking: acceleration records versus optimally-fitted wavelets, *Bulletin of Earthquake Engineering*, **13**(2):459–482.
- [75] Ricker N (1943), Further developments in the wavelet theory of seismogram structure, *Bulletin of the Seismological Society of America*, **33**(3):197–228.
- [76] Makris N and Kampas G (2016), Size versus slenderness: Two competing parameters in the seismic stability of freestanding rocking columns, *Bulletin of the Seismological Society of America*, **106**(1):104–122.

- [77] Lanczos C (1979), *The variational principles of mechanics*, New York: Dover Publications.
- [78] Mazzoni S, McKenna F, Scott MH, and Fenves GL (2006), OpenSees command language manual, *Pacific Earthquake Engineering Research (PEER) Center*.
- [79] SAC Joint Venture and Guidelines Development Committee (2000), *Recommended seismic design criteria for new steel moment-frame buildings*, Federal Emergency Management Agency.
- [80] Gupta A and Krawinkler H (1999), *Seismic demands for the performance evaluation of steel moment resisting frame structures*, Report, Stanford University Stanford.
- [81] Chopra AK and Goel RK (2002), A modal pushover analysis procedure for estimating seismic demands for buildings, *Earthquake Engineering & Structural Dynamics*, **31**(3):561–582.
- [82] Aghagholizadeh M and Makris N (2018), Seismic response of yielding frames coupled with restrained rocking walls, in: *16th European Conference on Earthquake Engineering*.
- [83] Aghagholizadeh M and Massumi A (2012), Relation between dynamic characteristics and damage index of rc-mrfs using non-linear incremental dynamic analyses, in: *15th World Conference on Earthquake Engineering*.
- [84] Hilber HM, Hughes TJ, and Taylor RL (1977), Improved numerical dissipation for time integration algorithms in structural dynamics, *Earthquake Engineering & Structural Dynamics*, **5**(3):283–292.
- [85] Ohtori Y, Christenson R, Spencer Jr B, and Dyke S (2004), Benchmark control problems for seismically excited nonlinear buildings, *Journal of Engineering Mechanics*, **130**(4):366–385.

- [86] Gupta A and Krawinkler H (2000), Behavior of ductile SMRFs at various seismic hazard levels, *Journal of Structural Engineering*, **126**(1):98–107.
- [87] Paulay T (1969), The coupling of reinforced concrete shear walls, in: *The Fourth World Conference on Earthquake Engineering*.
- [88] Fintel M (1975), Ductile shear walls in earthquake-resistant multistory buildings, in: *Wind and Seismic Effects: Proceedings of the Seventh Joint Panel Conference of the US-Japan Cooperative Program in Natural Resources*, volume 470, US Department of Commerce, National Bureau of Standards, page 33.
- [89] Kelly JM, Skinner R, and Heine A (1972), Mechanisms of energy absorption in special devices for use in earthquake resistant structures, *Bulletin of New Zealand Society of Earthquake Engineering*, **5**(3):63–88.
- [90] Beck JL and Skinner R (1972), *The seismic response of a proposed reinforced concrete railway viaduct*, Report 369, Physics and Engineering Laboratory DSIR, Report No 369.
- [91] Beck JL and Skinner R (1974), The seismic response of a reinforced concrete bridge pier designed to step, *Earthquake Eng. Struct. Dyn.*, **2**(4):343–358.
- [92] Constantinou MC, Soong TT, and Dargush GF (1998), *Passive energy dissipation systems for structural design and retrofit*, Report, Multidisciplinary Center for Earthquake Engineering Research.
- [93] Soong T and Dargush G (1999), *Passive energy dissipation and active control*, Boca Raton: Structural Engineering Handbook. CRC Press LLC.
- [94] Symans M, Charney F, Whittaker A, Constantinou M, Kircher C, Johnson M, and McNamara R (2008), Energy dissipation systems for seismic applications: current practice and recent developments, *Journal of Structural Engineering*, **134**(1):3–21.

- [95] Wada A, Saeki E, Takeuchi T, and Watanabe A (1989), *Development of unbonded brace*, Report 115, Nippon Steel.
- [96] Chang S and Makris N (2000), Effect of various energy dissipation mechanisms in suppressing structural response, in: *12th World Conf on Earthq. Eng.*, Auckland, New Zealand.
- [97] Black CJ, Aiken ID, and Makris N (2002), *Component testing, stability analysis, and characterization of buckling-restrained unbonded braces (TM)*, Report PEER 2002/08, Pacific Earthquake Engineering Research Center.
- [98] Black CJ, Makris N, and Aiken ID (2004), Component testing, seismic evaluation and characterization of buckling-restrained braces, *Journal of Structural Engineering*, **130**(6):880–894.
- [99] Skinner R, Kelly J, and Heine A (1974), Hysteretic dampers for earthquakeresistant structures, *Earthquake Engineering & Structural Dynamics*, **3**(3):287–296.
- [100] Skinner R, Tyler R, Heine A, and Robinson W (1980), Hysteretic dampers for the protection of structures from earthquakes, *Bulletin of New Zealand National Society of Earthquake Engineering*, **13**(1):22–36.
- [101] Blakeley WH, Charlesn AW, Hitchcock HC, M ML, Priestley MN, Sharpe RD, and Skinner R (1979), Recommendations for the design and construction of base isolated structures, *Bulletin of The New Zealand National Society for Earthquake Engineering*, **12**(2):136–157.
- [102] Kirkpatrick P (1927), Seismic measurements by the overthrow of columns, *Bulletin of the seismological society of America*, **17**(2):95–109.
- [103] Ikegami R and Kishinouye F (1947), 10. a study on the overturning of rectangular columns in the case of the nankai earthquake on december 21, 1946, *Bulletin of Earthquake Research Institute*, **25**(1):49–55.

- [104] Ikegami R and Kishinouye F (1950), The acceleration of earthquake motion deduced from overturning of the gravestones in case of the imaichi earthquake on dec. 26, 1949, *Bulletin of Earthquake Research Institute Tokyo Univ.*, **28**:121–128.
- [105] Muto K, Umemura H, and Sonobe Y (1960), Study of the overturning vibrations of slender structures, in: *Proc., 2nd World Conf. on Earthq. Eng.*, volume 2, Association for Science Documents Information Tokyo, pages 1239–1261.
- [106] Ishiyama Y (1982), Motions of rigid bodies and criteria for overturning by earthquake excitations, *Earthquake Engineering & Structural Dynamics*, **10**(5):635–650.
- [107] Spanos PD and Koh AS (1984), Rocking of rigid blocks due to harmonic shaking, *Journal of Engineering Mechanics*, **110**(11):1627–1642.
- [108] Hogan S (1989), On the dynamics of rigid-block motion under harmonic forcing, *Proceedings of Royal Society of London A*, **425**(1869):441–476.
- [109] Hogan S (1990), The many steady state responses of a rigid block under harmonic forcing, *Earthquake Engineering & Structural Dynamics*, **19**(7):1057–1071.
- [110] Tso W and Wong C (1989), Steady state rocking response of rigid blocks part 1: Analysis, *Earthquake Engineering & Structural Dynamics*, **18**(1):89–106.
- [111] Wong C and Tso W (1989), Steady state rocking response of rigid blocks part 2: Experiment, *Earthquake Engineering & Structural Dynamics*, **18**(1):107–120.
- [112] Makris N and Zhang J (2001), Rocking response of anchored blocks under pulse-type motions, *Journal of Engineering Mechanics*, **127**(5):484–493.
- [113] Dimitrakopoulos EG and DeJong MJ (2012), Overturning of retrofitted rocking structures under pulse-type excitations, *J. Eng. Mech.*, **138**(8):963–972.

- [114] Kimura K, Yoshioka K, Takeda T, Fukuya Z, and Takemoto K (1976), Tests on braces encased by mortar in-filled steel tubes, in: *Summaries of technical papers of annual meeting, Architectural Institute of Japan*, volume 1041, pages 1–42.
- [115] Black CJ, Makris N, and Aiken I (2003), Component testing and modeling of buckling restrained unbonded braces, in: *Proc., Conf. on Behaviour of Steel Structures in Seismic Areas–Stessa*, pages 141–145.
- [116] Makris N (2018), Seismic isolation: Early history, *Earthquake Engineering & Structural Dynamics*, (<https://doi.org/10.1002/eqe.3116>).
- [117] Makris N and Aghagholizadeh M (2018), The effect of supplemental hysteretic and viscous damping on the rocking response of free-standing columns, *Journal of Engineering Mechanics*.
- [118] Bolt BA (1971), The san fernando valley, california, earthquake of february 9 1971: Data on seismic hazards, *Bulletin of the Seismological Society of America*, **61**(2):501–510.
- [119] Bolt BA (1975), *The San Fernando earthquake, 1971. Magnitudes, aftershocks, and fault dynamics*, Chapter 21, *Bulletin 196*, California Division of Mines and Geology.
- [120] Bertero VV, Herrera R, and Mahin S (1976), Establishment of design earthquakes-evaluation of present methods, in: *International Symposium on Earthquake Structural Engineering*, St. Louis, Missouri.
- [121] Skinner R, Robinson W, and McVerry G (1993), *An introduction to seismic isolation*, New York: John Wiley & Sons.
- [122] Kelly JM (1993), *Earthquake-resistant design with rubber*, London: Springer.
- [123] Bradley BA and Cubrinovski M (2011), Near-source strong ground motions observed in the 22 february 2011 christchurch earthquake, *Seismological Research Letters*, **82**(6):853–865.

- [124] Makris N (1997), Rigidity–plasticity–viscosity: Can electrorheological dampers protect baseisolated structures from nearsource ground motions?, *Earthq. Eng. Struct. Dyn.*, **26**(5):571–591.
- [125] Mavroeidis GP and Papageorgiou AS (2003), A mathematical representation of near-fault ground motions, *Bull. Seismol. Soc. Am.*, **93**(3):1099–1131.
- [126] Vassiliou MF and Makris N (2011), Estimating time scales and length scales in pulselike earthquake acceleration records with wavelet analysis, *Bull. Seismol. Soc. Am.*, **101**(2):596–618.